



E17
Lehrstuhl für
Biomedizinische Physik

Physik Department

Diploma Thesis

Experimental characterization of the first preclinical X-ray phase contrast CT scanner

Mark Müller
Technische Universität München
Physik Department
Chair of Biomedical Physics E17
Supervisor: Prof. Dr. Franz Pfeiffer

September 13, 2013



Technische Universität München

Abstract

In the field of biomedical X-ray imaging, novel techniques, such as grating-based phase contrast and dark-field imaging, have the potential to improve medical diagnosis by enhanced soft-tissue contrast.

In this work, a characterization of the first preclinical X-ray phase contrast CT scanner is presented. Two fundamental characteristics of the scanner have been investigated.

A series of projection images and CT data sets in phase and attenuation contrast were acquired with different acquisition settings of the scanner. Subsequently, the contrast-to-noise ratios of the images were determined and the results for different acquisition settings were compared. The implications for practical imaging purposes were discussed and a recommendation for the acquisition settings of future imaging applications is given.

In the second part, the spatial system response of the scanner was characterized. Data from direct and indirect measurements of the modulation transfer function of the setup were acquired and analyzed. The maximal resolution of the scanner was estimated by different resolution measures. Finally, a brief example is given to demonstrate how the results of this study can be used to improve the sharpness of the resulting images.

Kurzfassung

Die Gitterbasierten Phasenkontrast- und Dunkelfeldbildgebungsverfahren mit Röntgenstrahlung stellen neuartige Modalitäten in der biomedizinischen Bildgebung dar. Aufgrund des verbesserten Weichteilkontrasts bergen diese Methoden großes Potenzial, die medizinische Röntgendiagnostik zu verbessern.

Die vorliegende Arbeit befasst sich mit der Charakterisierung des weltweit ersten Kleintier-Röntgen-Phasenkontrast CT Scanners für präklinische Forschungszwecke. Im Wesentlichen wurden zwei grundlegende Eigenschaften des Scanners untersucht.

Im ersten Teil wird die Bildqualität von Radiografie- und Tomografiedaten des Scanners mit variierenden Aufnahmeeinstellungen analysiert. Zu diesem Zweck wird das Kontrast-zu-Rausch-Verhältnis der Phasen- und Absorptionskontrastaufnahmen bestimmt und unter verschiedenen Gesichtspunkten verglichen. Anschließend werden die Konsequenzen der präsentierten Ergebnisse für praktische Anwendungen diskutiert und Vorschläge zur Optimierung der Scannereinstellungen gegeben.

Im zweiten Teil wird das Auflösungsvermögen des CT Scanners anhand von verschiedenen Messungen der Modulationstransferfunktion untersucht. In der Folge wird das maximale Auflösungsvermögen mittels unterschiedlicher Auflösungskriterien charakterisiert. Abschließend wird an einem kurzen Anwendungsbeispiel demonstriert, wie mit Hilfe der gewonnenen Daten die Bildqualität der Scanneraufnahmen verbessert werden kann.

Contents

1	Introduction	1
2	Theory	3
2.1	X-ray interaction with matter	3
2.1.1	Complex index of refraction	3
2.1.2	Attenuation	4
2.1.3	Refraction	5
2.2	Grating-based phase contrast X-ray imaging	5
2.2.1	Grating interferometer	5
2.2.2	Talbot effect	6
2.2.3	Phase stepping routine	7
2.3	X-ray Computed Tomography	8
2.3.1	Radon Transform	9
2.3.2	Fourier Slice Theorem	10
2.3.3	Filtered Backprojection	11
2.4	Signal, contrast, and noise	12
2.5	Spatial system response	13
2.5.1	Response function in real space and frequency space	13
2.5.2	Line spread function	14
2.5.3	Edge spread function	14
2.5.4	Resolution measures	15
3	Experimental setup	17
4	Analysis of contrast-to-noise ratio	23
4.1	Data acquisition	23
4.1.1	Acquisition of projection images	23
4.1.2	Acquisition of CT data	23
4.2	Data analysis	25
4.2.1	Analysis of projection images	25
4.2.2	Analysis of CT data	36
4.3	Results and discussion	38
4.3.1	CNR versus gain	38
4.3.2	CNR versus exposure	40
4.3.3	CNR versus peak voltage	52
4.3.4	CNR versus binning	62

4.3.5	CNR versus delay parameters	63
4.4	Summary	68
5	Characterization of the spatial system response	69
5.1	Direct modulation transfer function measurements	69
5.1.1	Data acquisition	69
5.1.2	Data processing	75
5.2	Edge profile measurements	77
5.2.1	Data acquisition	77
5.2.2	Data processing	84
5.3	Results and discussion	86
5.3.1	Direct modulation transfer function measurements	86
5.3.2	Source characterization	90
5.3.3	Edge profile measurements	91
5.3.4	Comparison of direct and indirect modulation transfer function measurements	96
5.3.5	Comparison of binned data from the edge profile measurements	98
5.3.6	Comparison of horizontal and vertical edge profile measurements	101
5.4	Summary	103
5.5	Application: Deconvolution with Richardson-Lucy algorithm	105
6	Summary, conclusions, and outlook	109
Supplementary data		114
A	CNR analysis	115
A.1	Projection data	115
A.1.1	MATLAB processing script	115
A.1.2	CNR versus gain: Acquisition parameters	116
A.1.3	CNR versus exposure time per step: Acquisition parameters	117
A.1.4	Exposure time per phase step versus number of phase steps: Acquisition parameters	118
A.1.5	Maximal CNR versus peak voltage: Acquisition parameters	119
A.1.6	CNR versus peak voltage with the new G ₂ grating: Acquisition parameters and supplementary results	120
A.1.7	CNR versus binning: Acquisition parameters	123
A.1.8	CNR versus delay parameters: Acquisition parameters	124
A.2	CT data	125
A.2.1	Processing and reconstruction	125
A.2.2	List of acquisition parameters for all CT data sets	126
A.2.3	Supplementary results: Low dose and alternative fixation	127
A.3	Literature data of the phantom materials	128
Acknowledgments		129

Bibliography	131
List of Abbreviations	137
List of Figures	140
List of Tables	142

1 Introduction

Ever since the discovery of X-rays by Wilhelm Conrad Röntgen in 1895 [43], for which he was awarded the first Nobel Prize in Physics in 1901, their ability to penetrate matter that is opaque for visible light has been subject to intensive scientific research. X-ray imaging has become an invaluable tool to non-destructively determine the inner structure of various specimens. Nowadays, the most important applications are medical diagnostics, non-destructive industrial testing, security inspections, and scientific research.

The principal of phase contrast imaging was discovered by Frits Zernike in 1942 [62] during his work with diffraction gratings and visible light. Since then, phase contrast imaging has played an important role in the field of optical microscopy. Nevertheless, image formation in X-ray imaging was practically restricted to the differences in transmitted intensity of the irradiated material until the end of the last century. In the last two decades, several phase contrast X-ray imaging techniques have been developed, such as crystal interferometry [6, 31], analyzer-based imaging [13, 23], propagation-based imaging [11, 47], and grating-based imaging [12, 53]. In comparison to conventional attenuation-based imaging, phase contrast X-ray imaging can provide complementary structural information about a specimen. For instance, it can yield enhanced soft tissue contrast for biological samples and therefore is a promising tool for medical diagnosis. The greatest potential for applications in daily clinical practice has the grating-based phase contrast technique, since it has the lowest requirements on the quality of the used X-ray beam and thus can be realized with standard X-ray tube sources [34]. First ex-vivo studies of biological tissue have demonstrated that grating-based phase contrast imaging with a conventional X-ray tube can provide valuable information about a specimen that is inaccessible in standard attenuation-based X-ray imaging [3, 17].

As a first step towards clinical imaging, a preclinical X-ray phase contrast CT scanner for small animals has been developed [51, 52]. The scanner features a rotating gantry system that allows for tomography scans with a stationary sample, and consequently enables the acquisition of phase contrast CT data from a living animal. The gantry setup is based on a grating interferometer with three gratings [34]. The image acquisition is realized by a phase stepping routine [53] that allows the extraction of three different contrast modalities: The conventional attenuation contrast, the phase contrast, and an additional dark-field signal that is based on the scattering properties of the sample [32].

The primary goal of this work was to characterize this preclinical phase contrast CT scanner experimentally in order to find the optimal acquisition settings for future imaging purposes. Since the scanner is basically used for in-vivo imaging of small animals, such as mice and rats, the crucial factors for the image acquisition are the acquisition time, the applied dose, and the image quality in the respective contrast modality. The quality of an image is basically characterized by two properties. On the one hand, the relative visibility of the indi-

vidual features of a sample in the acquired image can be described by the contrast-to-noise ratios of the respective materials. On the other hand, the spatial resolution of an image, which is defined by the minimal distance between two structures of the sample that can still be visibly resolved, can be assessed by characterizing the spatial system response of the scanner. Consequently, the experimental work of this thesis is divided into two parts.

In a first study, radiographic and tomographic data of a phantom were acquired with varying acquisition settings of the scanner and contrast-to-noise ratios for the resulting phase contrast and attenuation contrast images were analyzed in relation to the applied acquisition setting. To assess the contrast-to-noise ratio of radiographic images in phase contrast, a novel analysis method based on the geometry of the phantom was developed and applied.

In a second study, the spatial system response of the phase contrast CT scanner was investigated. A series of experiments were performed to measure the modulation transfer function of the scanner in different planes parallel to the detector. The relative contributions from individual components of the setup to the total spatial system response were quantified, and the maximal resolution of the scanner was estimated by various resolution measures. Finally, a brief example is given to demonstrate how the results of this study can be used to improve image quality of the resulting images. For this purpose, recorded raw images from the scanner were filtered with a deconvolution algorithm and the resulting images in phase, attenuation and dark-field contrast were compared to the images obtained from unfiltered raw images¹.

Outline

A brief overview of the principles of X-ray imaging, as well as an introduction to grating-based phase contrast X-ray imaging and Computed Tomography, are given in Chapter 2. Furthermore, the basic concepts of contrast-to-noise evaluation and linear system theory are introduced, with focus on the application to the performed measurements. A description of the basic features of the X-ray phase contrast CT scanner, complemented with comments on the technical details of the experimental setup used during the measurements, can be found in Chapter 3. The contrast-to-noise ratio analysis of attenuation and phase contrast data from the scanner is presented in Chapter 4, and the characterization of the spatial system response is given in Chapter 5. A summary of the main results and a conclusion of this thesis, as well as a brief outlook, can be found in Chapter 6.

¹ Please note that a few text passages in Chapter 1 and Chapter 2 have already been published under the *GNU Free Documentation License*.

2 Theory

Since the focus of this thesis lies on the experimental characterization of the scanner, the presented theoretical introduction to the underlying physical principals of this work is rather short and restricted to the most essential basics. For the interested reader, recommendations for further reading about the respective topic are presented at the beginning of each section.

2.1 X-ray interaction with matter

The part of the electromagnetic spectrum between extreme ultraviolet radiation and gamma rays is known as X-radiation. The corresponding energies of the X-ray photons range from approximately 100 eV to a few hundred keV. X-rays, nowadays, can be generated in several ways. One possibility is to produce so-called synchrotron radiation in a storage ring, where electrons are kept circulating at constant energies by strong magnetic fields and thereby emit X-rays. This kind of radiation is usually used for scientific research. For clinical applications, the X-rays are typically generated by a conventional X-ray tube. In such a device, electrons are emitted from a cathode and are accelerated to an anode. When hitting the anode, the electrons are decelerated and produce X-rays with a broad spectrum, which is called *Bremsstrahlung*. A detailed description of X-ray sources and the interaction of X-rays with matter can be found in [1, 56].

2.1.1 Complex index of refraction

Since X-rays are electromagnetic waves, their behavior when passing through matter can be described in analogy to visible light by a complex index of refraction [1]:

$$n = 1 - \delta + i\beta. \quad (2.1)$$

The decrement of the real part of the refractive index δ and the imaginary part β generally depend on the energy of the X-rays and on the material properties of the medium. The impact of the index of refraction on the behavior of an electromagnetic wave can be demonstrated by comparing a wave propagating in an arbitrary medium with a constant refractive index n to a wave propagating in vacuum. For reasons of simplicity, a monochromatic plane wave with no polarization, propagating in direction normal to the surface of the medium is assumed here, as depicted in Figure 2.1. The scalar wave function in vacuum ($n=1$) is given by

$$\Psi(z) = E_0 e^{ikz}. \quad (2.2)$$

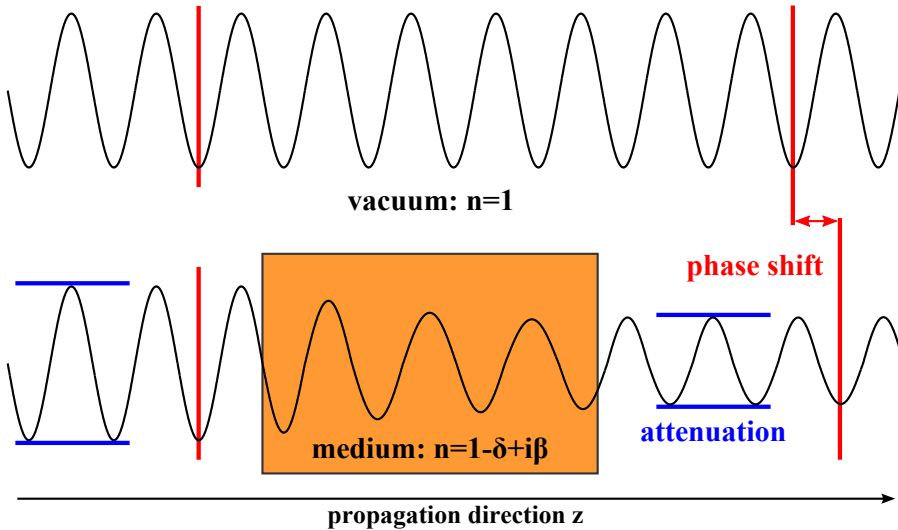


Figure 2.1: Schematic drawing of attenuation and phase shift of an electromagnetic wave propagating in a medium with complex index of refraction n . Attenuation is indicated by the blue lines, whereas the phase shift is indicated by the red lines.

Within the medium, the wave function changes to:

$$\Psi(z) = E_0 e^{i n k z} = E_0 e^{i(1-\delta)kz} e^{-\beta kz}, \quad (2.3)$$

where δkz describes the phase shift and $e^{-\beta kz}$ the exponential decay of the amplitude E_0 and thereby the loss of intensity of the wave. The corresponding macroscopic phenomena to these changes of the wave function are discussed individually in the following.

2.1.2 Attenuation

Attenuation is a macroscopically observable process that is characterized by an intensity reduction of the X-ray beam when passing through matter. For the typical X-ray energies used for biomedical imaging, which lie between 20 keV and 100 keV, attenuation is caused by photoelectric absorption and incoherent, inelastic scattering, known as Compton scattering [1]. The relation between the loss of intensity and the imaginary part of the refraction index of an object with thickness d is given by the *Lambert-Beer Law*:

$$I = I_0 e^{-2\beta kd} = I_0 e^{-\mu d}, \quad (2.4)$$

where $\mu = 2k\beta$ is the linear attenuation coefficient and I_0 the intensity of the wave before passing the object [56]. The linear attenuation coefficient depends on the used X-ray energies and the elemental composition of the respective material. Image formation in attenuation-based X-ray imaging relies on measuring the differences in intensity of the X-ray beam after traversing a sample and therefore visualizes the differences of the attenuation coefficients of

the materials in a sample. For instance, the strong contrast between bone and soft tissue in conventional radiography is due to the considerably higher attenuation coefficient of bone compared to soft tissue for the typically applied X-ray energies.

2.1.3 Refraction

From Equation 2.3, it can be deduced that the total phase shift Φ of a monochromatic electromagnetic wave passing through a medium with refraction index n and thickness d is given by

$$\Phi = \delta k d. \quad (2.5)$$

Considering an object with increasing refractive index or thickness along the axis perpendicular to the incident wave, the total phase shift increases correspondingly along this axis, which here is referred to as x-axis. This leads to a change in propagation direction of the X-ray beam, which is generally known as refraction. The refraction angle α is directly proportional to the local gradient of the object's phase shift along the x-axis and can be quantified by

$$\alpha = \frac{1}{k} \frac{\partial \Phi(x)}{\partial x}. \quad (2.6)$$

In contrast to visible light, for which the real part of the refractive index n can deviate strongly from unity, the refractive index decrement δ for X-rays is typically in the order of 10^{-5} . Thus, the refraction angles for X-rays are generally very small and are usually detected indirectly by interferometric methods. Image formation in phase contrast imaging is based on the measurement of the differences in refraction angles of the beam introduced by the object, as explained further for the case of a grating interferometer in the following section.

The refraction of X-rays can be described on the elementary particle level by elastic, coherent scattering of the X-rays at the electrons in the respective material, known as Thomson scattering [1].

2.2 Grating-based phase contrast X-ray imaging

The grating-based phase contrast X-ray imaging technique basically relies on the accurate measurement of the refraction angles introduced to the X-ray beam, when passing through a sample, by translating the angular deviations into changes of locally transmitted intensity [34]. A detailed introduction to the theory and experimental realization of this technique can be found in [2, 34, 53].

2.2.1 Grating interferometer

Since the first X-ray grating interferometer was built [12], various slightly different setups for this method have been developed. In this work, a so-called Talbot-Lau interferometer is used [34].

The typical components of this interferometer type are:

- A spatially incoherent X-ray source, such as a conventional laboratory X-ray source,
- a source grating G_0 ,
- a phase grating G_1 ,
- an analyzer grating G_2 ,
- a conventional X-ray detector.

The alignment of the individual components is sketched in Figure 2.2. The exact parameters of the used setup can be found in Chapter 3.

2.2.2 Talbot effect

The grating interferometer is based on the Talbot effect, which is a Fresnel diffraction effect that leads to repetition of a periodic wave front after a certain propagation distance called the Talbot length. The periodic wave front can be generated by spatially coherent illumination of a periodic structure, like a diffraction grating, and if so, the intensity distribution of the wave field at the Talbot length resembles exactly the structure of the grating and is called a self-image [11, 49]. Furthermore, periodic intensity variations are created at certain fractional Talbot lengths [27, 48]. Since the fractional Talbot lengths and the periods of the intensity fringes can be calculated by knowing the parameters of the illuminating radiation and the illuminated grating, the exact position of the respective intensity distribution can be determined. An angular change to the incoming X-ray beam leads to a transverse shift of the intensity pattern, as depicted in Figure 2.2. Consequently, the basic idea of phase contrast imaging with a Talbot interferometer is to determine the refraction angles of the X-ray beam by measuring the transverse displacement of the intensity distribution at a certain Talbot distance.

Since a standard laboratory X-ray source does not meet the requirement for spatially coherent illumination at the position of the phase grating G_1 , an absorption mask, known as the source grating G_0 , is introduced to create an array of individually coherent but mutually incoherent sources that fulfill the requirement for spatial coherence and allow for the creation of a Talbot interference pattern [34].

Since the Talbot fringes for typically used X-ray energies and periods of the phase grating have periods of a few μm , they cannot be resolved by a conventional X-ray detector. Therefore, a third grating, known as the analyzer grating G_2 , is positioned immediately in front of the X-ray detector. The analyzer grating is an absorption mask with the same period as the expected period of the Talbot fringes at the respective position of the G_2 grating. The superposition of the interference pattern and the grating profile allow for the accurate determination of the transverse shift of the Talbot pattern using a conventional X-ray detector with a much larger pixel size than the period of the Talbot fringes [2].

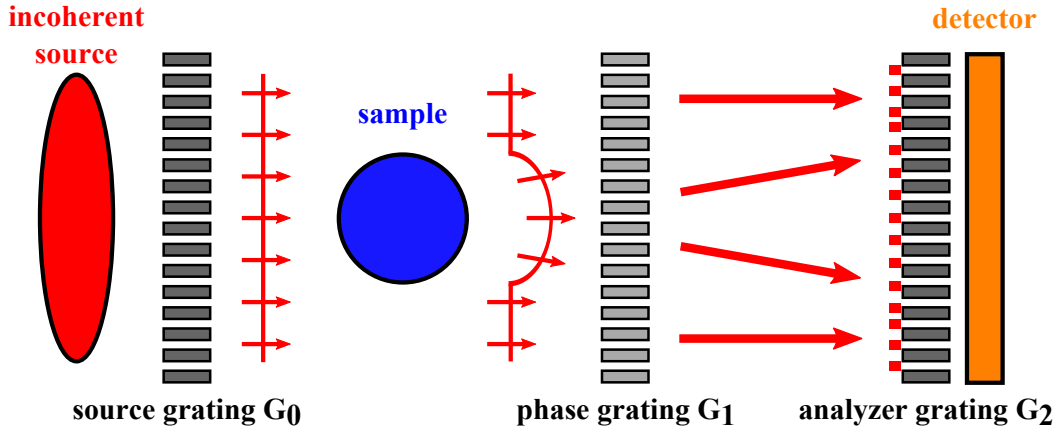


Figure 2.2: Schematic drawing of a Talbot-Lau interferometer. The small red arrows indicate the incoming wave front and the distorted wave front after passing through the sample. The thick red arrows and the small red rectangles in front of the G_2 grating indicate the resulting displacement of the interference pattern due to the distortion of the wave front.

2.2.3 Phase stepping routine

The signal extraction with the presented grating interferometer is realized by a so-called phase stepping routine [53]. In this procedure, either one of the three gratings is moved relative to the other gratings in the direction x_g perpendicular to the propagation direction of the X-ray beam. The grating is scanned over one period (g_2) of the G_2 grating, with a finite number of steps (≥ 3) and at each grating position an image is taken. Thereby, the interference pattern is sampled at a finite number of points in each detector pixel, which is demonstrated for eight phase steps per period by the thick black dots in the intensity curves of Figure 2.3. The recorded intensity in each pixel is called a stepping curve and can be approximated by the first two terms of a Fourier series [2]:

$$I(x_g) = a_0 + a_1 \cos\left(\frac{2\pi}{g_2} x_g + \phi_1\right), \quad (2.7)$$

where a_0 is the offset, a_1 the amplitude, and ϕ_1 the transverse shift of the intensity distribution. These three parameters can be obtained from the stepping curve by Fourier analysis.

By comparing the parameters of the stepping curve from a reference stepping routine without a sample in the beam (denoted with a superscript r) and the parameters from the stepping curve with a sample in the beam (denoted with a superscript s), the following imaging signals can be extracted simultaneously for each pixel:

- The relative attenuation of the sample, as depicted in Figure 2.3 a), is given by

$$a_0 = \frac{a_0^s}{a_0^r}. \quad (2.8)$$

This imaging modality, which is referred to as the AMP signal throughout this the-

sis, is based on the same contrast mechanism as conventional attenuation-based X-ray imaging.

- The relative transverse shift of the stepping curve, is given by

$$\phi_1 = \phi_1^s - \phi_1^r. \quad (2.9)$$

As shown in Figure 2.3 b), the relative transverse of the interference pattern is related to the angular refraction of the X-ray beam. For a distance d_2 between the phase and the analyzer grating, this relation is given by [2]

$$\alpha = \frac{g_2}{2\pi} \frac{\phi_1}{d_2}. \quad (2.10)$$

It can be deduced from Equation 2.6 and Equation 2.10 that the relative transverse shift of the intensity distribution is related to the differential phase shift of the wave front by

$$\phi_1 = \frac{d_2 \lambda}{g_2} \frac{\partial \Phi(x)}{\partial x}. \quad (2.11)$$

Consequently, this imaging modality is known as the differential phase contrast (DPC) signal.

- The visibility of a stepping curve is defined as $V = a_1/a_0$. Therefore, the relative visibility of the interference pattern is given by [32]

$$V = \frac{V^s}{V^r}. \quad (2.12)$$

The reduction of the visibility can be explained by small-angle scattering of the X-ray beam at sub-pixel sized structures in the sample, as depicted in Figure 2.3 c). This imaging modality is called X-ray dark-field imaging and is referred to in this thesis as the DCI signal.

The standard radiographic images in the three contrast modalities are based on the summation of the respective quantity along the beam direction through the sample and represent two-dimensional projection images of the object. They are called AMP, DPC, and DCI projections throughout this thesis.

2.3 X-ray Computed Tomography

X-ray Computed Tomography (CT) is an imaging technique to non-destructively retrieve information about the inner structure of a three-dimensional object. The technique was developed by Allan McLeod Cormack and Sir Godfrey Hounsfield, for which they were awarded the Nobel Prize in Physiology or Medicine in 1979. For a more detailed introduction to tomographic methods and tomographic reconstruction algorithms, the reader is referred to [46, 20]. Here, only a brief summary of the mathematical basics of CT reconstruction for

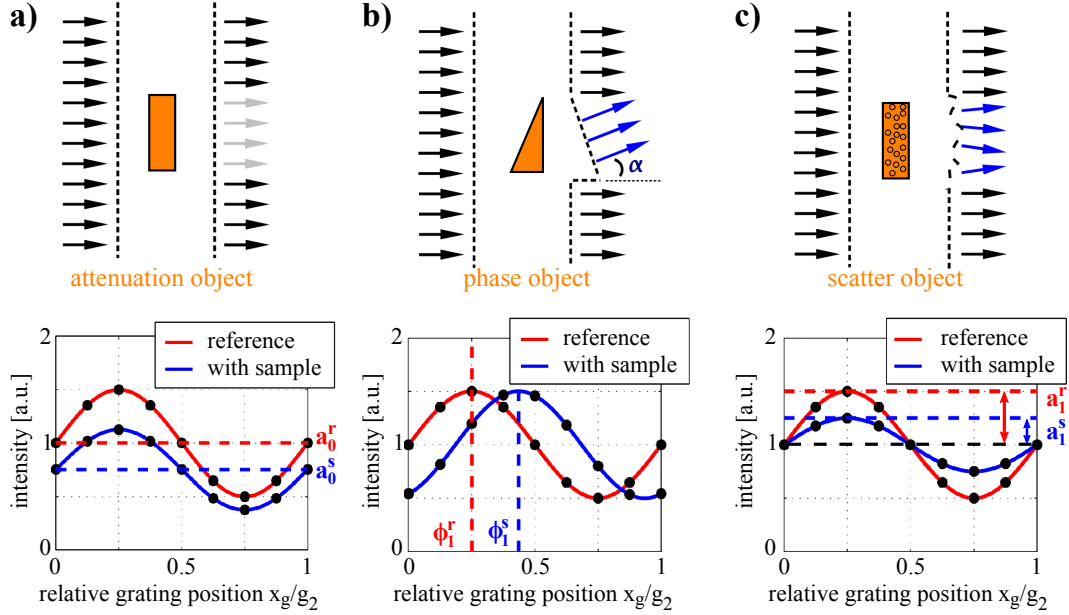


Figure 2.3: Phase stepping procedure and resulting contrast modalities. **a)** The decrease of the mean value (dashed lines) of the stepping curve is equal to the relative attenuation of the sample. **b)** The relative transverse shift of the stepping curve is related to beam deflections caused by a differential phase shift of the wave front traversing the sample. **c)** The amplitude decrease of the stepping curve is related to small-angle scattering of the X-ray beam at sub-pixel sized structures in the sample. Figure adapted from [8].

parallel beam geometry is given. The description is restricted to two dimensions but can be easily expanded to three dimensions by considering the three-dimensional object as a stack of individual slices.

2.3.1 Radon Transform

The mathematical foundation of tomography was laid by Johann Radon in 1917 [38]. A line integral represents the integral of a parameter of the object along a line L with a certain angle θ and distance t from the origin, as depicted in Figure 2.4. Such a line can be parametrized for the given two-dimensional representation of the object $f(x, y)$ by

$$L_\theta(t) : x \cos \theta + y \sin \theta = t, \quad (2.13)$$

and thereby the line integral or one-dimensional projection of the function $f(x, y)$ can be defined as

$$P_\theta(t) = \int_{L_\theta(t)} f(x, y) ds. \quad (2.14)$$

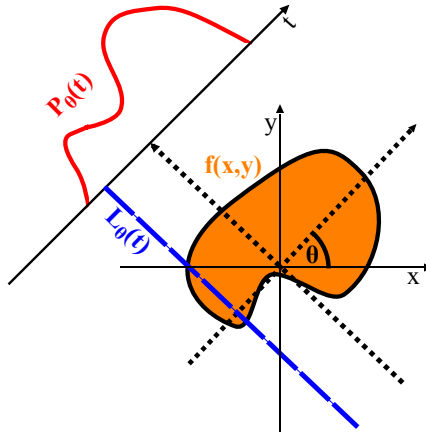


Figure 2.4: Projection $P_\theta(t)$ at a projection angle θ of a given object that is represented by $f(x, y)$. Figure adapted from [45].

This equation can be rewritten using a Dirac delta function as

$$P_\theta(t) = \int_{-\infty}^{\infty} \int_{-\infty}^{\infty} f(x, y) \delta(x \cos \theta + y \sin \theta - t) dx dy. \quad (2.15)$$

$P(\theta, t)$, as a function of θ and t , is known as the *Radon Transform* of the function $f(x, y)$ and basically transforms a two-dimensional object into its angular projections. Since this transform is symmetric, the full information about the object is contained in projections over a range π of projection angles. The *Radon Transform* can be visualized by a sinogram, which displays the projection $P_\theta(t)$ for each angle θ as a horizontal line of gray values. This is depicted in Figure 2.5.

2.3.2 Fourier Slice Theorem

The reconstruction of the object function from the projections, also known as the *inverse Radon Transform*, is an exact mathematical transformation based on the *Fourier Slice Theorem*, which is stated as [46]:

The Fourier transform of a parallel projection of an image $f(x, y)$ taken at angle θ gives a slice of the two-dimensional transform $\tilde{f}(u, v)$, subtending an angle θ with the u-axis.

The *Fourier Slice Theorem* is illustrated in Figure 2.6; mathematically, it can be formulated by

$$\tilde{P}_\theta(w) = \mathcal{F}[P_\theta(t)], \quad (2.16)$$

$$\tilde{f}(u, v) = \mathcal{F}[f(x, y)], \quad (2.17)$$

$$\tilde{P}_\theta(w) = \tilde{f}(w \cos \theta, w \sin \theta), \quad (2.18)$$

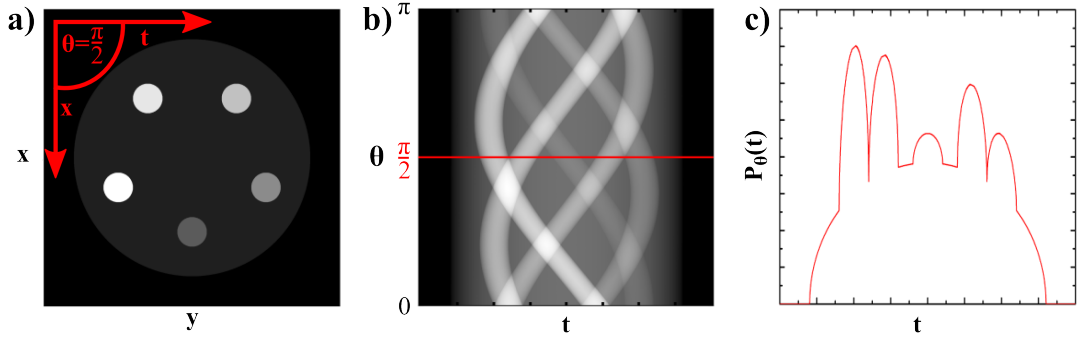


Figure 2.5: Visualization of the Radon Transform. **a)** Two-dimensional object function $f(x, y)$ in gray value representation. **b)** Corresponding Radon Transform in sinogram representation. Each horizontal line of the sinogram represents a projection $P_\theta(t)$ of $f(x, y)$ with a different angle θ . **c)** Line profile of projection with 90° angle between x -axis and t -axis as indicated in a) and b). Figure adapted from [45].

where u , v , and w are the corresponding Fourier space coordinates to the real space coordinates x , y , and t . Consequently, the *Fourier Slice Theorem* provides an analytical solution for the reconstruction of a continuous object from its projections. However, in practice, only a finite set of projection angles and detector pixels are available, and therefore only a discrete representation of the Fourier transform in polar coordinates can be obtained. The density of the radial sample points in Fourier space decreases for increasing spatial frequencies, as indicated by the circles in Figure 2.6. As a consequence of this, interpolation to a Cartesian coordinate system is necessary, before the inverse Fourier transform of $\tilde{f}(u, v)$, and thereby the object function, can be calculated.

2.3.3 Filtered Backprojection

Instead of interpolation, an algorithm known as *Filtered Backprojection* (FBP) can be used to reconstruct the object function from the projection data. In this method, the Fourier transforms of the projections are filtered with a frequency filter $|w|$ prior to taking the inverse Fourier transform \mathcal{F}^{-1} . The object function is then given by the integral of the filtered projections in real space over a range of π :

$$f(x, y) = \int_0^\pi \mathcal{F}^{-1} [\tilde{P}_\theta |w|] d\theta. \quad (2.19)$$

In practice, the linear ramp filter $|w|$, also called a *Ram-Lak* filter, is often replaced by other filters, such as a *Shepp-Logan* or a *Hamming* filter, in order to suppress high frequency noise [46].

In attenuation-based X-ray Computed Tomography the *Filtered Backprojection* algorithm is used to reconstruct the distribution of the linear attenuation coefficients of a sample from a set of projection images acquired at varying projection angles. Furthermore, the FBP can

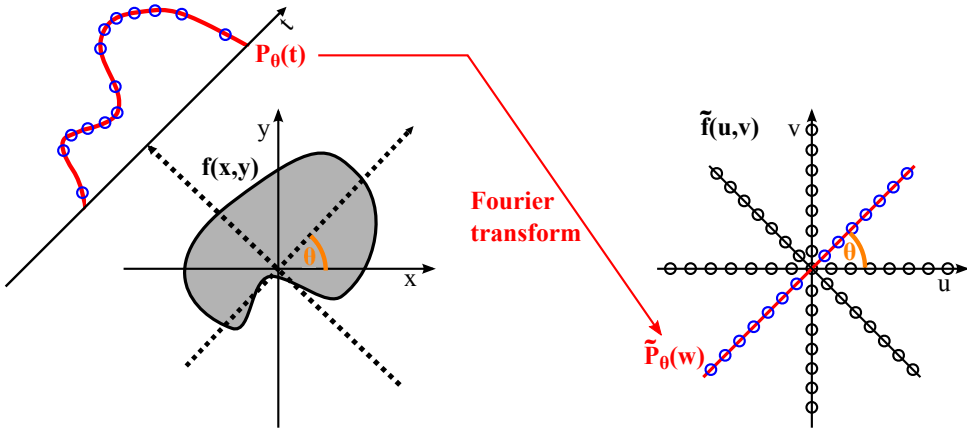


Figure 2.6: Visualization of the Fourier Slice Theorem. The Fourier transform of a parallel projection of an object $f(x,y)$ at an angle θ is equal to a slice at an angle θ through the two-dimensional Fourier space $\tilde{f}(u,v)$.

be used to reconstruct the distribution of the decrement of the real part of the refraction index δ and thereby the phase shift of the object in each voxel. For the case of grating-based phase contrast imaging, where the projection images are differential phase shift data, this requires the replacement of the *Ram-Lak* filter in the FBP integral by an imaginary *Hilbert* filter [33, 2].

As mentioned before, the presented formulas are only valid for a parallel geometry, a detailed description of the reconstruction in the case of cone beam geometry can be found in [46, 20].

2.4 Signal, contrast, and noise

Measured imaging data are always subject to signal fluctuations, which are generally referred to as noise. For a given mean value of signal M , the noise is commonly defined as the standard deviation of the mean value σ . The signal-to-noise ratio (SNR) is then given by [5, 50]

$$SNR = \frac{M}{\sigma}. \quad (2.20)$$

The contrast between two individual features i and j of an image is basically given by the modulus of the difference of the mean values of the corresponding signals $|M_i - M_j|$. Consequently, the contrast-to-noise ratio (CNR) can be defined as [51]

$$CNR = \frac{|M_i - M_j|}{\sqrt{\sigma_i^2 + \sigma_j^2}}. \quad (2.21)$$

A detailed discussion about the different sources of noise in the attenuation and phase images, obtained with the scanner, is presented in Chapter 4.

2.5 Spatial system response

In this section, a brief introduction to the concepts of linear system theory with respect to the characterization of imaging systems is given. For a detailed theoretical treatment of this topic, the reader is referred to [7, 16, 55]. Here, only the basic quantities are introduced with focus on the particular case of real and radially symmetric response functions, which represents the experimental setup used for the measurements of the spatial system response in this work. Moreover, the resolution measures used to characterize the spatial resolution of the system are presented.

2.5.1 Response function in real space and frequency space

A common approach to describe the spatial system of imaging systems is provided by the concepts of linear system theory. An imaging system is defined to be linear if the principle of superposition can be applied to the system, meaning that the overall response to a linear combination of stimuli, also called input signals, is simply the same linear combination of the individual responses, also called output signals. Furthermore, a system is said to be shift invariant if the only effect caused by a shift in the position of the input is an equal shift in the position of the output [16]. For a linear and shift invariant system (LSI), the output can be calculated from the input by convolution:

$$i(x, y) = s(x, y) \otimes o(x, y) = \int_{-\infty}^{\infty} \int_{-\infty}^{\infty} s(x - x', y - y') o(x', y') dx' dy', \quad (2.22)$$

where the symbol \otimes designates two-dimensional convolution. The output $i(x, y)$ describes the recorded two-dimensional image and $o(x, y)$ describes the object. The convolution kernel $s(x, y)$ is known as the point spread function (PSF) of the system. The PSF describes the system response to an input signal with the shape of a Dirac delta function and hence gives the intensity distribution that is recorded for a point-like object. The PSF is typically normalized to unity:

$$\int_{-\infty}^{\infty} \int_{-\infty}^{\infty} s(x, y) dx dy = 1, \quad (2.23)$$

which means that the integral intensity in the image is unchanged by the convolution operation. This is equivalent to describing a system with efficiency of unity [14].

The *Convolution Theorem* states that the convolution of two functions in real space is given by the point wise product of the Fourier transforms in frequency space [16], consequently the image in Fourier space is given by

$$\tilde{i}(u, v) = \tilde{s}(u, v) \times \tilde{o}(u, v), \quad (2.24)$$

where u and v are the corresponding Fourier space coordinates to the real space coordinates x and y , and the symbol \times designates point wise multiplication. The Fourier transform $\tilde{s}(u, v)$ of the point spread function is called optical transfer function (OTF) and is generally defined

as

$$\tilde{s}(u, v) = \tilde{m}(u, v) e^{i\Psi(u, v)}, \quad (2.25)$$

where $\Psi(u, v)$ is called the phase transfer function (PTF) and $\tilde{m}(u, v) = |\tilde{s}(u, v)|$ is known as the modulation transfer function (MTF). For the case of a real and radially symmetric PSF $s(t)$ that only depends on the radial distance t from the origin, the corresponding OTF is also real and radially symmetric [22, 16]. Therefore, the system response in frequency space is fully described by the modulation transfer function $\tilde{m}(w)$ that only depends on the radial spatial frequency w .

Furthermore, if the system response is a superposition of n responses from individual components of the linear imaging system, the modulation transfer function of the entire system is given by

$$\tilde{m}(w) = \prod_{i=1}^n \tilde{m}_i(w), \quad (2.26)$$

which corresponds to a convolution product of the corresponding point spread functions in real space.

2.5.2 Line spread function

The line spread function (LSF) is generally defined as the spatial system response to a line-shaped input signal. Assuming that the line object is parallel to the y-axis and is defined as

$$o_L(x, y) = \delta(x), \quad (2.27)$$

the line spread function $LSF(x)$ is given by [14]

$$LSF(x) = s(x, y) \otimes o_L(x, y) \quad (2.28)$$

$$= \int_{-\infty}^{\infty} \int_{-\infty}^{\infty} s(x - x', y - y') \delta(x') dx' dy' \quad (2.29)$$

$$= \int_{-\infty}^{\infty} s(x, y') dy', \quad (2.30)$$

where $s(x, y)$ is the point spread function of the system. Consequently, the line profile described by $LSF(x)$ is equal to the projection of the point spread function along the y-axis.

For the particular case of a radially symmetric point spread function, the line spread function only depends on the radial distance t and the spatial system response is fully described by

$$\tilde{m}(w) = \mathcal{F}[LSF(t)]. \quad (2.31)$$

2.5.3 Edge spread function

The edge spread function (ESF) is generally defined as the spatial system response to an edge-shaped input signal. Assuming that the edge object is aligned parallel to the y-axis and

is defined as

$$o_E(x, y) = o_E(x) = \begin{cases} 0 & \text{for } x < 0 \\ 1 & \text{else} \end{cases}, \quad (2.32)$$

the edge spread function $ESF(x)$ is given by [14]

$$ESF(x) = s(x, y) \otimes o_E(x, y) \quad (2.33)$$

$$= \int_{-\infty}^{\infty} \int_{-\infty}^{\infty} s(x - x', y - y') o_E(x') dx' dy' \quad (2.34)$$

$$= o_E(x) * LSF(x), \quad (2.35)$$

where the symbol $*$ designates one-dimensional convolution. Considering that the derivative of a convolution product of two functions is given by the convolution of either function with the derivative of the other, the derivative of $ESF(x)$ is given by

$$\frac{d}{dx} ESF(x) = \frac{d}{dx} [o_E(x) * LSF(x)] = \delta(x') * LSF(x) = LSF(x). \quad (2.36)$$

For a radially symmetric PSF this leads to

$$\frac{d}{dt} ESF(t) = LSF(t), \quad (2.37)$$

and thereby Equation 2.31 can be reformulated to

$$\tilde{m}(w) = \mathcal{F} \left[\frac{d}{dt} ESF(t) \right]. \quad (2.38)$$

This means that the spatial system response is fully characterized by a single edge profile.

2.5.4 Resolution measures

Despite the fact that the point spread function or modulation transfer function fully characterize the spatial system response of an LSI system, it is sometimes more convenient to describe the system resolution by a single parameter, a so-called resolution measure. In this work, three different resolution measures are used.

A commonly used resolution measure [10, 14] is based on the spatial frequency f_{10} , at which the MTF of the systems falls below 10%, and is defined as

$$\text{MTF 10\%} = \frac{1}{2f_{10}}. \quad (2.39)$$

This resolution measure is particularly sensitive to high-frequency components of the spatial system response.

A line spread function with the shape of a single Gaussian distribution can be uniquely described by its full width at half maximum (FWHM). In this thesis, the line spread functions

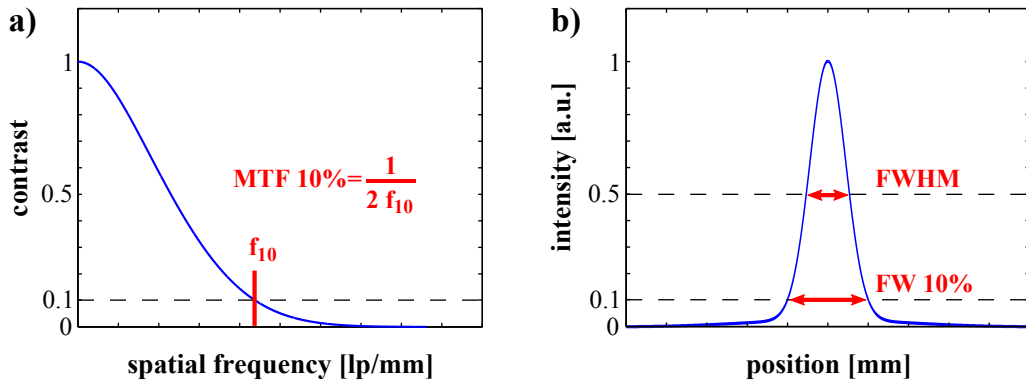


Figure 2.7: Resolution measures. **a)** 10% MTF is based on the spatial frequency f_{10} at which the modulation transfer function drops below 10%. The spatial frequency is given in line pairs per millimeter. **b)** FWHM and FW at 10% of the corresponding line spread function.

are assumed to be a linear combination of two Gaussian distributions and therefore cannot be described uniquely by their FWHM. Consequently, an additional resolution measure is introduced that is defined as the full width at 10% of the LSF (FW 10%). This resolution measure is particularly sensitive to low-frequency components of the spatial system response that are expressed by the tails of the LSF. The different resolution measures are illustrated in Figure 2.7.

3 Experimental setup



Figure 3.1: Photograph of small animal phase contrast CT scanner and control PC equipped with special software suitable for the acquisition modes of the scanner.

The small animal phase contrast CT scanner presented in this work, was developed and built by a cooperation between *Technische Universität München* and *Bruker microCT*, Kontich, Belgium (formerly *Skyscan*), as industrial partner. In a first step, a small animal gantry system for X-ray phase contrast Computed Tomography was developed. In a second step, the gantry system was slightly redesigned and incorporated into a standard micro-CT housing in order to be operated in rotating gantry mode and thereby providing the possibility of in-vivo phase contrast CT imaging of small animals. The scanner is controlled by software from *Bruker microCT* that was developed to be suitable for the acquisition modes of the scanner.

A detailed description of the stepwise development, including the technical challenges for the translation from bench-top system with rotating sample to a rotating gantry system can be found in [50, 51, 52]. First experimental results have demonstrated that quantitatively correct CT scans of biological samples in phase and attenuation contrast can be performed with the scanner [50, 52]. Moreover, a first projection-based in-vitro study of excised murine lungs has provided evidence that X-ray dark-field images obtained with the scanner can be used

to improve the diagnosis of pulmonary emphysema [58]. The feasibility of radiographic imaging of a living mouse with the phase contrast CT scanner has recently been proven by [4]. Furthermore, a first preclinical in-vivo study investigating the visualization of pulmonary emphysema in living mice using dark-field radiography, has been recently conducted with the scanner [30].

In this chapter, the basic features of the small animal phase contrast CT scanner are described and the relevant technical details are given.

In Figure 3.2, technical drawings and corresponding photographs of the scanner and the gantry are shown. The gantry can be rotated around the animal bed (B) and includes a flat panel detector (D), an X-ray tube (T), and a Talbot-Lau interferometer. The bed is mounted on a positioning stage that allows precise translation along the rotation axis of the gantry. The dimensions of the scanner housing (Fig. 3.2 c)) are approximately 95 cm in width, 100 cm in height, 85 cm in depth. The source-to-detector distance is approximately 47 cm. All other relevant distances can be found in Figure 3.3.

The X-rays in the scanner are generated by a tungsten-target X-ray tube (MCBM 65B-50 W, RTW, Neuenhagen, Germany) with an approximate focal spot size of $50 \times 50 \mu\text{m}^2$ [44].

Furthermore, the scanner features a visible light camera to monitor the animal during in-vivo imaging and appropriate facilities for monitoring of physiological functions. Breathing movement, temperature, and an electrocardiogram can be recorded, and the animal can be heated by airflow from an installed heated fan.

Grating interferometer

The grating interferometer is operated in the first fractional Talbot distance with a $\pi/2$ -shifting phase grating and a design energy of 23 keV. The source grating (G_0) was introduced to provide sufficient transverse coherence at the position of the phase grating (G_1). The analyzer grating (G_2) is positioned in contact with the detector. The different imaging signals are extracted by the phase stepping routine described in Section 2.2.3. The phase stepping is performed with the source grating by using a piezo scanner (P-712, *Physik Instrumente PI*, Karlsruhe, Germany [36]). In order to allow for precise alignment of the gratings, additional movements are motorized: The source grating can be rotated around the z-axis (notation of axes as indicated in Fig. 3.2 b)). The phase grating can be rotated around the z-axis, tilted around the x-axis and the y-axis, and translated along the z-axis. The analyzer grating is stationary.

In Figure 3.3, a schematic drawing of the cone beam setup is depicted including the approximate distances between the individual components. Due to the cone beam geometry the sensitivity of the interferometer is reduced by a factor r_1/l with r_1 being the source-to-sample and l the source-to- G_1 distance [15]. All gratings were fabricated by *microworks*, Karlsruhe, Germany, using the LIGA process [24, 41]. The source grating is $1 \times 1 \text{ cm}^2$ in size, while the phase and the analyzer grating have a round shape with a diameter of 7 cm.

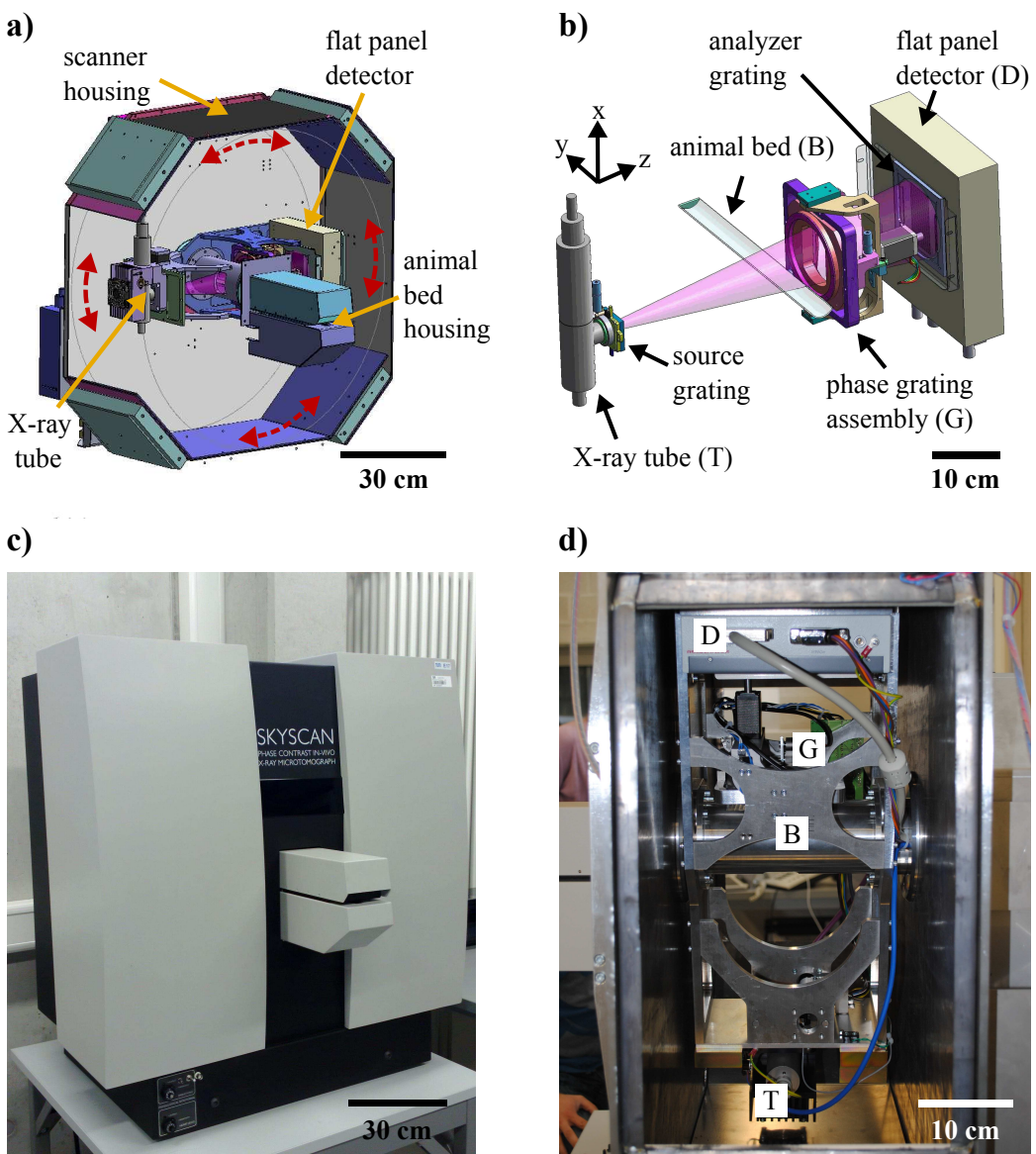


Figure 3.2: Small animal phase contrast CT scanner. **a)** Technical drawing of the scanner housing with rotating gantry (gantry movement indicated by the red arrows). **b)** Technical drawing of the grating interferometer within the gantry. **c)** Photograph of the small-animal phase contrast CT scanner. **d)** Photograph of the gantry showing the detector (D), phase grating assembly (G), animal bed position (B), and X-ray tube source (T). Panel a), b) and d) of this figure are adapted from [50].

The periods (g) and heights (h) of the used gratings are:

- Source grating G_0 (gold): $g_0 = 10 \mu\text{m}$, $h_0 = 35 \mu\text{m}$.
- Phase grating G_1 (nickel): $g_1 = 3.24 \mu\text{m}$, $h_1 = 4.0 \mu\text{m}$.
- Old analyzer grating G_2 (gold): $g_2 = 4.8 \mu\text{m}$, $h_2 = 25 \mu\text{m}$.
- New analyzer grating G_2 (gold): $g_2 = 4.8 \mu\text{m}$, $h_2 = 45 \mu\text{m}$.

Please note that the same G_0 and G_1 grating were used for all presented results in this thesis, whereas two G_2 gratings with different gold heights of the grating structures were used during the experiments. The grating with the higher gold structure, which is referred to as the new G_2 grating in this thesis, causes an increase of the shadowing effect that leads to a drop of intensity towards the left and right margins of the field of view (FOV), but provides a higher overall visibility in the FOV compared to the grating with lower gold structures, which is referred to as the old G_2 grating. In Table 3.1 the approximate mean visibilities in the FOV of the scanner for both G_2 gratings are displayed as a function of peak voltage of the X-ray tube. The visibility of the interferometer decreases when the deviation between the design energy of the interferometer and the effective energy for a certain peak voltage increases.

Peak voltage [kVp]	Old G_2 grating Visibility [%]	New G_2 grating Visibility [%]
30	25	37
35	19	30
40	15	24
45	12	20
50	10	16

Table 3.1: Mean visibilities in relation to the applied peak voltage for different G_2 gratings.

Detector

The flat panel sensor (C9312SK-06, *Hamamatsu*, Japan), used to record the images, is positioned in contact with the G_2 grating. The detector features a GOS scintillator and 2396×2304 pixels with a pixel size of $50 \times 50 \mu\text{m}^2$. This corresponds to a photosensitive area of $124.8 \times 115.2 \text{ mm}^2$ [18]. Since the effective FOV at the detector position depends on the size of the analyzer grating (7 cm round), the size of a typical rectangular raw image is limited to approximately 1150×900 pixel, which translates into a cone beam angle of approximately 7 degree perpendicular to the gantry rotation axis and 5 degree along the rotation axis. Due to the cone beam geometry, the effective pixel size at the position of the sample is $29 \times 29 \mu\text{m}^2$ and the effective FOV is approximately $3.5 \times 2.5 \text{ cm}^2$.

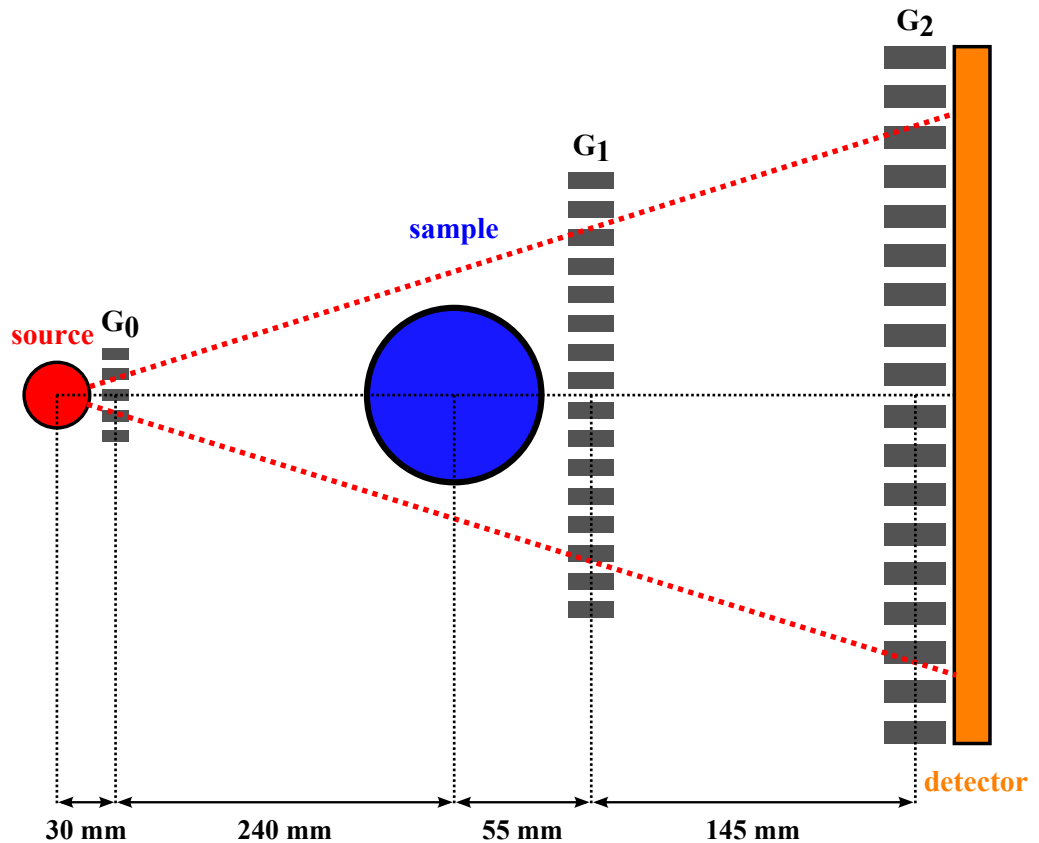


Figure 3.3: Schematic drawing of the setup including X-ray source, detector, sample and a grating interferometer with three gratings: Source grating (G_0), phase grating (G_1), and analyzer grating (G_2). The approximate distances between the individual components of the setup are given in mm. The analyzer grating is positioned in contact with the detector. Figure adapted from [50].

The acquisition software of the scanner generally features two image acquisition modes for the X-ray camera. In the snap-mode, the image acquisition of the detector is triggered by an input signal, whereas the camera continuously records images in the grab-mode. To ensure correct exposure times in grab-mode, the software provides the possibility to skip the first frame of the acquisition cycle. In principle, the snap-mode provides a higher acquisition speed than the grab-mode and is therefore the preferred acquisition mode. However, during the experiments it was found that acquisition in snap-mode led to severe stripe artifacts in some of the recorded images and consequently the acquisition mode was changed. In this

work, three different versions of the *Skyscan* acquisition software were used:

- *Version 1*: image grab-mode, first frame skipped¹.
- *Version 2*: image snap-mode².
- *Version 3*: image grab-mode, first frame skipped³.

More information about the acquisition settings and the processing and reconstruction routines used in this work can be found in Chapter A.

¹ Skyscan1190.exe

² Skyscan1190.exe

³ Skyscan1190.exe. Skip first frame option = "true"

4 Analysis of contrast-to-noise ratio

4.1 Data acquisition

The basic idea of this measurement was to record images of the same object for various settings of the scanner and to analyze the image quality of the resulting images in order to find the ideal settings for each contrast modality. A phantom of three different plastic rods was used for the measurements, as displayed in Figure 4.1 a). The rods were made of polymethylmethacrylate (PMMA), polytetrafluoroethylene (PTFE), and polyvinyl chloride (PVC). The particular materials were chosen due to their different attenuation and phase shifting properties. The diameter of each rod was roughly 5 mm¹ and the phantom was constructed to fit into a 50 ml Falcon tube, as shown in Figure 4.1 b).

4.1.1 Acquisition of projection images

For projection measurements, the Falcon tube with the phantom was filled with air and was attached to the sample stage in such a way that only the Falcon tube containing the phantom was in the field of view. The reason for this was to circumvent the influence of the animal bed on the resulting projection images. The phantom was aligned in such a manner that the full profiles of the three plastic rods could be seen clearly separated from each other for the given gantry angle and all projection images were recorded for the same position. In total, about 130 different setup configurations were used to image the phantom. The different acquisition parameters are discussed in Section 4.3. The standard Fourier processing routine was used to retrieve the attenuation and differential phase contrast signals². Since the acquisition mode of the detector used to record the majority of the raw images was occasionally defective, some of the processed AMP and DPC images showed severe artifacts, mainly in the form of entire pixel columns with constantly wrong values³. To counteract this issue and to ensure statistical reliable results, ten artifact-free projections were acquired for each setup configuration. The analysis of the projection data is described in Section 4.2.1.

4.1.2 Acquisition of CT data

For CT measurements, the Falcon tube was filled with water to avoid phase wrapping, which is caused by a strong phase shift between the phantom and air and which can affect the reconstructed CT slices [60]. Furthermore, the plastic container filled with water has approximately

¹ The exact diameters of the rods used are 5.38 mm (PMMA), 5.13 mm (PTFE) and 5.33 mm (PVC). These values were used for the analysis of the projection images.

² MATLAB processing script. More information can be found in Section A.1.1.

³ Version 2 of the acquisition software was used. More information can be found in Chapter 3.

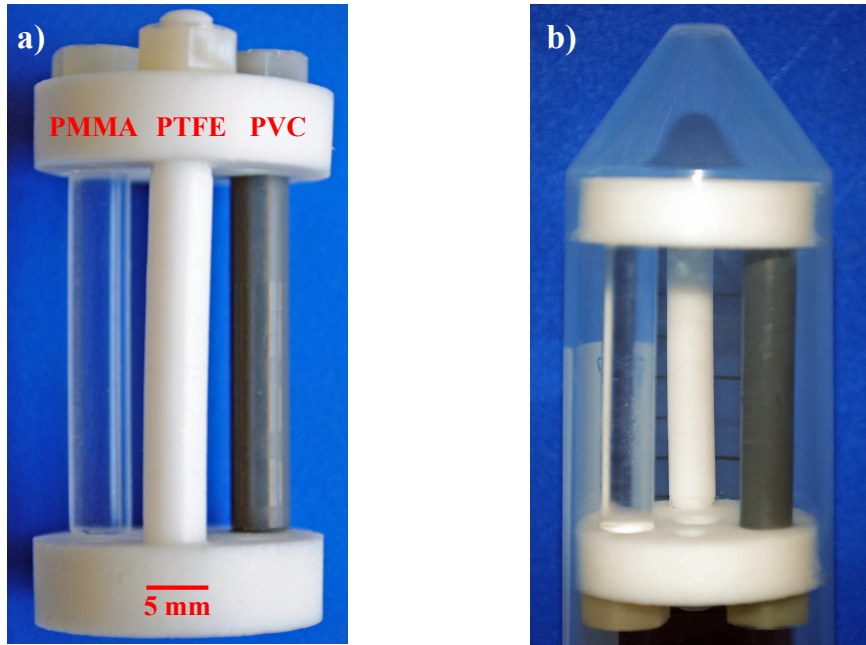


Figure 4.1: Photographs of the phantom. **a)** Photograph of the phantom consisting of a PMMA rod, a PTFE rod, and a PVC rod. **b)** Photograph of the phantom placed into a Falcon tube. The plastic container was filled with air for the projection acquisitions and with water for the CT acquisitions.

the same attenuation properties as a mouse and thus requires similar exposure times and X-ray energies. Due to the additional weight of the water, the plastic container was too heavy to be attached to the sample stage in the same way as for the projection measurements and therefore was placed on the bed of the scanner. To avoid the problems caused by the detector mode during the acquisition of the projection images, all CT data were acquired by using a different detector mode that did not show the mentioned artifacts⁴. In total 15 CT data sets with different acquisition parameters were acquired and the raw images were processed in the same way as the projection images. All CT data were reconstructed with a *Filtered Backprojection* algorithm. A *Hamming* filter was used to reconstruct the attenuation contrast slices and a *Hilbert* filter for the reconstruction of the phase contrast images. The reconstruction parameters, such as the correction parameter for the center of rotation or the windowing of the gray values for the respective contrast⁵, were identical. No beam hardening or ring artifact corrections were applied to make the reconstructed slices comparable.

⁴ Version 1

⁵ The gray values were chosen according to the histogram of the data set recorded at the lowest energy. Since this setting naturally has the broadest gray value range it was thereby ensured that all gray values of the recorded CT data sets lie within the chosen gray value window. Hence, there are no saturated pixels expected in the reconstructed slices, which could cause problems in the CNR analysis. More information can be found in Section A.2.1.

4.2 Data analysis

4.2.1 Analysis of projection images

The analysis of the AMP and the DPC projections yields several problems. For attenuation contrast projections, a straightforward region of interest (ROI) analysis of the contrast-to-noise ratios (CNRs), as described for the CT data, is generally possible, but not appropriate for the cylindrical geometry of the phantom. On the contrary, analysis of DPC projections by the standard method is generally not feasible due to the differential character of the signal, meaning that not the absolute phase shift but the first derivative of the phase is measured. Consequently, a line-by-line analysis of the data was applied.

In Figure 4.2 and Figure 4.3 the attenuation contrast and differential phase contrast images of the phantom in the plastic container are shown together with exemplary line profiles corresponding to the red lines in the images. The shown images were recorded at 45 kVp with 10 phase steps per projection and an exposure time of 5 s per phase step. The gain factor was 20%. Please note that, for the sake of consistency, all plots in this section are taken from this data set. The basic idea of the analysis is to fit analytical functions, describing the expected signal arising from the geometry of the sample, with one fit parameter that characterizes the strength of the signal. The goodness of the fit is used to estimate the noise of the signal. The region of interest for the following analysis comprises 100 consecutive lines for each image.

Analytical functions

Since the used rods have cylindrical shapes and the cylinder axes were aligned sufficiently parallel to the vertical axis of the detector, the analytical functions for the expected AMP and DPC line profiles can be determined by considering the behavior of the signals for the case that the X-ray beam passes through a massive circle with a constant complex index of refraction n . Moreover, a monochromatic parallel beam is assumed for the sake of simplicity. Assuming that the direction of the X-ray beam is parallel to the z-direction and the center of the circle lies in the origin of the xz-coordinate system, as illustrated in Figure 4.4, the path length of the beam through the sample can be formulated depending on the position on the x-axis and the radius R of the object:

$$d(x) = 2\sqrt{R^2 - x^2}. \quad (4.1)$$

According to the *Lambert-Beer Law* (Equ. 2.4) and Equation 4.1 the drop of intensity caused by a circular object with a constant attenuation coefficient μ is given by

$$I(x) = I_0 \exp(-\mu d) = I_0 \exp\left(-\mu 2\sqrt{R^2 - x^2}\right). \quad (4.2)$$

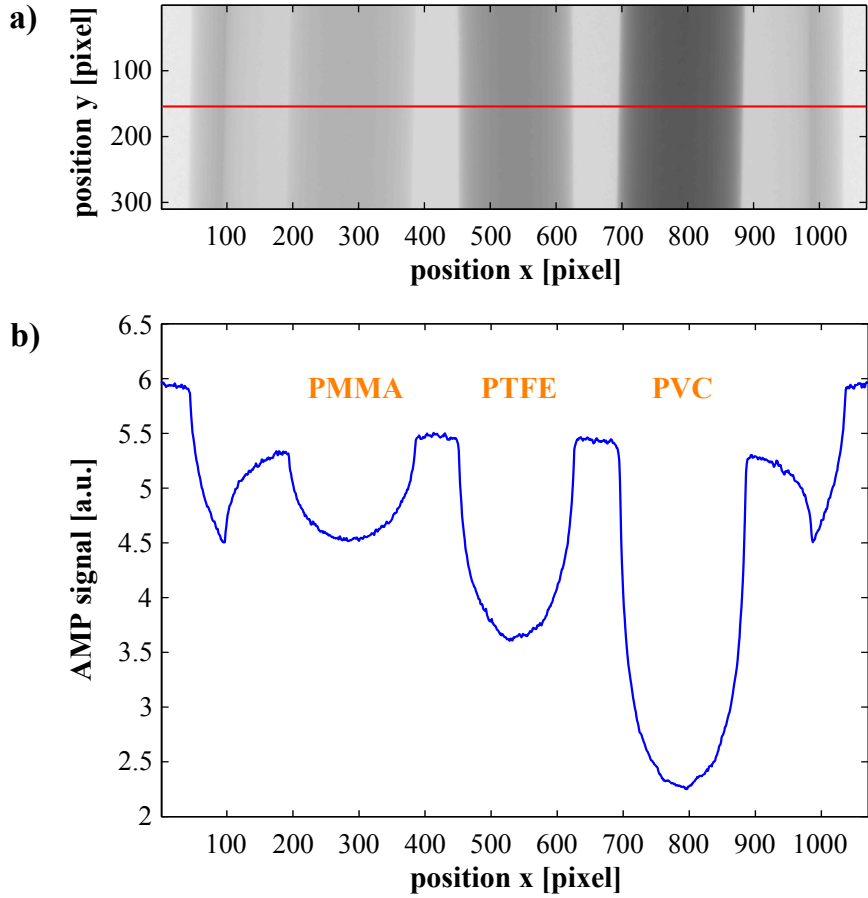


Figure 4.2: Attenuation signal from the phantom. **a)** Attenuation contrast image of the phantom placed into a Falcon tube. **b)** Line profile corresponding to the pixel row indicated by the red line in a).

The discrete form of this equation, where x is represented by an array containing the pixel values of a detector line, describes the expected line profile of the AMP signal when the beam passes through an object with a circular base, such as the rods used in the presented measurements⁶. This is demonstrated in Figure 4.4 a).

As stated in Equation 2.11, the DPC signal $\phi_1(x)$ can be expressed by

$$\phi_1(x) = \frac{d_2 \lambda}{g_2} \frac{\partial \Phi(x)}{\partial x}, \quad (4.3)$$

where g_2 is the period of the analyzer grating, d_2 the distance between the phase grating and the analyzer grating and λ the wavelength of the X-ray photons. The differential phase shift

⁶ The normalization with a reference image and the signal extraction from the phase-stepping routine has been ignored here for the sake of clarity. The transmission signal expected for the used processing with reference images is described by $a_0(x) = a_0^s/a_0^r = I_0^s/I_0^r \exp(-\mu 2\sqrt{R^2 - x^2})$.

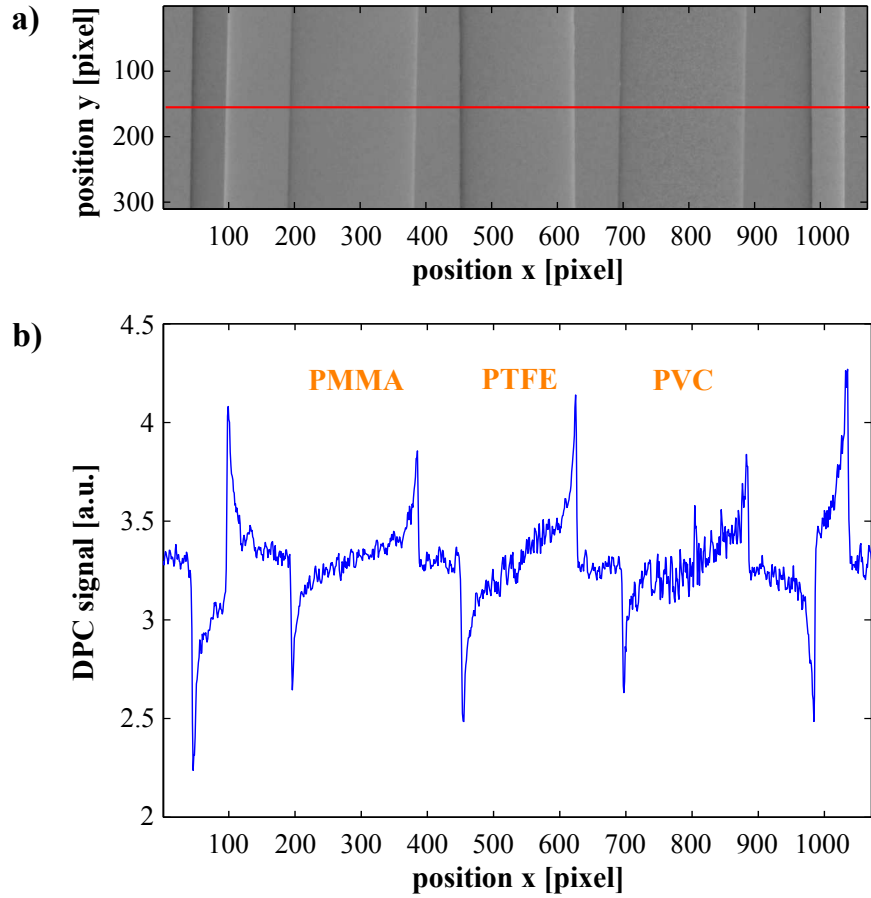


Figure 4.3: Differential phase signal from the phantom. **a)** Differential phase contrast image of the phantom placed into a Falcon tube. **b)** Line profile corresponding to the pixel row indicated by the red line in a).

for a circular object with radius R and a constant δ is given by

$$\frac{\partial \Phi(x)}{\partial x} = \delta \frac{2\pi}{\lambda} \frac{\partial d(x)}{\partial x} = -\delta \frac{2\pi}{\lambda} 2 \frac{x}{\sqrt{R^2 - x^2}}, \quad (4.4)$$

and thereby Equation 4.9 can be reformulated to

$$\phi_1(x) = -\frac{4\pi d_2 \delta}{g_2} \frac{x}{\sqrt{R^2 - x^2}}. \quad (4.5)$$

For the analytical solution, the values of the DPC signal approach infinity when x goes to $\pm R$. This, naturally, is not true for the case when the signal consists of discrete pixel values. Aside from that, the equation describes the expected line profile of the DPC signal, as depicted in Figure 4.4 b).

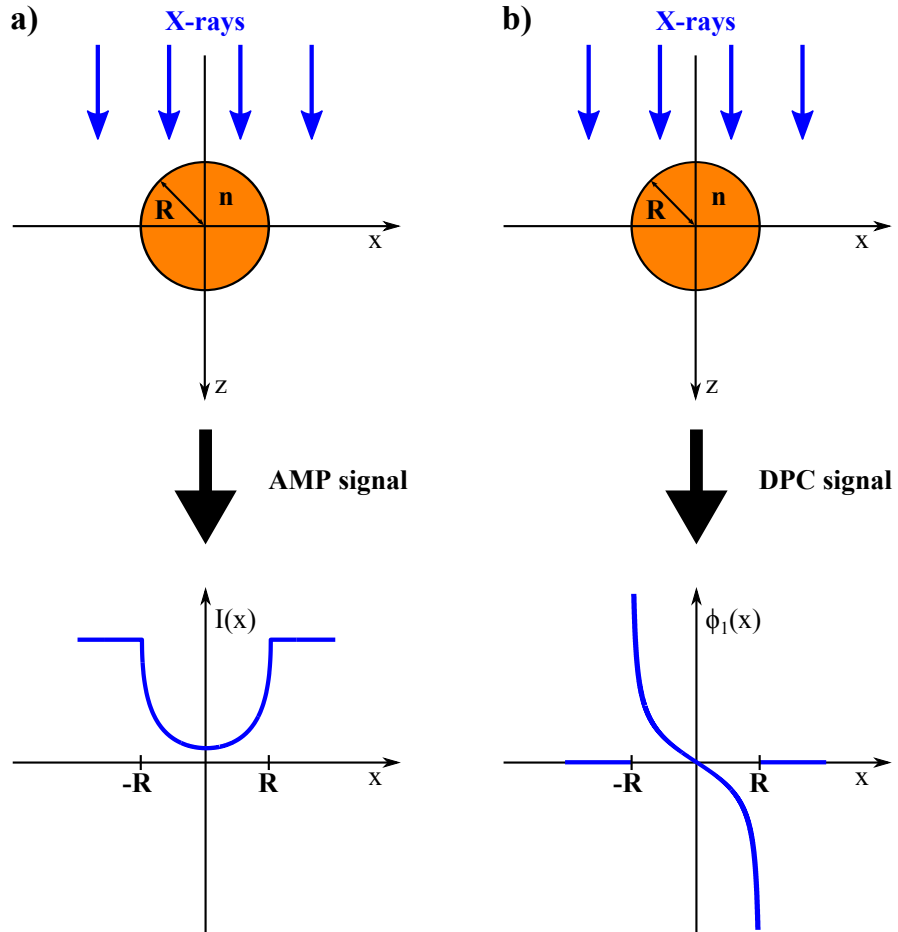


Figure 4.4: Schematic drawing of attenuation and differential phase contrast signal for a circular object with radius R and constant refractive index n . **a)** Expected line profile for the AMP signal $I(x)$ after traversing the sample. **b)** Expected line profile for the DPC signal $\phi_1(x)$ after traversing the sample. Please note that the denomination of the axes of the coordinate system are chosen to be x and z to indicate the translation to three dimensions, where x and y represent the horizontal and vertical axis of the detector or the object plane, while z is the beam direction.

The obtained analytical functions are the foundation for the used fit functions in the line-by-line analysis of the AMP and DPC images. Please note that the progression of the DPC signal in the analyzed images (Fig. 4.3) is mirror inverted to the signal described here. This is due to the fact that the signal in the used processing script is defined with the opposite sign.

Signal of the Falcon tube

The AMP and DPC signals of the phantom in Figure 4.2 and Figure 4.3 are overlaid with the respective signal from the Falcon tube. This can be easily seen from the line profile of the AMP signal. The strongest impact can be observed towards the lateral margins of the sample where the path length through the wall of the plastic container gets longer and thereby the attenuation due to the plastic tube increases significantly. Since this would lead to problems in the further analysis, the contributions of the Falcon tube to the AMP and DPC signals were determined. As the Falcon tube can geometrically be described in two dimensions by a ring, the analytical fit functions to describe the signals of the tube can be found by using a superposition of the already deduced functions for circular objects⁷. The obtained analytical functions were then fitted to the data points of the line profiles in regions where only the Falcon tube contributed to the signals, as demonstrated in Figure 4.5.

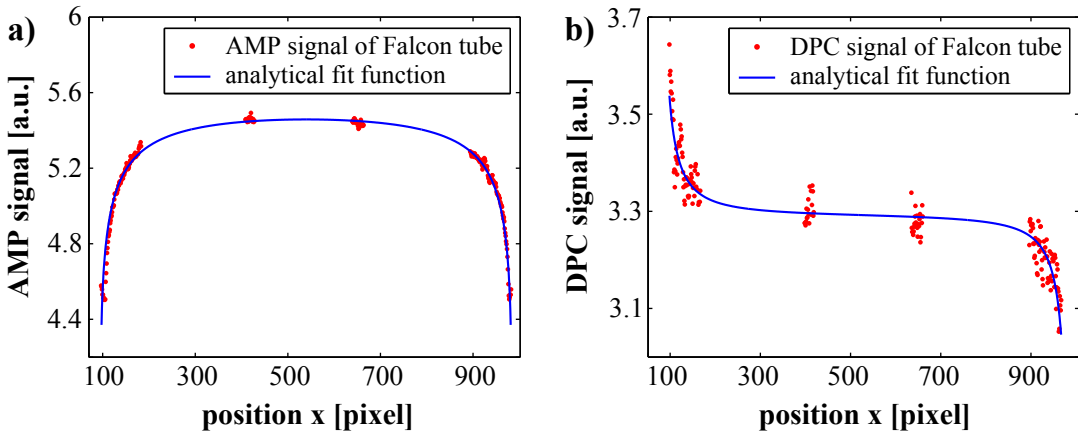


Figure 4.5: Fitting of the obtained analytical functions to the attenuation and differential phase signals from the Falcon tube. **a)** Analytical fit function (blue curve) deduced from the geometrical shape of the tube, fitted to the AMP signal of the tube without the phantom (red dots). **b)** DPC fit function (blue curve) fitted to the corresponding signal of the Falcon tube (red dots). The scaling of the x-axis was chosen to make the fitted regions easier comparable to the line plots of the original signal in Figure 4.2 and Figure 4.3.

The gained analytical forms of the Falcon tube signals were used to isolate the signals from the three rods. The differences between the original and the corrected AMP and DPC signals are shown in Figure 4.6. The corrected signals were used as the basic input for all following analysis steps.

⁷ The center of the Falcon tube fit was determined manually and used for all lines analyzed in one image, since the falcon tube was aligned sufficiently parallel to vertical axis of the detector. The used radius of the tube was also constant, as the small deviations due to the slightly conical form of the tube can be neglected for the used ROI.

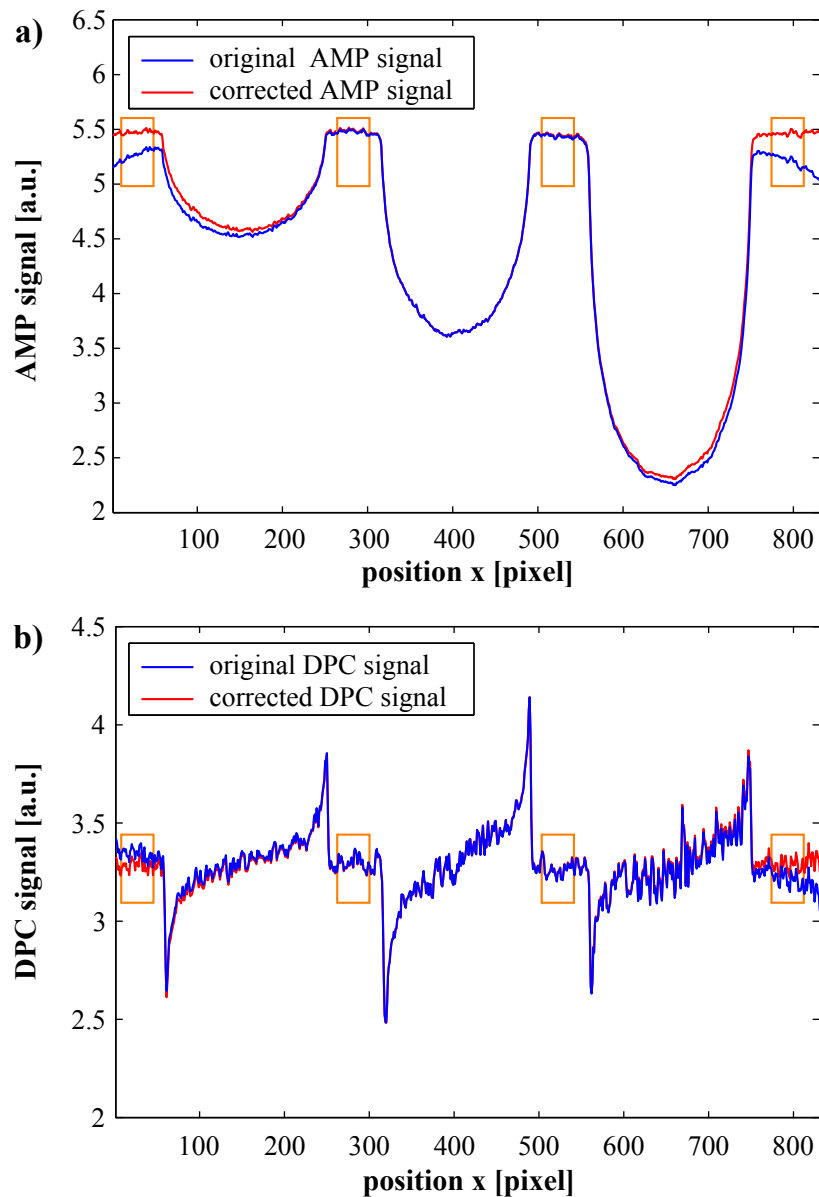


Figure 4.6: Comparison of the original signals and the isolated signals from the three rods in the used line profile representation. **a)** Original AMP signal including the signal of the Falcon tube (blue) and the corrected signal (red). **b)** Original DPC signal (blue) and corrected signal (red). The orange rectangles indicate the regions used to quantify the background intensity of the AMP signal and the background noise in both contrast modalities.

Determination of the origins of the fit functions

The exact center of the corresponding rod for each analyzed line was calculated from the corrected AMP signal. For each of the three rods, an interval was defined large enough to compensate for the slight deviation of the rod axes from the vertical axis of the detector within the region of interest. Thereby, the same interval could be used for all analyzed lines of the respective rod in the entire region of interest. In analogy to a center of mass calculation, the origin of the intensity distribution within this interval was obtained by calculating the point at which the relative position vectors of the pixels, weighted with their attenuation values, sum up to zero. This was done separately for each line and the found center points were also used for the analysis of the DPC images.

Fitting of the attenuation signal

The adjusted fit function for the attenuation signal based on the analytical functions deduced in Section 4.2.1 is given by

$$A_r(x) = A_0 \exp\left(-a_r \sqrt{R_r^2 - (x - center_r)^2}\right). \quad (4.6)$$

The index r indicates that the same formula, adjusted to the respective plastic rod was used for the fitting. A_0 was obtained by averaging the values of the line profile in regions not influenced by the sample, as indicated by the orange rectangles in Figure 4.6, and was the same for all rods. R_r is the radius of the respective rod in pixel scaling, and $center_r$ stands for the position of the center of the rod in sub-pixel precision, as calculated beforehand. The variable a_r is the free fit parameter used to characterize the strength of the respective signal. As input for the fitting, 80 pixels to the left and to the right of the calculated center pixel of the rod (rounded value of the determined center) were chosen. The particular size of the interval arises from the fact that it was also used for the DPC images to have comparable statistics. Compared to the diameters of the rods, which are about 180 pixels, the interval was sufficiently large to do a reliable fit but small enough to prevent problems in the fitting process of the DPC signal at the edges of the rods where the fit function approaches infinity. In Figure 4.7, the fitting procedure is depicted for the three plastic rods. For the case of PMMA and PTFE, the fitting was in good agreement with the data and the deviation of the data can be interpreted as high frequency noise due to the Poisson distribution of the X-ray photons and other high frequency noise contributions. Consequently, the root-mean-square error (RMSE) of the regression was a suitable parameter to characterize the noise of the signal since it practically describes the standard deviation of the data from the expected signal. In contrast, the strong beam hardening artifact in the center region of the PVC signal (Fig. 4.7 c)) led to a vertical shift of the entire fit function and thereby made the fit useless for the characterization of the noise. Therefore, a polynomial function was additionally fitted to the PVC data and the RMSE from this fit was used to characterize the noise of the PVC signal.

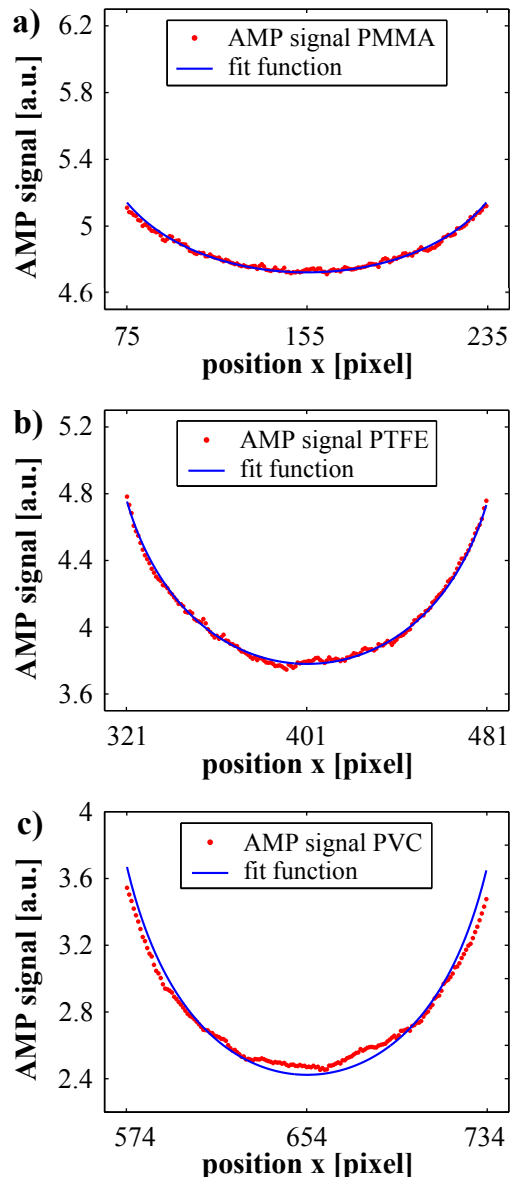


Figure 4.7: Fitting of the obtained analytical functions to the attenuation signal from the rods. **a)** Signal of PMMA rod (blue) and fit function (red). **b)** Signal of PTFE rod (blue) and fit function (red). **c)** Signal of PVC rod (blue) and fit function (red).

Fitting of the differential phase signal

The fit function of the DPC signal is given by

$$P_r(x) = P_{0r} + P_{0r} \frac{p_r (x - center_r)}{\sqrt{R_r^2 - (x - center_r)^2}}. \quad (4.7)$$

The offset P_{0r} was determined independently for each rod, by calculating the mean value of the corresponding fit interval. R_r is the radius of the respective rod in pixel scaling, and $center_r$ stands for the exact position of the center of the rod. The variable p_r is the free fit parameter used to characterize the strength of the DPC signal. As mentioned before, the intervals for the input of the fit were the same as used for the attenuation signal. In Figure 4.8, the fitting procedure of the DPC signal for the three rods is shown. The deviation of the data from the fit function can be explained as high frequency photon noise for all three rods, consequently the RMSE of the respective regression was used to characterize the noise of the signal. From the comparison of Figure 4.7 and Figure 4.8, it can be observed that the relative noise of the DPC signal is generally higher than for the AMP signal. This is discussed further in Section 4.3.

Contrast-to-noise ratio definition

The figures of merit to characterize the contrast-to-noise ratios of the AMP and the DPC signal of the rods were defined by

$$\text{AMP : } CNR_r = \frac{a_r 2R_r}{\sqrt{(RMSE_r)^2 + (RMSE_0)^2}}, \quad (4.8)$$

$$\text{DPC : } CNR_r = \frac{p_r}{\sqrt{(RMSE_r)^2 + (RMSE_0)^2}}. \quad (4.9)$$

The parameter $RMSE_r$ describes the noise of the signal from the respective rod while $RMSE_0$ is the standard deviation from the regions outside the phantom, as demonstrated in Figure 4.6, and is consequently the same for all rods. Please note that the free fit parameters a_r and p_r comprise different parameters and thus need different normalization. The attenuation CNR is normalized by the diameter of the respective rod to make it a unitless quantity, whereas this step was unnecessary for the phase CNR, since the free parameter p_r is already unitless. Consequently the obtained values from the AMP and the DPC formula are not comparable to each other.

Please note that the figures of merit defined here are different from the standard definition of the CNR, as given in Equation 2.21, and the absolute values are not comparable at all. Nevertheless, the information about the image quality is practically the same, since the free parameter of the fit basically describes the difference between the signal from the background and the signal from the sample, and thereby the contrast, while the denominator of the equation represents the noise characteristics of the background and of the sample signal, in analogy to the denominator in the standard CNR formula.

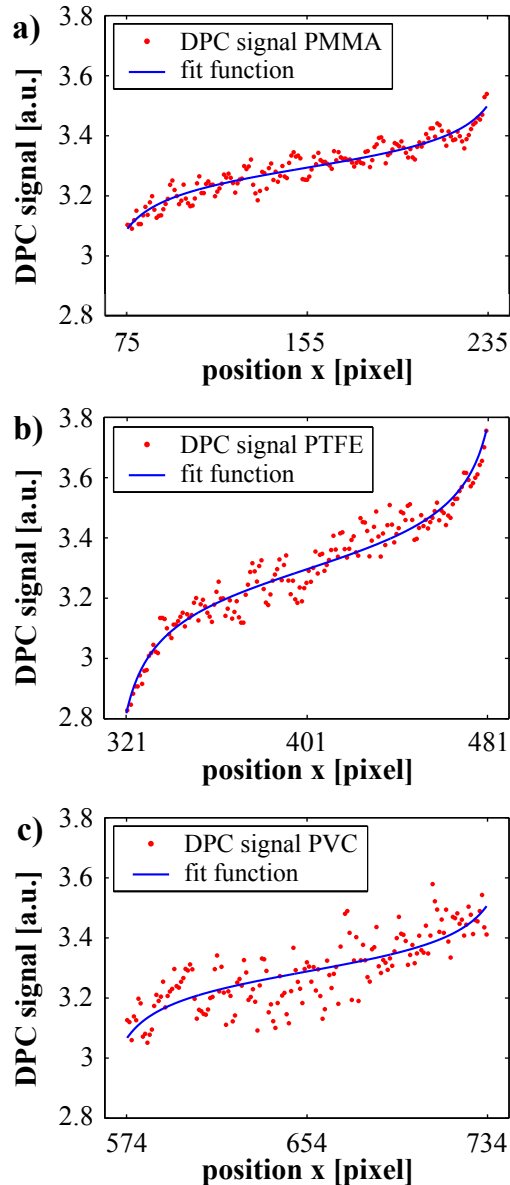


Figure 4.8: Fitting of the obtained analytical functions to the differential phase signal from the rods. **a)** Signal of PMMA rod (blue) and fit function (red). **b)** Signal of PTFE rod (blue) and fit function (red). **c)** Signal of PVC rod (blue) and fit function (red).

Averaging

All the analysis steps described here were executed separately for each of the 100 lines of the region of interest and the average CNR was calculated. Moreover, the entire procedure was repeated for ten projections, recorded for the same settings, to cancel out variations in the acquisition process of the images, such as the quality of the flat-field images or the phase stepping routine. Consequently, the final result of the analysis provides a statistically reliable value for the CNR of the respective contrast modality⁸.

Error estimation

An estimation of the relative error of the CNR values was determined based on the 95% confidence interval of the respective fit parameter. The standard errors of the RMSE of the fit and the standard deviation of the background were ignored in these considerations, since they can be assumed to be negligible in comparison to the confidence interval of the fit. The relative errors of the AMP contrast-to-noise ratios are very small (< 1%) for all presented results and can be practically neglected in the following sections. In contrast, the relative errors of the DPC results depend strongly on the applied acquisition settings and the material of the respective rod, and therefore have to be considered in the following sections. In general, it can be stated that the PTFE rod provided the most reliable result for the DPC CNR due to its attenuation and phase shifting properties. Moreover, the PTFE rod is placed at the center of the FOV where the remaining influence of the Falcon tube (that could not be compensated for with the Falcon tube correction) is at its weakest.

⁸ To shorten the computing time of the total analysis process for ten images, the used *MATLAB* routine was parallelized. This reduced the computing time by a factor of 7, resulting in a total computing time per acquisition setting of roughly 20 minutes.

4.2.2 Analysis of CT data

The CT data were analyzed with a region of interest analysis, as commonly used to characterize the contrast-to-noise ratio of CT slices [51, 57]. Square regions at the center of the individual rods in the transverse slices of the CT reconstruction were selected and a region outside the Falcon tube was chosen as reference region. The particular size of the regions was chosen to be relatively small compared to the diameter of the rods in order to reduce influences of the cupping effect, caused by beam hardening, on the calculations of the mean values and standard deviations. The chosen ROIs are indicated by the colored rectangles in Figure 4.9. To get statistically more reliable results, 100 adjacent transverse slices were averaged and

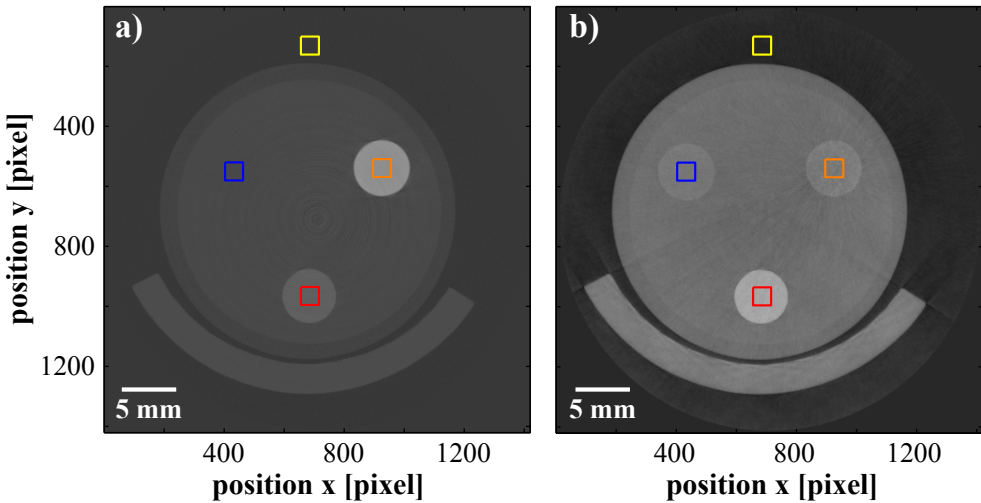


Figure 4.9: Reconstructed transverse CT slices with regions of interest used for the CNR analysis. **a)** Attenuation contrast. **b)** Phase contrast. Regions of interest for the PMMA rod (blue rectangle), PTFE rod (red rectangle), PVC rod (orange rectangle), and the background intensity (yellow rectangle).

the mean values and standard deviations were subsequently calculated from effective ROIs with a size of $60 \times 60 \times 100$ voxels. According to Equation 2.21, the contrast-to-noise ratios between the respective rod and the reference region in the two imaging modalities were calculated by

$$CNR_r = \frac{M_r - M_{air}}{\sqrt{\sigma_r^2 + \sigma_{air}^2}}, \quad (4.10)$$

with M_r being the mean value of the respective signal from the selected region of interest for a particular rod and σ_r the associated standard deviation. Accordingly, M_{air} and σ_{air} are the mean value and the standard deviation of the respective signal from the reference region.

The uncertainty of the CNR was determined by applying standard error propagation to Equation 4.10. The required uncertainties for the calculations are the standard error (SE) for each mean value ($SE_{mean} = \frac{\sigma}{\sqrt{N}}$) and the standard error of the corresponding standard deviation ($(SE_\sigma = \frac{\sigma}{\sqrt{2N}})$) [37]. N denotes the number of voxels in the corresponding ROI.

SECTION 4.2: DATA ANALYSIS

The calculated uncertainty of the CNR was smaller than $\pm 1\%$ for all presented results regardless of the contrast modality and the rod material and can consequently be neglected in the discussion of the results.

4.3 Results and discussion

In this section, the results of the analysis of the projection images and CT slices are presented and the impact of the respective parameters on the quality of the obtained images is discussed. The results from the projection images are named AMP CNR and DPC CNR, whereas the CT results are called CNR attenuation CT and CNR phase CT. Please note that the absolute values of the projection results are not comparable to the CT results, since the analysis was completely different. Depending on the respective purpose, the CNR results of projection and CT data are given either as absolute values (solid polygons) or as relative values that are normalized relative to the maximal CNR of the respective rod (hollow circles, crosses).

For reasons of clarity, no error bars are shown in the plotted results. In general, the calculated errors of the contrast-to-noise ratios from the CT measurements are very small and can be neglected for practical considerations. This is also valid for the error estimation of the CNR values obtained from the AMP projections. Since the error estimations of the DPC projections results are relatively large and depend on the applied acquisition settings and the material of the respective rod, they are given in the text of the corresponding section.

Furthermore, it is important to mention that for all projection and CT acquisitions the current of the X-ray tube was set to its maximum value, which depends on the applied peak voltage. Thus, a change of the peak voltage does not only result in a different X-ray spectrum but also in a change of photon flux hitting the detector. The exact parameters for each acquisition are listed in Chapter A. In the following sections, only the respective peak voltages are given. Moreover, the majority of the presented results was acquired with the same gratings and consequently the grating properties are not mentioned individually for each result. For a few results a different G₂ grating was used, which is mentioned in the respective sections. If not stated explicitly in the text, the projection images were recorded by using *Version 2* of the acquisition software and the CT data sets by using *Version 1* of the software.

4.3.1 CNR versus gain

Results

In this section, the calculated contrast-to-noise ratio of projection images acquired with different gain settings are compared. For each acquisition configuration in terms of photon flux and energy, projections were recorded for all reasonable gain settings ranging from 20% to 100% in steps of 20%. For instance, at 30 kVp and 10 s exposure per phase step, projections were acquired for 60%, 80%, and 100%, as lower gain settings resulted in underexposed raw images. Underexposure is defined throughout this work as the circumstance that the minimal transmission in the transmission profile of the acquisition software for a raw image of the sample is approximately 0%. On the contrary, for 45 kVp and 3.3 s exposure per step, projections could only be acquired for 20% and 40%, since higher gain settings led to overexposed raw images. Overexposure is defined as the case that the maximal transmission in the transmission profile for the flat-field image, associated with a particular projection acquisition, is approximately 100%.

In order to estimate the influence of the gain parameter on the CNR of the images, con-

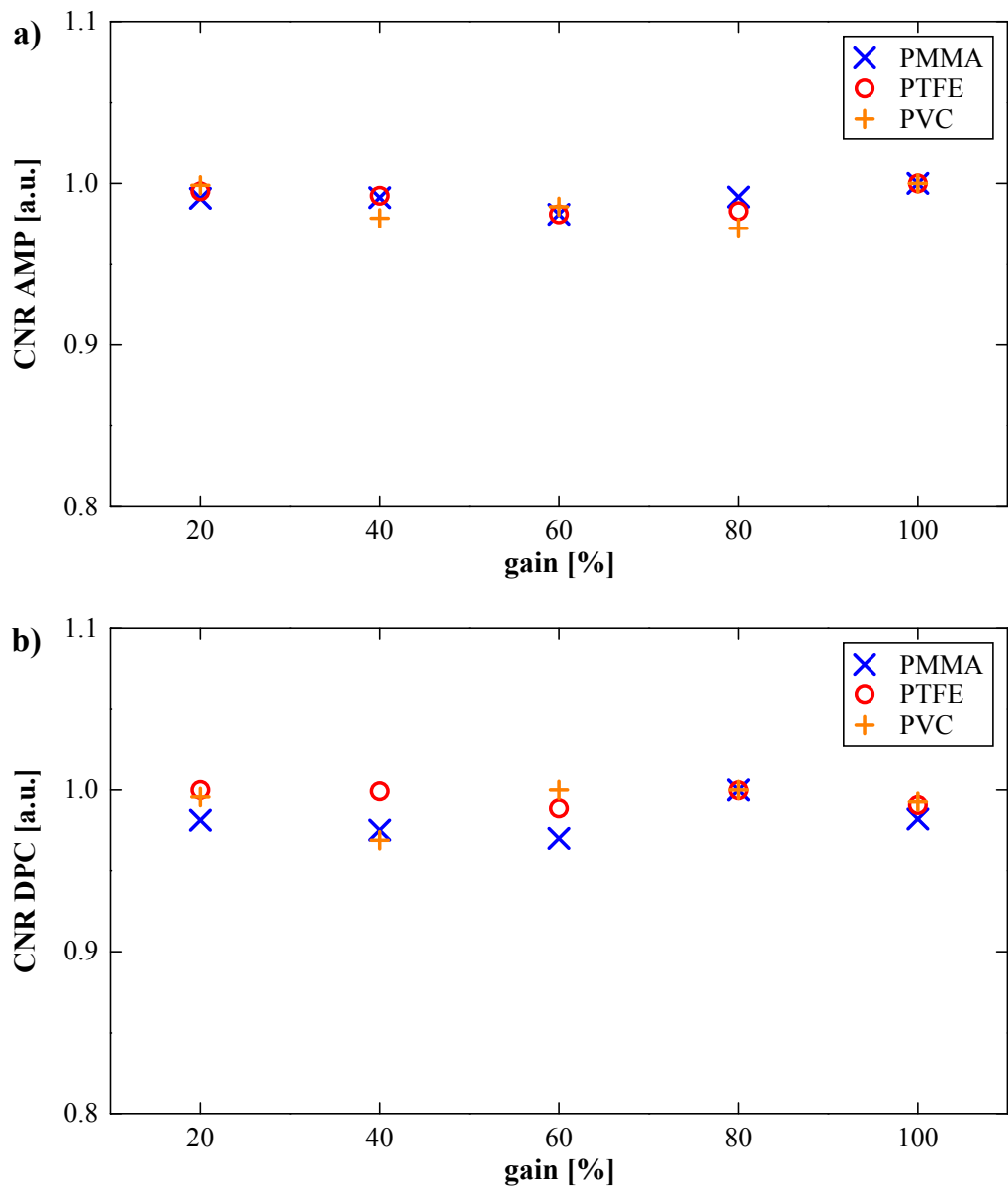


Figure 4.10: CNR vs. gain in projection mode.

a) AMP CNR. **b)** DPC CNR. The displayed results are mean values based on several different acquisition settings, as explained in the text. The values are normalized relative to the maximum value of the respective rod.

figurations were selected, for which the entire gain range produced reasonable results⁹. The CNR results of a particular configuration and rod were then normalized to unity and the normalized results for all used configurations were added up and normalized to unity again. Consequently, the results presented in Figure 4.10 are the mean CNR values for the respective rod, obtained by averaging the CNR of 50 images at each gain setting. Considering the scaling of the y-axis in the displayed plots, one finds that all calculated values deviate at the most 3% from the max value. The estimated relative error (see Sec. 4.2.1) of the DPC CNR for PMMA ranged from $\pm 5.4\%$ for 33 kVp and 10 s exposure to $\pm 11\%$ at 48 kVp and 1 s exposure. Respectively, the error for the CNR of PTFE ranged from $\pm 4.2\%$ to $\pm 8\%$, and the error of PVC from $\pm 11\%$ to $\pm 30\%$. The large relative errors for the DPC results explain why the deviations from the maximal values are slightly larger for the DPC CNR than for the AMP CNR, in particular for the PMMA and PVC rods.

Discussion

The found results indicate that the CNR is independent of the gain setting, within the accuracy of measurement. The influence of the gain parameter on the output signal of the used detector [19] is expressed by

$$U(t) = G \times Q(t). \quad (4.11)$$

Since the resulting output video signal voltage $U(t)$ is a product of the integrated charge $Q(t)$ and a constant gain factor G , the contrast and the noise in the acquired image are amplified by the same factor. Consequently, the gain setting is not expected to have any impact on the calculated CNR results, which is in good agreement with the presented results.

For practical applications, this means that the gain factor of the scanner can be chosen arbitrarily without any effect on the image quality. Due to fact that the CNR results are independent of the applied gain settings, the following results are presented without considering the applied gain factors.

4.3.2 CNR versus exposure

The total exposure of a projection image, which is defined here as the total number of photons reaching a particular detector pixel during the phase stepping routine, depends on the mean number of photons hitting the respective pixel per second, the number of phase steps, and the exposure time per step. For CT imaging, the total exposure of the data set depends additionally on the number of projection angles. In this section, the influences of the different parameters on the CNRs are investigated.

⁹ The used configurations were 33 kVp with 10 s exposure per step, 36 kVp with 5 s, 39 kVp with 3.3 s, 42 kVp with 2 s, and 48 kVp with 1 s. These were the only configuration, for which a gain factor of 20%, 40%, 60%, 80%, and 100% was reasonable. A table with all settings can be found in Section A.1.2.

Exposure time per phase step in projection mode

To estimate the influence of the exposure time per phase step on the resulting image quality of the projections, for each acquisition setting, in terms of peak voltage, projections with all reasonable exposure times were acquired. In Figure 4.11 and Figure 4.12, the CNR behavior in dependence on the exposure time per step is shown exemplarily for 36 kVp and 45 kVp; in both cases the images were acquired with 10 phase steps. The dashed line in the plots represents a square root function fitted to all data points of the corresponding figure. Hence, the results are more easily comparable to the theoretically expected behavior for mere statistical photon noise. This is explained further in the discussion of the presented results. The results indicate that the AMP CNR increases approximately as theoretically expected until reaching a certain level of total exposure. Above this threshold, the CNR increases only very slightly. In contrast, the DPC CNR increases roughly as theoretically expected for large exposure times and shows no saturation. The relative errors of the DPC results are decreasing with increasing exposure time and range from $\pm 9\%$ (2 s) to $\pm 4\%$ (10 s) at 36 kVp and $\pm 30\%$ (0.3 s) to $\pm 6\%$ (5 s) at 45 kVp for the PMMA rod. Correspondingly, the relative errors for the PTFE rod range from $\pm 7\%$ to $\pm 3\%$ at 36 kVp and from $\pm 17\%$ to $\pm 4\%$ at 45 kVp, and for the PVC rod from $\pm 28\%$ to $\pm 10\%$ at 36 kVp and from $\pm 78\%$ to $\pm 14\%$ at 45 kVp.

Exposure time per phase step versus number of phase steps in projection mode

In order to compare results with same total exposure but varying number of phase steps, the raw data of the projection images were also processed by using only every second phase step and thus reducing the total number of photons in each pixel by half. For 15 different acqui-

Contrast modality	Material	5 steps / 10 steps
AMP	PMMA	1.11 ± 0.07
	PTFE	1.11 ± 0.08
	PVC	1.13 ± 0.10
DPC	PMMA	1.18 ± 0.10
	PTFE	1.14 ± 0.08
	PVC	1.15 ± 0.09

Table 4.1: Comparison of CNR for the same total exposure but varying numbers of steps.

sition settings¹⁰, the ratio of the CNR from the processing with 5 steps to the corresponding result with half the exposure time per step and 10 steps were calculated. The averaged ratios

¹⁰ The particular acquisition settings for the comparison were selected to include the largest comparable range of acquisition parameters in terms of peak voltage and exposure times per step. For instance, at 33 kVp the results of 10 s exposure time for each of the 5 steps was compared to the original result of 5 s exposure time per 10 phase steps and at 45 kVp the results of 1 s and 2 s exposure time for each of the 5 steps were compared to the original results of 0.5 s and 1 s exposure time for each of the 10 steps. All compared settings are listed in Section A.1.4.

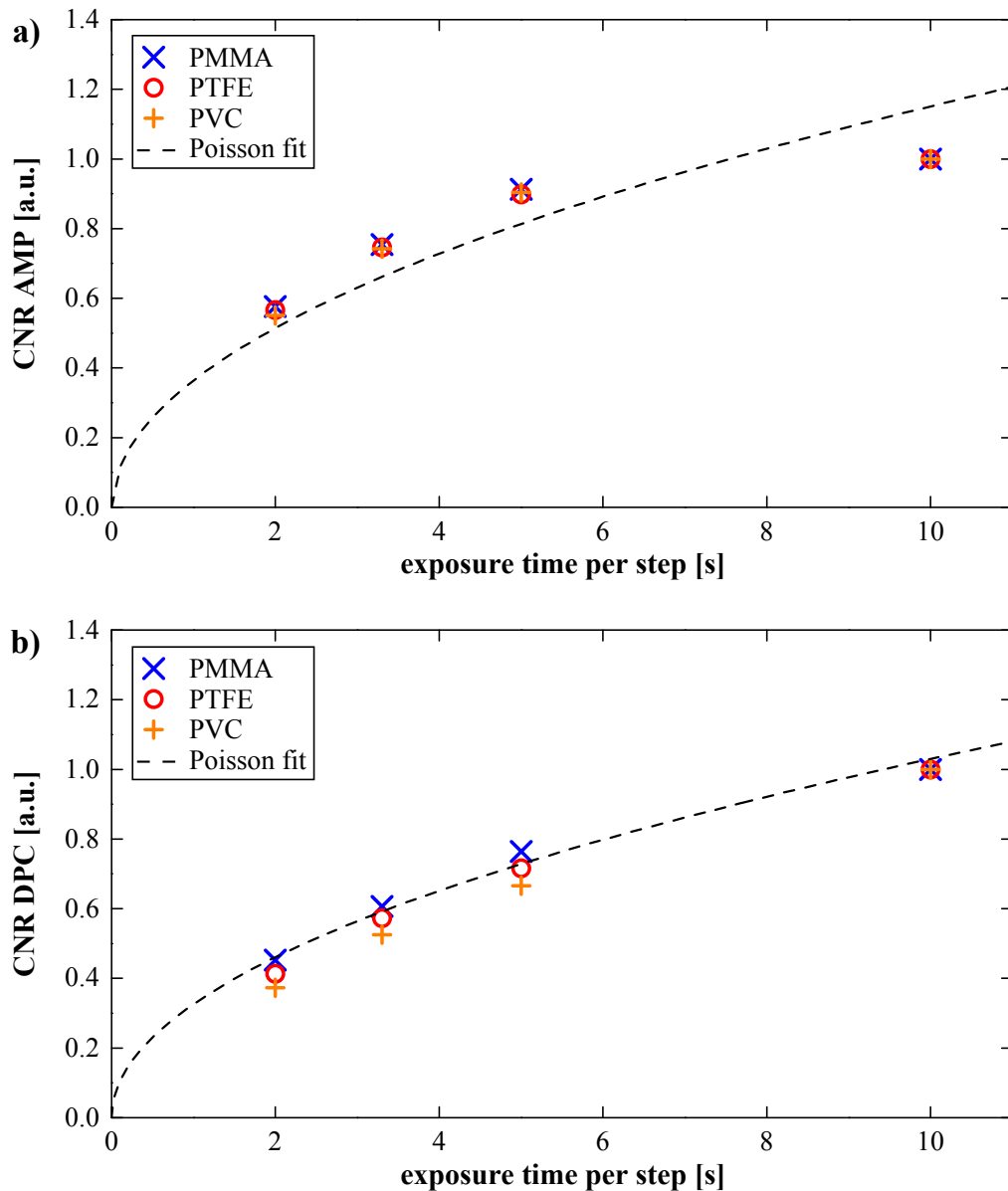


Figure 4.11: CNR vs. exposure time per phase step in projection mode at 36 kVp.

a) AMP CNR. **b)** DPC CNR. The projections were acquired with 10 phase steps. The dashed lines represent a square root function fitted to all data points of the respective plot. The displayed results are normalized relative to the maximum value of the respective rod.

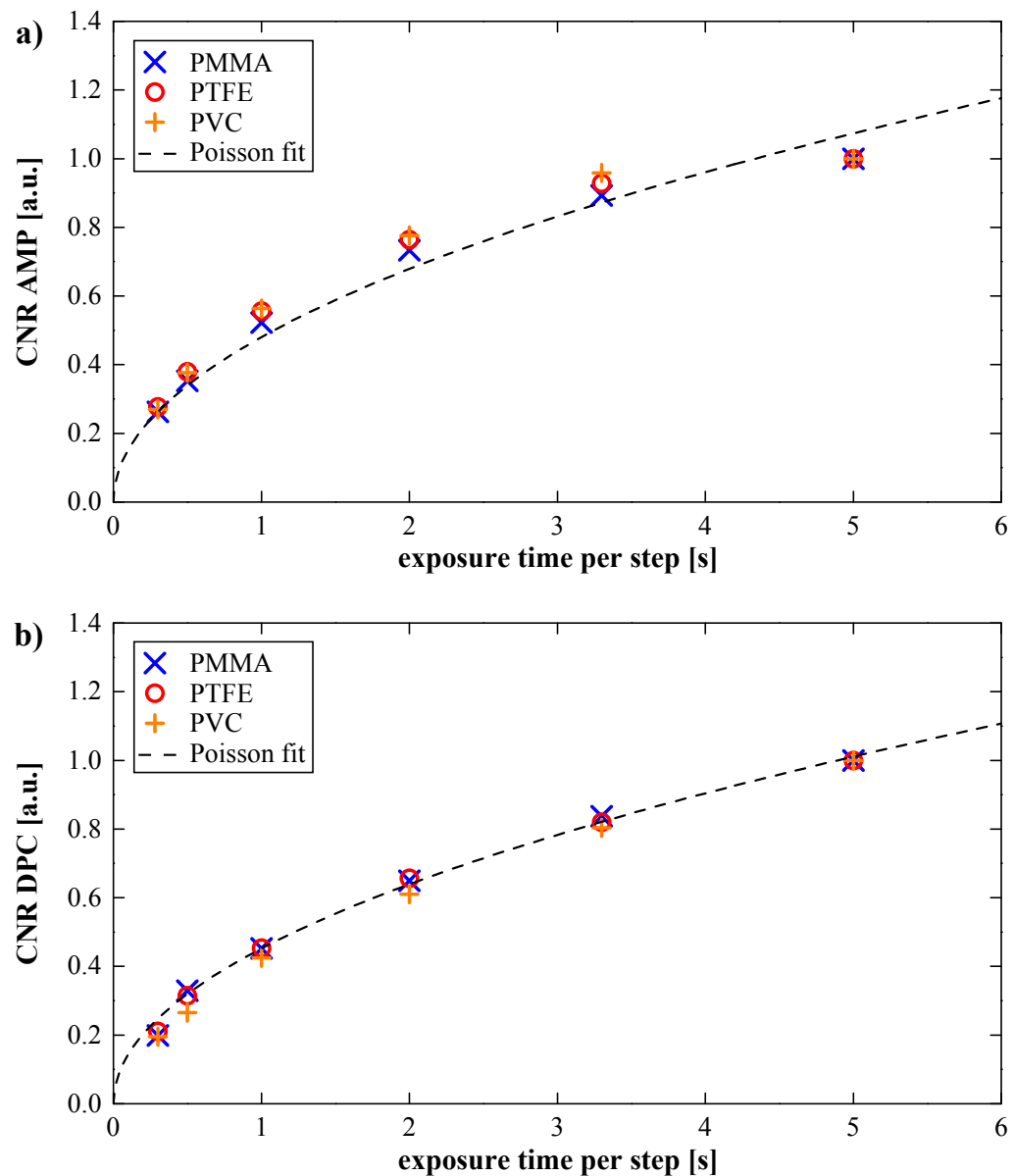


Figure 4.12: CNR vs. exposure time per phase step in projection mode at 45 kVp.

a) AMP CNR. **b)** DPC CNR. The projections were acquired with 10 phase steps. The dashed lines represent a square root function fitted to all data points of the respective plot. The displayed results are normalized relative to the maximum value of the respective rod.

for the respective contrast modality and rod are shown in Table 4.1 together with the standard deviations of the mean values.

The presented results clearly demonstrate that the acquisition mode with less steps and higher exposure time per step is generally beneficial over the acquisition mode with more steps. The presented standard deviations do not represent an error estimation of the obtained CNR values but the deviation from the mean value of the calculated ratios. They are given to express the fact that the degree of benefit for less steps and higher exposure per step depends on the total exposure of the respective projection. For lower total exposures (e.g. 45 kVp: 5 steps with 1 s vs. 10 steps with 0.5 s), the benefit is considerably larger than for higher total exposures (e.g. 42 kVp: 5 steps with 10 s vs. 10 steps with 5 s).

Number of projection angles in CT mode

To assess the impact of the number of projection angles on the CNR of the reconstructed CT slices, the CT data set acquired at 45 kVp with 2 s exposure for each of the 6 steps was reconstructed with varying fractions of the total number of acquired projections to simulate data sets acquired with different angular steps of gantry rotation and thus different total numbers of projection angles over the recorded interval of 360°. The plots in Figure 4.13 show that the CNR values for both contrast modalities behave roughly as expected in case that the CNR is proportional to the square root of the number of projection angles (dashed line), which is further explained in the discussion.

Number of phase steps in CT mode

In order to characterize the behavior of the CNR in dependence on the number of phase steps in tomography mode, CT data sets were acquired with varying number of steps. For all compared results shown in Figure 4.14, data sets of 1001 projections distributed over an interval of 360° were acquired at 45 kVp with 2 s exposure for each phase step and the CT slices of the respective contrast modality were reconstructed in the same way. Again a square root function (dashed lines) is fitted to all normalized data points of the corresponding figure to compare the results more easily to the theoretically expected behavior for mere statistical photon noise. The results demonstrate that both contrast modalities benefit from the increasing number of steps over the entire range of applied values. The benefit for the phase contrast CNR is considerably larger than for the attenuation contrast CNR, which is explained in the discussion.

Discussion

In this section, the presented results and their implications for practical imaging purposes are discussed. Since the respective results demonstrated here to characterize a particular exposure parameter were acquired at the same X-ray energy, the contrast in the applied contrast-to-noise ratios can be expected to be constant. Consequently, the discussion here is mainly restricted to the noise behavior.

The noise behavior of the attenuation and differential phase signal obtained from the phase

stepping routine in projection mode and the noise properties of the reconstructed attenuation and phase contrast slices have been investigated recently in several works [9, 10, 29, 40, 39]. Basically, the noise can be evaluated by applying Gaussian error propagation to the signal transmission chain of the respective signal. For a detailed derivation of the following formulas, the reader is referred to [9, 40]. Since a more detailed treatment of the noise behavior would go beyond the framework of this thesis, only a brief outline of the most essential findings is given and the formulas are simplified to be convenient for the practical discussion.

Given that the fluctuation around the mean value of photons hitting a detector pixel can be described by Poisson statistics and that the detector signal is proportional to the number of photons measured, the normalized standard deviation of the mean AMP signal \bar{S}_{AMP} and the absolute standard deviation of the DPC signal are given by

$$\frac{\sigma_{AMP, \text{statistics}}}{\bar{S}_{AMP}} = \frac{1}{\sqrt{M t F_0}}, \quad (4.12)$$

$$\sigma_{DPC, \text{statistics}} = \frac{1}{\sqrt{M t F_0}} \times \frac{\sqrt{2}}{V}, \quad (4.13)$$

where M is the number of phase steps, t the exposure time per step, and F_0 the mean number of photons hitting the respective pixel per second. At this point, it has to be mentioned that the absolute quantity of F_0 for a given acquisition setting of the scanner was not calculated in this work. The mean flux per pixel depends on a variety of factors such as the applied peak voltage and current of the X-ray tube, the efficiency of the detector, and the attenuation properties of the gratings and the sample. Consequently, the calculation is rather complicated and has to be done separately for each setting with different applied peak voltage and current. Therefore, the absolute values of the statistical photon noise could not be calculated in absolute values and the following discussion is generally of a qualitative nature.

The parameter V in Equation 4.13 describes the visibility and thereby the efficiency of the interferometer. In contrast, the statistical noise of the AMP signal is independent of the visibility, which is important for the following considerations. Considering the fact that the visibility of the scanner ranges from 10% at 48 kVp to 40% at 27 kVp, one can deduce from the equations above that the signal-to-noise ratio (SNR) for the AMP signal is generally higher than the SNR of the DPC signal (even for the maximum phase shift: $\pm\pi$).

Furthermore, at low photon statistics, the influence of statistical phase wrapping comes into play and the noise level of the DPC signal is higher than estimated by Equation 4.13 [29]. At even lower photon statistics, the phase signal gets lost and the standard deviation of the signal is constant [39].

Another contribution to the noise of the AMP and DPC signals is the influence from the jitter of the phase stepping due to mechanical uncertainties of the piezo translation stage [40]. Therefore, the actual grating position for a particular phase step is distributed around its ideal

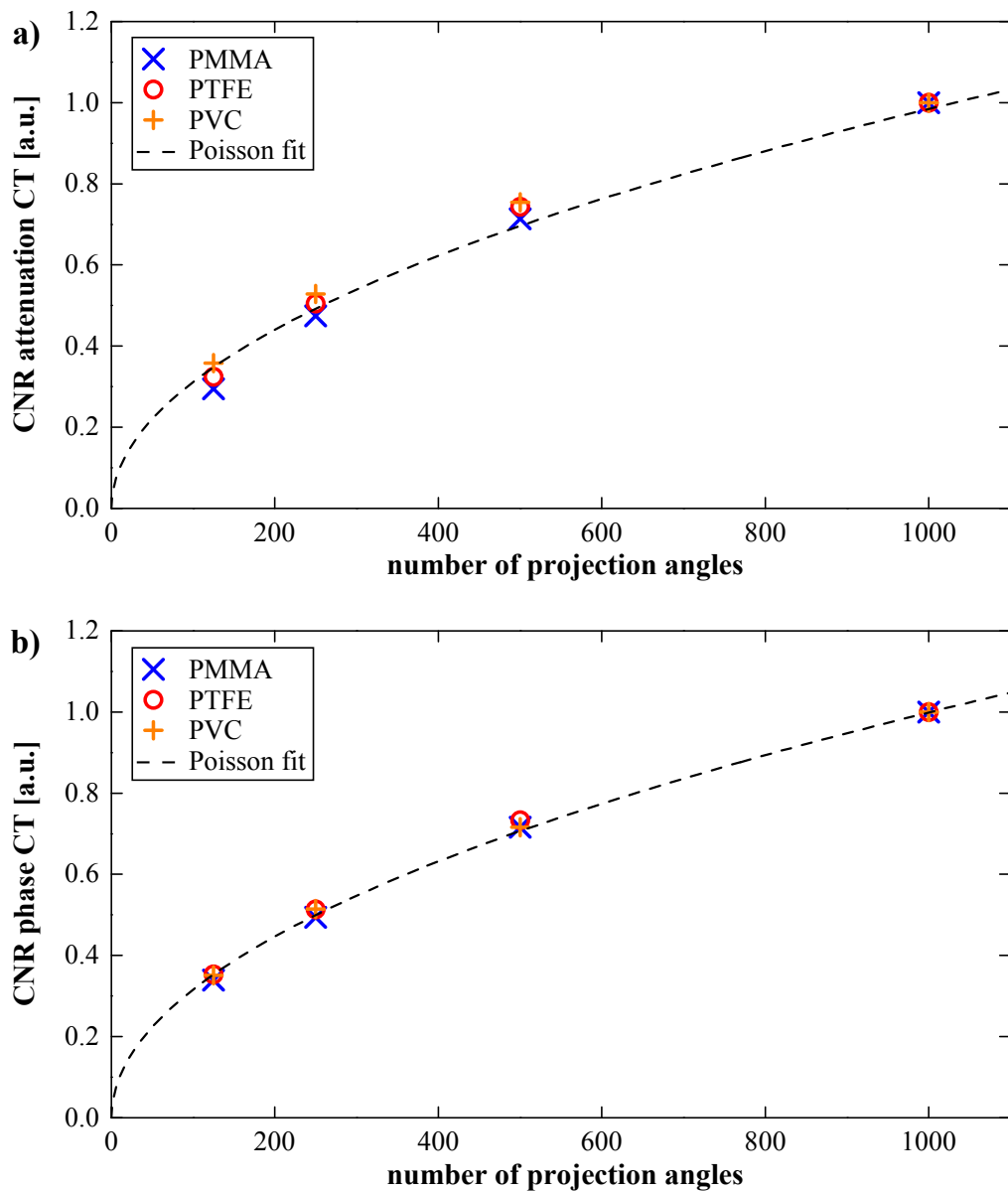


Figure 4.13: CNR vs. number of projection angles in CT mode.

a) Attenuation contrast CNR. b) Phase contrast CNR. The CT data set was acquired at 45 kVp with 1001 projection angles and 2 s exposure time for each of the 6 phase steps. The dashed lines represent a square root function fitted to all data points of the respective plot. The displayed results are normalized relative to the maximum value of the respective rod.

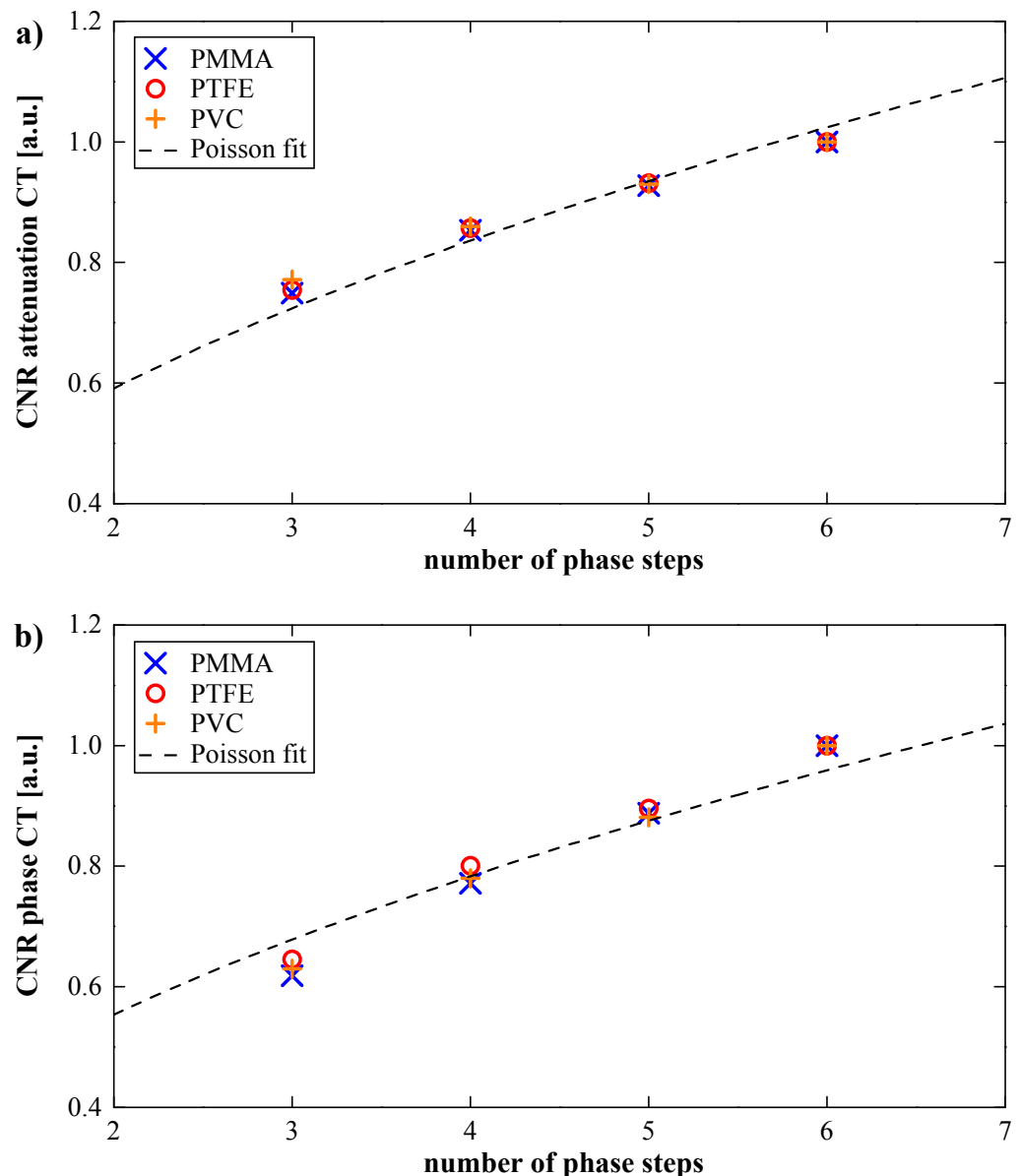


Figure 4.14: CNR vs. number of phase steps in CT mode.

a)) Attenuation contrast CNR. **b)**) Phase contrast CNR. The CT data sets were acquired at 45 kVp with 1001 projection angles and 2 s exposure time for each phase step. The dashed lines represent a square root function fitted to all data points of the respective plot. The displayed results are normalized relative to the maximum value of the respective rod.

position. Assuming the standard deviation of this distribution is given by σ_{pos} , simplified equations for the contribution from the jitter to the noise of the two signals can be formulated by

$$\frac{\sigma_{AMP,jitter}}{S_{AMP}} = \frac{2\pi V}{\sqrt{M}} \times \frac{\sigma_{pos}}{g_2}, \quad (4.14)$$

$$\sigma_{DPC,jitter} = \frac{\sqrt{3}}{\sqrt{M}} \times \frac{\sigma_{pos}}{g_2}, \quad (4.15)$$

where M is the number of phase steps and V the visibility of the interferometer.

Furthermore, contributions to the noise are caused by the detector. The readout noise produced by the readout and signal conversion electronics of the detector is independent of the exposure time and can be assumed to be constant for all presented measurements [18]. The dark current, which is caused by random generation of electron-hole pairs in the photosensitive area of the detector, increases proportional to the exposure time. A dark current correction was done separately for each projection acquisition, but due to fluctuations in temperature during the acquisitions a residual influence of the dark current on the noise cannot be excluded completely, but is expected to be small compared to the other noise distributions. Additionally, residual noise pattern from imperfections of the grating structures or their relative alignment to each other might also contribute to the noise in the images, as well as imperfections in the photosensitive area of the detector, such as defect pixels. The impact of the detector noise and imperfections of the setup on the noise of the different contrast modalities images are difficult to predict. For simplification, these sources are summed up to additional factors $\sigma_{AMP,detector}$ and $\sigma_{DPC,detector}$ for the estimation of the total noise of the respective signal:

$$\sigma_{AMP,total} = \sqrt{\sigma_{AMP,statistics} + \sigma_{AMP,jitter} + \sigma_{AMP,detector}}, \quad (4.16)$$

$$\sigma_{DPC,total} = \sqrt{\sigma_{DPC,statistics} + \sigma_{DPC,pw} + \sigma_{DPC,jitter} + \sigma_{DPC,detector}}, \quad (4.17)$$

where $\sigma_{DPC,pw}$ describes the contribution of statistical phase wrapping to the noise in the DPC signal. The quantitative contribution of each factor to the total noise for a particular acquisition setting is very complicated to determine and would go beyond the scope of this work.

The relation of the noise properties of the projection images to the noise properties of the resulting attenuation contrast and phase contrast CT data from the scanner is difficult to predict. On the one hand, it depends on the applied reconstruction filter, the number of projection images, and a resolution factor that describes the resolution in the reconstructed slices compared to the detector resolution [10]. On the other hand, instabilities of the gantry rotation system have to be considered, such as undesired mechanical movement of the gratings due to gravitational and mechanical influences caused by the rotation [52]. By applying Gaussian error propagation to the *Filtered Backprojection* algorithm with a *Hilbert* filter, it was found that the statistical noise level of the reconstructed phase images depends linearly on the statistical noise level of the projection images and is further inversely proportional to the square root of the number of projections angles [10]. Since the noise of different projections

is mutually independent, it can be expected that this is also true when considering additional contributions to the total noise in a projection image. Moreover, it is assumed that this is also approximately correct for the reconstruction of the attenuation data with a *Hamming* filter. Thus, the simplified proportionalities of the noise in the reconstructed slices to the noise in the projections are given by

$$\sigma_{attenuation, total} \propto \frac{1}{\sqrt{N_\theta}} \sigma_{AMP, total}, \quad (4.18)$$

$$\sigma_{phase, total} \propto \frac{1}{\sqrt{N_\theta}} \sigma_{DPC, total}, \quad (4.19)$$

where N_θ is the number of projection angles used for the reconstruction. Please note that this is only valid above a certain total number of projection angles, since for lower numbers of projections undersampling artifacts dominate the noise distribution in the reconstructed slices.

Above a threshold level of total exposure, the AMP signal does not benefit by further increasing of the exposure time per step (Fig. 4.11 a), Fig. 4.12 a)). The contrast is constant for all plotted values in each figure, since the images were obtained at the same X-ray energies. This indicates that the noise level must also be practically constant above a certain level, which is most likely due to the fact that the total noise in the AMP signal is dominated by the contribution from the jitter of the phase stepping for high total exposures ¹¹. This contribution is constant for the presented values, since the visibility of the setup and the number of phase steps were identical. The fact that the saturation effect starts at different exposure times for the depicted results at 36 and 45 kVp is due to the dependence of the statistical photon noise (Eq. 4.12) on the photon flux per pixel and thereby on the applied peak voltage, as explained in Section 4.3.3.

The results for the DPC signal clearly show that the photon noise is the dominant contribution to the total noise for high total exposures.

The found conclusions about the AMP and DPC CNR related to the exposure time per step are expected to be valid regardless of the number of steps, since the statistical noise as well as the jitter noise depend inversely proportional on the square root of the total number of phase steps. Consequently, the threshold level in the AMP signal depends practically only on the flux per pixel and the exposure time per step (for a constant visibility and position deviation in the phase stepping routine). However, for even higher total exposures or a higher visibility of the scanner, the noise of DPC signal is expected to behave similar to the AMP signal.

The fact that the DPC CNR values for very low exposure times are smaller than theoretically expected can be explained by the effect of statistical phase wrapping. This might

¹¹ A very rough approximation of the typical number of photons hitting a detector pixel was calculated. The standard deviation of the stepping position was assumed to be 250 nm, which is the typical resolution of the piezo, determined by a stability measurement of the piezo stage, conducted by Bart Pauwels from *Bruker microCT*. From this estimations, one finds that for the typical visibility range of the scanner, a fixed number of steps, and relatively high total exposure values, the contributions from the statistical photon noise to the total noise can be neglected compared to the contribution from the phase stepping jitter.

also explain the fact that the DPC CNR from each rod benefits to a different degree from increasing exposure time as demonstrated in Figure 4.11 a). For instance, PVC absorbs more radiation than PMMA and thus less photons hit the detector pixels. Therefore, the effect of statistical phase wrapping contributes more to the noise level of PVC than to the noise level of PMMA for the same total exposure time.

The results in Table 4.1 indicate that for a given total exposure time the images acquired with 5 steps and longer exposure times per step are beneficial over those acquired with 10 steps. The statistical noise is expected to be the same for both cases since the total exposure of the compared projections was identical. The contribution from the jitter is expected to decrease with increasing phase steps. Consequently, the explanation of the results has to be related to the contribution of the detector to the total noise in the resulting images. This seems reasonable, since the constant readout noise is applied to each raw image of the stepping procedure, regardless of the total number of phase steps. Hence, the relative impact of the detector noise on the total noise in the raw image is expected to increase, when the total exposure (flux per pixel and exposure time) of the raw image decreases. This assumption is confirmed by the fact that the degree of benefit for less steps and higher exposure per step in the presented results depends on the total exposure of the respective raw images. The fact that the DPC images seem to benefit even more from the setting with less steps may be explained by the fact that the detector noise in the raw images has stronger influence on the practical extraction of the DPC signal than on the AMP signal. Another explanation might be that the statistical phase wrapping effect in the DPC signal does not only depend on the total exposure of each pixel during the phase stepping, as theoretically expected, but also on the mean number of photons hitting the pixel in a single raw image.

For practical applications, this means that for a given total exposure per projection the quality of the raw image has a larger impact on the contrast-to-noise ratios of the resulting projections than the total number of phase steps. However, this statement has to be treated carefully. It is clearly valid for the comparison of 5 and 10 steps with the used total exposure parameters and is also expected to be valid for even higher number of steps. On the contrary, for 3 and 4 steps, the influence of the jitter of the phase stepping gets stronger and thus this statement might not be valid anymore.

The results in Figure 4.13 confirm that the noise of the CT slices for both contrast modalities is generally inversely proportional to the square root of the number of projection angles, as stated in Equation 4.18 and Equation 4.19. The fact that the degree of benefit from increasing the number of projection angles used to reconstruct the CT slices is higher for low total numbers of projection angles is due to the influence of undersampling artifacts, as mentioned before.

In Figure 4.14, the influence of the number of phase steps on the reconstructed slices in attenuation and phase contrast are depicted. The fact that the phase CNR benefits considerably more from increasing the number of phase steps than the attenuation CNR over the entire range of applied steps can be explained by statistical phase wrapping that only plays a

role for the phase signal ¹². As stated before, the impact of this effect becomes stronger the lower the total exposure of a single projection image. This can also explain that the phase CNR benefits even more at very low total number of phase steps.

The results of Figure 4.13 and Figure 4.14 can be easily compared, since all acquisition parameters, except for the varying numbers of projection angles and phase steps are identical. Moreover, the highest values used to normalize the other values stem from the very same measurement in both figures. From a comparison of the phase CNR behavior, one finds that the image quality of the CT slices benefits more by increasing the number of steps than by increasing the number of projections. The reason for this is statistical phase wrapping, which only depends on the total exposure of a single projection and not on the total number of projections [29]. Therefore, when reducing the total exposure for a CT acquisition, it is preferable to reduce the number of projection angles instead of the number of steps. However, this is only valid as long as the total number of projection angles is sufficiently high that undersampling artifacts from the reconstruction can be neglected. At this point, it should be mentioned again that all CT data were reconstructed by applying a FBP algorithm. For iterative reconstruction algorithms, the number of projections needed for reconstruction without undersampling artifacts can be expected to be considerably smaller. For in-vivo imaging, the acquisition time for CT data is so far limited to approximately 100 projection angles with typical exposure times per projection. This is due to the relatively low acquisition speed of the scanner and the fact that the animal can only be anesthetized for a certain period of time. Therefore, the CT data from in-vivo imaging with the scanner should be generally reconstructed iteratively in order to obtain the optimal image quality.

The overall conclusions for practical imaging applications with the scanner from the examination of the CNR behavior for different exposure parameters are:

- For projection images, the DPC CNR always benefits from increasing the total exposure regardless of the distribution of the total exposure among the different exposure parameters, while the AMP signal reaches a certain exposure level per step where it does not benefit from higher exposure.
- For typical numbers of phase steps (above 4) the total exposure for a projection image should be distributed among the smallest number of phase steps possible and thereby maximizing the exposure of the individual raw images, since this results in superior image quality for both contrast modalities.
- In CT mode, it is beneficial to apply a relative small number of projection angles instead of decreasing the total exposure for the individual projection images, as long as undersampling artifacts are avoided.

¹² The effect of statistical phase wrapping can be considered to be generally much higher for the individual projections of the CT data than for the analyzed radiographic data, since for the CT acquisition the Falcon tube was filled with water instead of air and thus the total attenuation of the sample was much higher. Therefore, the statistical phase wrapping shows already an impact on CT projections, while it does not on the analyzed single projection images with the same acquisition parameters.

4.3.3 CNR versus peak voltage

In this section, the influence of the peak voltage on the CNR of the two contrast modalities is investigated. A given peak voltage of the X-ray tube results in a spectrum of X-rays with a certain effective mean energy. In theory, it is more convenient to compare the CNR to the respective different mean energies for the acquisitions. However, in practice, the current of the source is always set to the maximum value that is possible for a certain applied peak voltage in order to maximize the photon flux and thereby reducing the statistical noise regardless of the applied exposure times or numbers of steps (see Equ. 4.12, 4.13). Thus, for practical considerations, it seems more convenient to compare the CNR to the applied peak voltage, since this parameter is connected with a certain effective mean energy for the X-rays and the corresponding photon flux created by the source. Consequently, for the CNR dependence on the peak voltage, two general effects have to be considered for the presented results. On the one hand, the contrast between the respective rod and the reference material depends on the spectrum of the X-rays. On the other hand, the noise in the images depends on the applied photon flux and the visibility of the interferometer, which are both related to the applied peak voltage.

Contrast versus peak voltage in projection mode

In Figure 4.15, the fit parameter for each rod representing the contrast in the projection images is demonstrated for the two signals. The presented values are obtained from the acquisitions with the highest possible exposure times, without reaching the saturation level of the detector at the respective peak voltage. The applied exposure times for each of the 10 phase steps were 10 s for peak voltages up to 39 kVp and 5 s at 45 kVp and 48 kVp. This was due to the fact that an exposure time of 10 s per step at high peak voltages led to the saturation of the detector and since only certain exposure time values can be applied with the used acquisition software, the next lower possible exposure time was 5 s. The relative errors of the contrast parameters are less than $\pm 1\%$ for all demonstrated AMP results in this section, whereas the relative errors of the DPC results are decreasing with increasing total exposure. The relative errors of PMMA range from $\pm 7\%$ at 27 kVp to $\pm 4\%$ at 42 kVp. For 45 and 48 kVp the error is roughly $\pm 5\%$. Correspondingly, the relative errors for PTFE range from $\pm 5\%$ to $\pm 3\%$ and for PVC from $\pm 33\%$ to $\pm 9\%$.

Maximum CNR versus peak voltage in projection mode

In Figure 4.16, the absolute CNR values of the different rods corresponding to the contrast values presented in Figure 4.15 are displayed, therefore the acquisition parameters are the same as in the last paragraph. Moreover, the same error estimations are valid since the errors of the noise can be neglected compared to the errors of the contrast fit parameters. The depicted results represent the maximal CNRs that could be realized for each applied peak voltage.

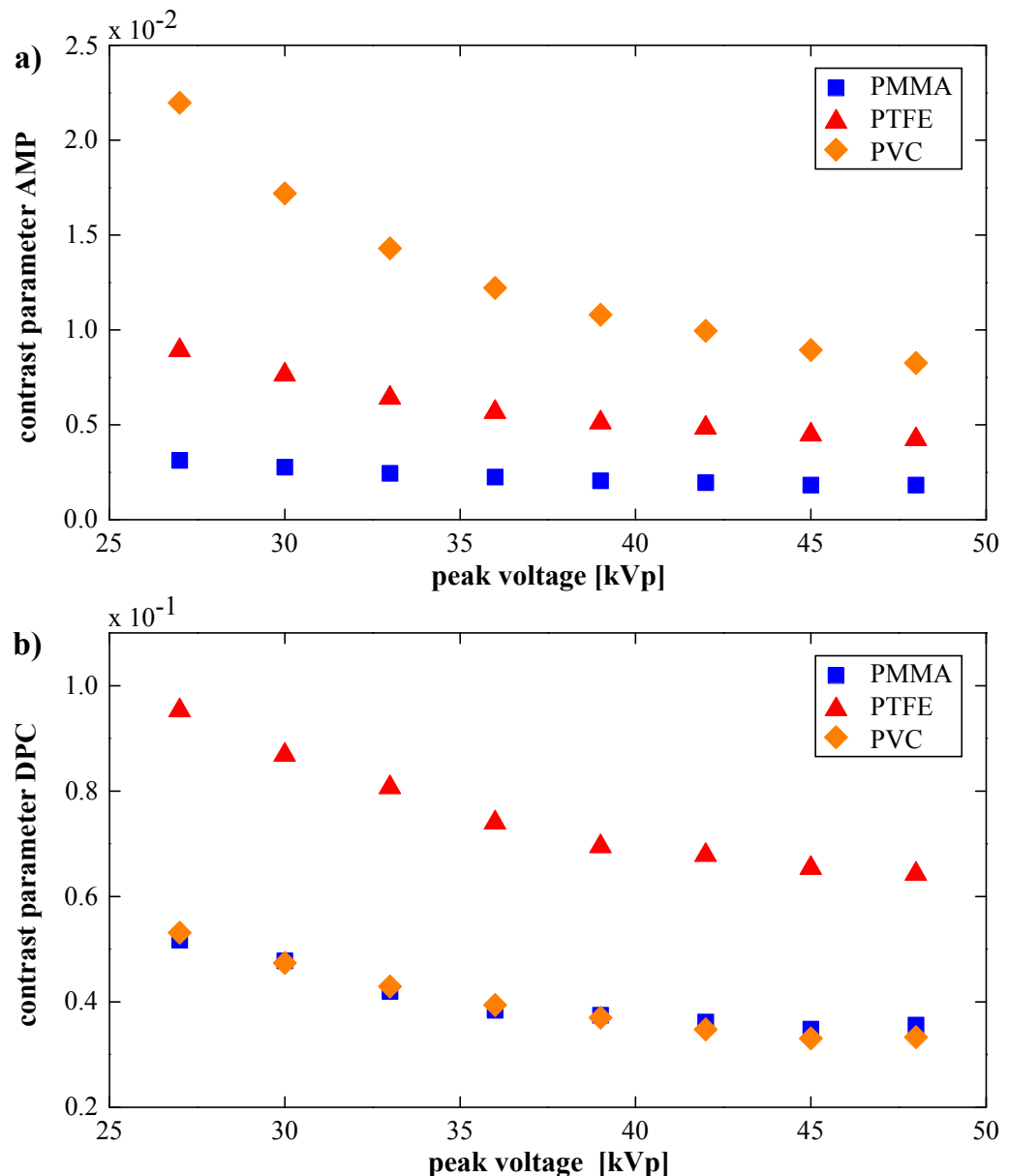


Figure 4.15: Contrast parameter from projection analysis vs. peak voltage.

a) AMP CNR. **b)** DPC CNR. All presented results are absolute values and were obtained from projections acquired with 10 phase steps. The exposure time per step was 5 s for the acquisition at 45 kVp and 48 kVp, and 10 s for all other acquisitions.

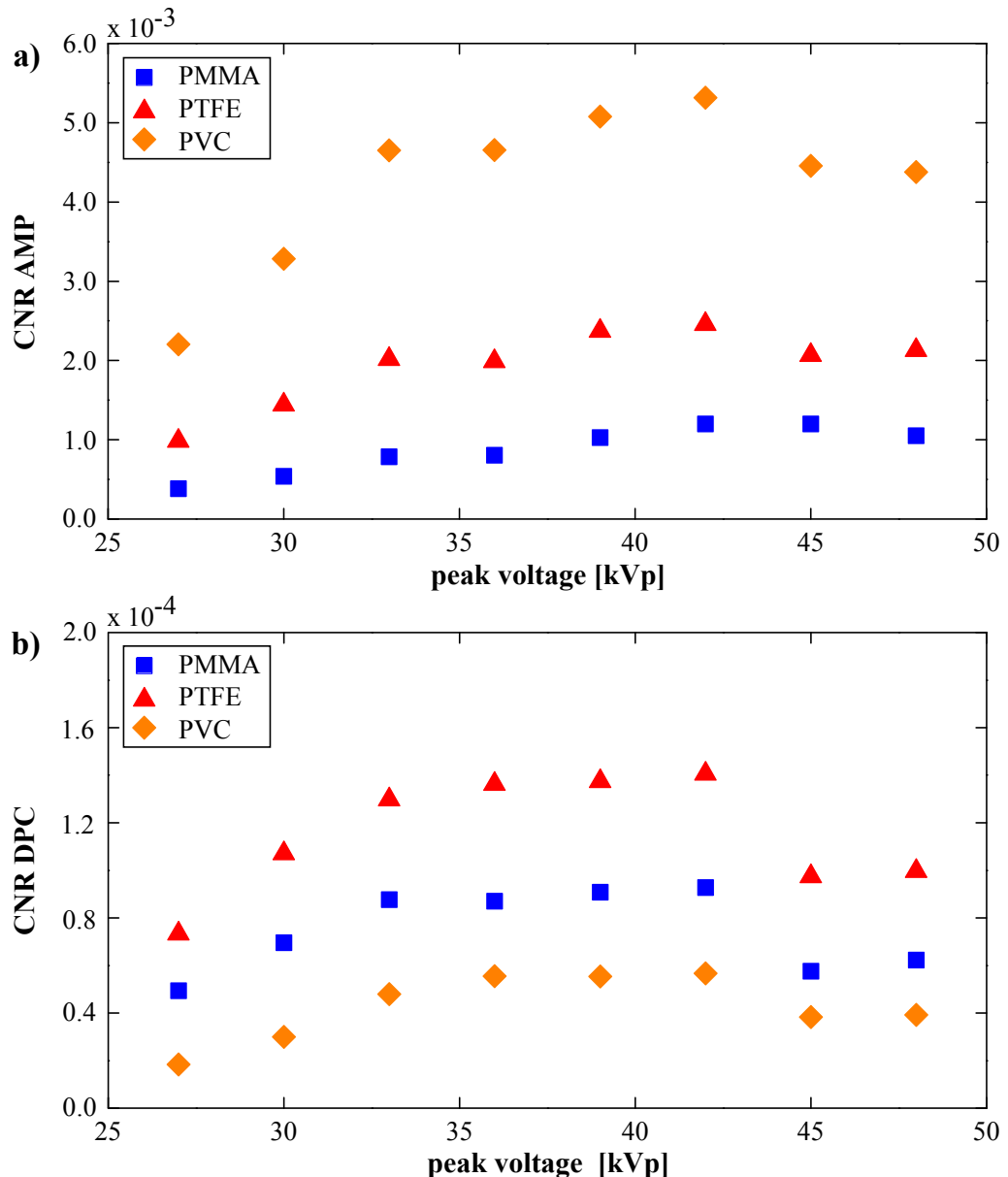


Figure 4.16: Maximal CNR vs. peak voltage in projection mode.

a) AMP CNR. b) DPC CNR. All presented results are absolute values and were obtained from projections acquired with 10 phase steps. The exposure time per step was 5 s for the acquisition at 45 kVp and 48 kVp, and 10 s for all other acquisitions.

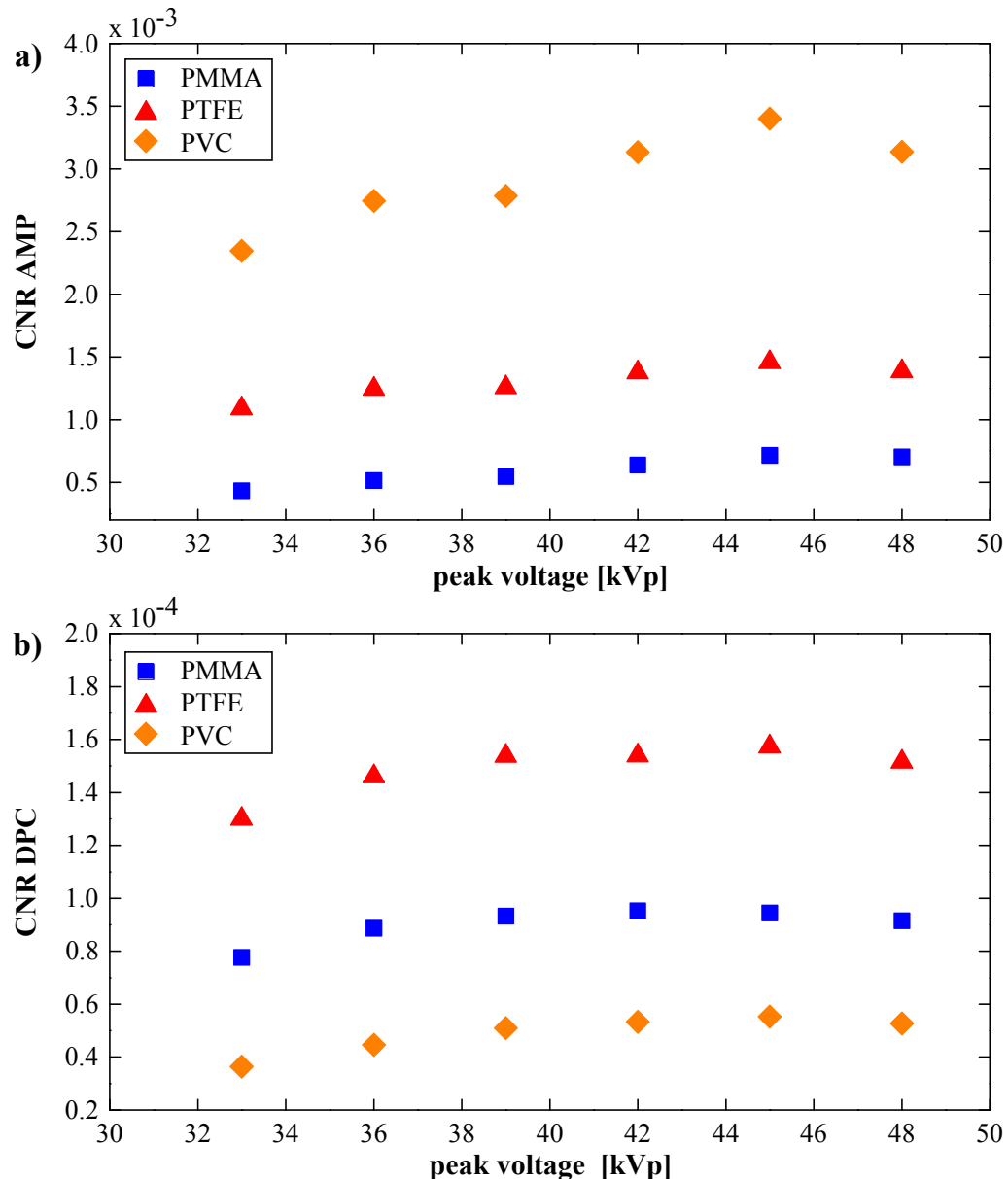


Figure 4.17: CNR vs. peak voltage at constant exposure time in projection mode.

a) AMP CNR. **b)** DPC CNR. All presented results are absolute values and were obtained from projections acquired with 3.3 s for each of the 10 phase steps. Please note that the presented results in this figure are acquired with the new G₂ grating.

CNR versus peak voltage at constant total exposure time in projection mode

In Figure 4.17, the absolute CNR for the different rods in relation to the peak voltage for constant exposure times is depicted. The images were obtained with 3.3 s for each of the 10 phase steps. Please note that the presented results are acquired with the new G₂ that provided a higher visibility over the entire range of applied peak values. The relative errors of the DPC results are decreasing with increasing peak voltage. The relative errors of the DPC CNR for PMMA range from $\pm 5\%$ at 33 kVp to $\pm 4\%$ at 48 kVp. Respectively, the relative errors for PTFE range from $\pm 3\%$ to $\pm 2\%$ and for PVC from $\pm 16\%$ to $\pm 10\%$.

CNR versus peak voltage at constant total exposure in CT mode

In Figure 4.18, the absolute CNR for the different rods in CT mode are shown in relation to the peak voltage at comparable total exposures for the respective CT acquisitions. As already mentioned, it is rather complicated to calculate the exact photon flux for a given peak voltage. Therefore, comparable settings in terms of total exposure were determined by considering the transmission profiles in the acquisition software for the individual raw images of the phase stepping. For all presented CT acquisitions, the number of phase steps (and the gain factor) was constant and the exposure time per step was adapted to the respective peak voltage in such a way that the average transmission values were as equal as possible. However, the accuracy of this procedure was limited by the fact that the exposure time per step in the scanner can only be varied in discrete steps. Therefore, the estimated total exposures of the presented results still showed appreciable differences. For instance, the average transmission signal of the CT acquisition at 32 kVp and 10 s exposure per step showed a relative deviation from the mean value of the average transmission signal of about +2%. Correspondingly, the deviations of the other acquisitions are: +17% at 35 kVp and 10 s, -20% at 39 kVp and 3.3 s, and +7% at 45 kVp and 2 s. All data sets were acquired with 6 phase steps. Please note that the CT acquisition at 33 kVp was the lowest applicable peak voltage for the maximal exposure time of 10 s per step, at which no underexposure of the detector images occurred and thus a correct extraction of the signals for all pixels was feasible.

Discussion

Figure 4.15 is primarily shown to simplify the discussion of the following CNR results. The contrast for both imaging modalities can be assumed to be independent of the noise and thus the same values are expected for other exposure times or numbers of steps¹³.

Aside from that, the presented results can be used to estimate the feasibility of the applied projection analysis. Theoretically, the linear attenuation coefficient μ and the decrement of the real part of the refractive index δ (phase coefficient) of the respective rod can be calculated from the fit parameters, as explained in Section 4.2.1. In practice, a quantitative evaluation of the attenuation and phase coefficients from the presented results is rather complex and would go beyond the framework of this work, therefore only a brief qualitative comparison of the

¹³ The loss of the phase signal due to statistical phase wrapping at very low exposure times can be ignored for the applied total exposures.

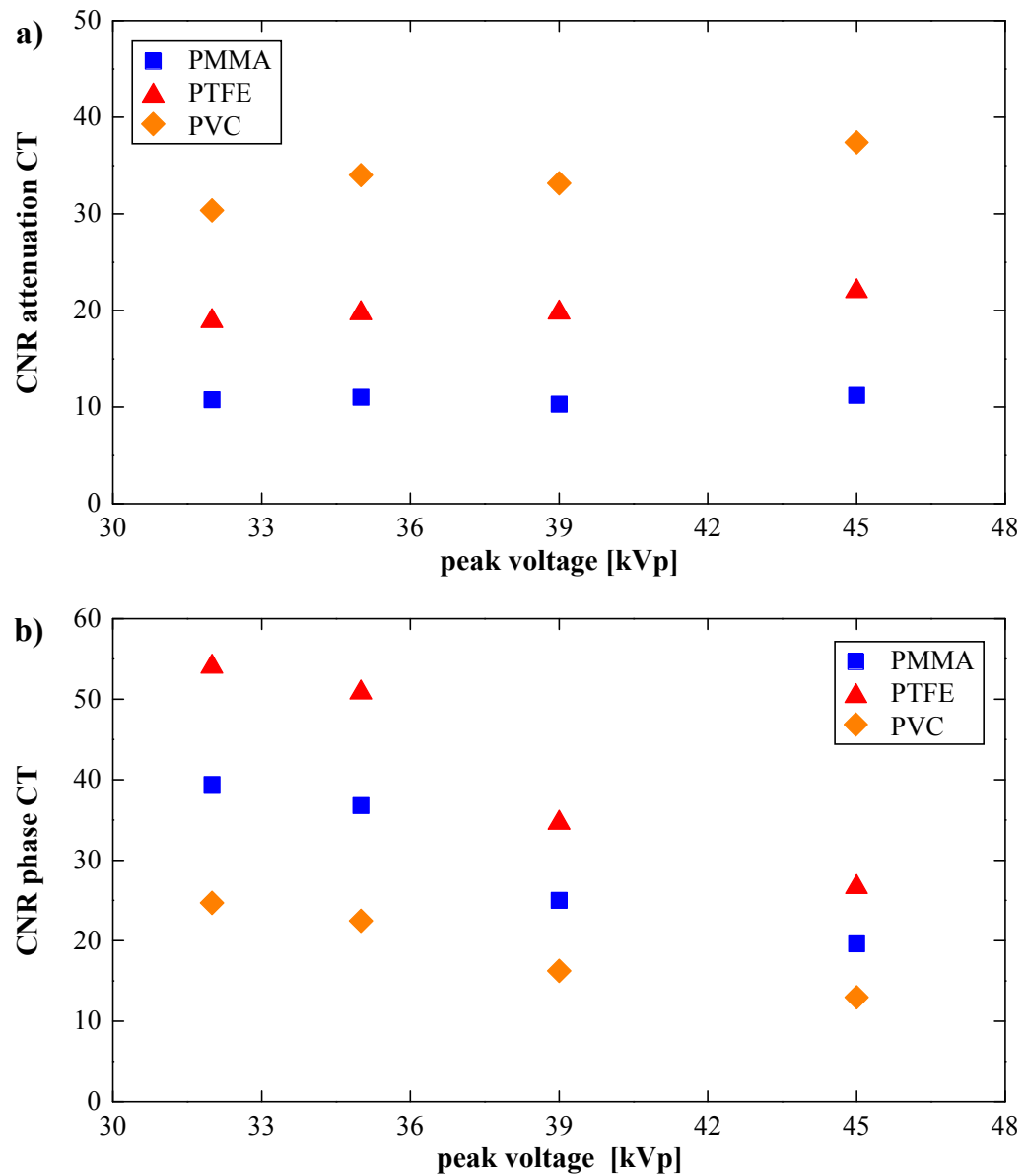


Figure 4.18: CNR vs. peak voltage at constant total exposure in CT mode.
a) Attenuation CNR. **b)** Phase CNR. All presented results are absolute values and 6 phase steps were used for each acquisition. The applied exposure times per step are 10 s for 32 kVp and 35 kVp, 3.3 s at 39 kVp, and 2 s at 45 kVp.

contrast parameters to the literature values is presented here. The energy dependence of μ and δ for the rod materials in the relevant energy range are shown in Section A.3.

A rough approximation of the mean photon energies corresponding to the applied range of peak voltages for both signals was calculated based on the findings of [52]. The values of the fit parameters were subsequently compared to the reference data from literature at the corresponding energies. By first examining the results of each rod separately, one finds that the overall behavior of both fit parameters to a change in peak voltage is in decent agreement with the corresponding reference data for all rods and over the entire range of applied peak voltages. Furthermore, by considering the relations between the contrast values of the different rods, it can be stated that the ratio of the PMMA fit parameter to the PTFE fit parameter is roughly the same as the ratio of the corresponding reference data for both contrast modalities and the entire range of applied peak values. In contrast, the ratios of PMMA to PVC and PTFE to PVC are significantly larger as expected from the reference data, which at first sight indicates that the contrast values resulting from the fit of the PVC rod are underestimated. However, the overall behavior of the contrast for each rod in projection mode is in good agreement with the behavior of the contrast in CT mode; moreover, the ratios found for the CT contrast values of the different rods are very similar to determined ratios for the projection analysis. This indicates that the reason for the strong deviation of the PVC contrast values from the reference data is not related to the applied fitting procedure. It may rather be related to the strong beam hardening effect of the PVC rod, since no correction for the beam hardening is applied, neither in the projection nor in the CT analysis.

In summary, it can be stated that the line-by-line analysis applied to the projection images provides reliable results in both contrast modalities and is feasible to compare the contrast-to-noise ratios in the recorded images of the phantom .

For a quantitative discussion of the presented CNRs in relation to the applied peak voltage, a variety of different effects and dependencies has to be considered. Here, only the most important effects are explained and the results are discussed qualitatively. The following considerations can be expected to be valid for projection and CT imaging mode.

As explained before, the attenuation and phase contrast introduced by a particular rod depends on the effective mean energy of the polychromatic spectrum of the X-ray tube and thus on the applied peak voltage, as shown in Figure 4.15.

The effect of beam hardening that typically leads to an underestimation of the contrast in both signals [8] is depending on the material properties and geometry of the sample and on the effective energy of the X-ray photons. For the applied range of peak voltages, the beam hardening effect for all rods is expected to decrease for increasing peak voltage in both contrast modalities.

As mentioned before, the current of the X-ray tube was maximized for each peak voltage and thereby the photon flux is also depending on the applied peak voltage. The relative statistical noise of the AMP signal decreases with increasing photon flux (Eq. 4.12) and is therefore expected to decrease for increasing peak voltages. The statistical noise of the phase signal (Eq. 4.12) is inversely proportional to the photon flux and the visibility of the interferometer. Since the photon flux increases and the visibility decreases for increasing peak

voltages (see Tab. 3.1), these effects are canceling out each other to some extent and consequently the behavior of the statistical noise of the phase signal in relation to the peak voltage is difficult to predict.

The relative noise introduced to the attenuation signal by the jitter of the phase stepping gets smaller for lower visibilities of the scanner (Eq. 4.16) and thus decreases for increasing peak voltages, while the noise from the jitter in the phase signal (Eq. 4.15) is independent of the visibility and is expected to be constant for varying peak voltages.

The detector noise is assumed to be approximately constant for different applied peak voltages and therefore it is expected to influence the CNR behavior only for the case of very low total photon numbers per step (see Sec. 4.3.2).

Additionally, for both signals, the effect of beam hardening might partially be interpreted as additional noise by the used analysis methods for projections and CT data.

In Figure 4.16, the maximal realizable CNRs for each peak voltage are shown. For both contrast modalities, the CNR rises considerably at relatively low applied peak voltages. This can be explained by the fact that the improvement of the noise and the less pronounced beam hardening effect for increasing peak voltages in this range dominate the effect of decreasing contrast for both signals and all rods. For the AMP signal, this statement is also generally valid for the interval from approximately 33 to 42 kVp, but the impact of the improving noise and beam hardening is relatively smaller compared to the decreasing contrast. On the contrary, the DPC signal is roughly constant in the same interval. This indicates that the additional dependence of the statistical noise on the visibility of the scanner results in the fact that the various effects are canceling out each other for this range of peak voltages. The drop in the CNR behavior of both contrasts at 42 kVp is due to the lower applied exposures per step at 42 and 45 kVp. This was done due to practical reasons related to the sample, as explained before. However, by reducing the gain parameter to a smaller factor than the applied 20%, the maximal exposure time of 10 s might also be applied at very high voltages. Therefore, the behavior of the maximum CNR in relation to relatively high peak voltages for typical imaging purposes with the scanner can be assumed to be more similar to the behavior of the curves in Figure 4.17.

In these plots, the CNR is shown for increasing peak voltage and a constant exposure time of 3.3 s for each of the 10 phase steps. From the discussions about the CNR in dependence on the different exposure parameters (Sec. 4.3.2), one can deduce that the overall behavior of the CNR of the DPC signal in relation to the peak voltage is expected to be roughly the same for different number of steps and exposure times that are typically applied for practical imaging purposes¹⁴. For the attenuation signal this is not true due to the saturation of the noise level when the jitter noise is the dominating noise contribution and has to be considered individually for each acquisition setting.

For practical applications, this means that for a given total acquisition time the applied peak voltage should be in the approximate range from 35 to 45 kVp, since this interval pro-

¹⁴ This statement is restricted: It is only valid above a certain mean numbers of photons per pixel, when the influence of statistical phase wrapping can be ignored, and above a certain total exposure per step, when the influence of the detector can be neglected. Further information is given in Section 4.3.2.

vides the highest CNR for both contrast modalities. The best image quality regardless of the applied dose can be achieved at approximately 45 kVp. At even higher voltages, the CNR for both contrast modalities is expected to decrease with increasing peak voltage, as indicated by the results at 48 kVp in Figure 4.17.

Please note that the results in Figure 4.16 and Figure 4.17 originate from images that were acquired with different G₂ gratings. The new G₂ used for the results in Figure 4.17 had higher gold structures and therefore provided a higher absolute visibility over the entire range of applied peak voltages. The comparison of the absolute CNR values of both plots can be used to illustrate the influence of the visibility on the different contrast modalities. The AMP CNR values in Figure 4.16 up to 42 kVp are generally significantly higher than the corresponding values in Figure 4.17. The main reason for this is naturally the higher exposure times, but the fact that the jitter noise in the AMP signal gets larger the higher the visibility of the scanner is also contributes to the lower absolute values. In contrast, the DPC values in both figures are very similar for a given peak voltage, due to the fact that the loss of photon flux is compensated by the higher visibility.

The results in Figure 4.18 show the relation of the CNR to the peak voltage for a given total exposure of a CT data set. The presented behavior of the attenuation CNR may be explained by the following considerations. The attenuation coefficients of the materials that theoretically describe the contrast introduced by the respective rod are decreasing for increasing peak voltages. Aside from that, a higher voltage leads to a decrease of the cupping effect that is considered to cause a strong underestimation of the CNR with the applied analysis of the CT slices. Moreover, the noise distribution from the jitter of the phase stepping decreases with increasing voltage. Since different effects are partially compensating each other, the results for the attenuation CNR are slightly increasing.

The phase coefficients of all rods also decrease monotonically over the entire range of applied peak voltages, while the beam hardening also decreases. However, the quantitative effect of beam hardening in the phase signal is less pronounced than in the attenuation signal [8] and therefore has a smaller impact on the presented results. Furthermore, the statistical noise of the phase signal increases with rising peak voltages, due to the dependence on the visibility. Consequently, the effect of less beam hardening is dominated by the other effects and the phase CNR is expected to diminish for increasing voltages, as shown in Figure 4.18.

This means that for comparable total exposures the ideal applied peak voltage depends on the contrast modality that has priority in the particular measurement. Nevertheless, it is recommended for typical applications to choose a relatively low peak voltage, since the relative loss in CNR for the attenuation contrast compared to a higher voltage is much smaller than the relative gain for the phase contrast, which usually is the preferred contrast modality.

For in-vivo imaging and particularly in the CT mode of the scanner, the applied dose to the small animal, typically a mouse, during image acquisition plays an important role. To estimate the applied dose for the presented CT measurements, one has to consider that the dose applied per second depends on the applied peak voltage and the resulting photon flux. In Table 4.2, the approximate mean dose rates applied to a mouse in the scanner are displayed for the different peak voltages and the corresponding maximal currents of the X-ray tube. The

dose rates were measured with a patient skin dosimeter (Unfors PSD, Unfors Instruments AB, Billdal, Sweden) placed in the center of a polymer cylinder with a diameter of 3 cm. The polymer material resembles carbon in density and thus the cylinder can be expected to be a suitable phantom for the estimation of the mean mouse dose. To avoid statistical errors the dosimeter was placed in the beam for 10 minutes and the dose rate was calculated subsequently from the obtained dose values. The dose per acquired raw image was then calculated by multiplying the dose rate with the applied exposure time per step for each of the four acquisitions with different peak voltages. The presented results in Table 4.2 indicate

Peak voltage [kVp]	Dose rate [mGy/s]	Dose per acquired raw image [mGy]
32	0.030	0.301
35	0.051	0.523
39	0.091	0.301
45	0.175	0.339

Table 4.2: Typical mouse dose rates and total doses per phase step for the image acquisition with the scanner at varying peak voltages.

that the dose per acquired raw image is comparable for the entire range of applied peak voltages. For exactly equivalent total exposures at different peak voltages, the dose is expected to increase slightly with increasing peak voltages. The deviation from this behavior for the acquisitions at 35 kVp and 39 kVp is related to the varying total exposure of the presented results, as mentioned before. Therefore, for in-vivo imaging, it is highly recommended to use the lowest applicable peak voltage without causing underexposure of the raw images, since this results in the best image quality and the lowest dose for comparable total exposures.

Since the number of projection angles and the reconstruction was the same for all compared data sets, the results and conclusions here can be directly transferred to a single projection image.

In summary, the results from the CNR behavior in relation to the applied peak voltage lead to the following conclusions for practical imaging purposes:

- For a given total acquisition time per projection, the phase and attenuation CNR are significantly increasing up to approximately 35 kVp. For a peak voltage range from 35 to 45 kVp the resulting image quality in both contrast modalities is relatively similar. Above 45 kVp the phase and attenuation CNRs decrease again.
- The best image quality regardless of the applied dose can be achieved at approximately 45 kVp.
- For a given dose per acquisition, the applied peak voltage should be as low as possible without causing underexposure of the raw images.

4.3.4 CNR versus binning

Results

In this section, the contrast-to-noise ratios for different binning modes were compared. For this purpose, the raw data of a series of projection images, covering a wide range of different acquisition parameters, were subsequently binned by summing up the values of neighboring 2×2 or 4×4 pixels in the raw images, thereby enlarging the effective pixel size of the processed images. The particular binning factors were selected due to the fact that the acquisition software of the scanner provides a 2×2 and a 4×4 binning mode. Since the implemented binning mode is also based on the summation of the pixel values after the detector readout, the results presented here can be assumed to reflect the expected results for images acquired in 2×2 or 4×4 binning mode of the acquisition software.

The binned images were analyzed in the same way as the unbinned projections and the ratios of the CNR from the respective binning mode to the CNR of the unbinned images with the same acquisition settings were calculated. The mean values of these ratios were calculated for each rod and contrast modality and are given in Table 4.3. The acquisition parameters used for the presented results are given in Section A.1.7.

Contrast modality	Material	2×2 binning/unbinned	4×4 binning/unbinned
AMP	PMMA	1.18 ± 0.05	1.40 ± 0.20
	PTFE	1.18 ± 0.06	1.41 ± 0.24
	PVC	1.19 ± 0.08	1.43 ± 0.25
DPC	PMMA	1.22 ± 0.05	1.67 ± 0.11
	PTFE	1.24 ± 0.06	1.66 ± 0.18
	PVC	1.32 ± 0.07	1.86 ± 0.14

Table 4.3: Comparison of CNR for different binning modes.

The presented standard deviations do not represent an error estimation of the obtained CNR values but the deviation from the mean value of the calculated ratios. They are given to express the fact that the degree of benefit for binned image acquisition depends on the total exposure of the respective projection. For low total exposure values the gained benefit due to image binning was significantly larger than for higher total exposures.

Discussion

In the 2×2 binning mode, the statistical noise (Eq.4.12, Eq.4.13) of both contrast modalities is reduced by half since the number of photons hitting each detector pixel is 4 times higher than for the respective unbinned acquisition. Correspondingly, the statistical noise in the 4×4 binning mode is reduced by 75%. Since the contrast parameters are not affected by the binning, the contrast-to-noise ratios for both contrast modalities are expected to increase with increasing bin factor, which is in good agreement with the presented results. The fact that the gained benefit due to image binning is higher for low total exposure values in both contrast

modalities can be explained by the higher impact of the detector noise. Furthermore, the statistical phase wrapping effect at low photon statistics is reduced by the binning procedure. The generally larger benefit from binned acquisition for the DPC signal can be explained by the reduced phase wrapping and the fact that the statistical noise is the dominating factor in the DPC noise over the entire range of applied total exposures, whereas the AMP noise is dominated by the jitter noise at high photon statistics.

For practical imaging purposes, this means that the image quality in terms of contrast-to-noise ratio can be significantly improved by binning of the raw images. On the other side, it has to be considered that the resolution in the images might be decreased by the binning procedure. This is investigated further in Section 5.3.5.

4.3.5 CNR versus delay parameters

Piezo delay parameters

The G_0 grating is moved during the phase stepping routine by using a piezoelectric actuator (PEA) [36] to allow positioning of the grating with sub-micron precision. The creep of the PEA (a time-dependent change in displacement without any accompanying change in the control voltage [35]) and additional instabilities introduced by the assembly of the grating cause a loss in precision of the grating position. To compensate for these effects certain delay times are implemented in the phase stepping routine. After the movement of the grating to each stepping position (except the first stepping position), the piezo delay time is applied prior to image acquisition to ensure the correct position of the grating for each phase step. To compensate for the higher piezo instability at the first stepping position due to a longer travel distance of the PEA, the piezo start delay time is applied before acquiring the raw image at the first position of the phase stepping routine.

To investigate the influence of these delay parameters, projections with different values for the delay parameters were acquired at 42 kVp with an exposure time of 1 s for each of the 5 phase steps. Please note that the used images for this analysis were obtained with *Version 3* of the acquisition software and the new G_2 grating.

The relative errors of the DPC results are approximately $\pm 11\%$ (PMMA), $\pm 7\%$ (PTFE), and $\pm 33\%$ (PVC), and can be considered to be constant for the contrast-to-noise ratios of both piezo delay parameter measurements.

In Figure 4.19, the results for different applied piezo delay times are displayed. The CNR of both contrast modalities is constant for delay times ranging from 1000 ms to 200 ms. For 100 ms the CNR is drastically reduced and the processed images show severe artifacts such as strongly pronounced Moiré fringes. Thus, the creep of the piezo and other instabilities do not influence measurements with delay times of 200 ms or more.

From the results in Figure 4.20, it can be deduced that the CNR of both contrast modalities is practically independent of the piezo start delay parameter for the entire range of applied values.

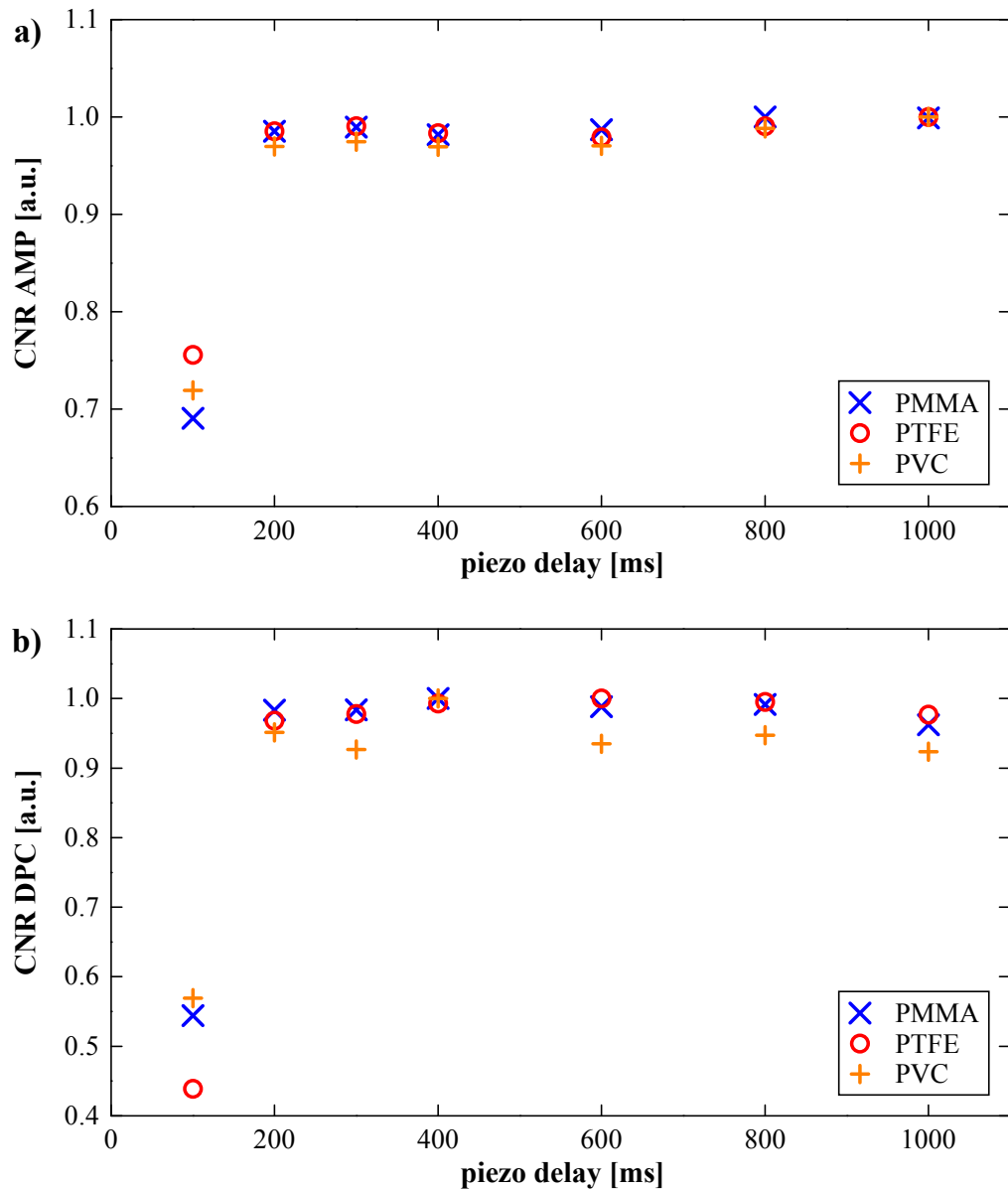


Figure 4.19: CNR vs. piezo delay in projection mode.

a) AMP CNR. b) DPC CNR. The projections were acquired at 42 kVp with an exposure time of 1 s for each of the 5 phase steps. The displayed results are normalized relative to the maximum value of the respective rod.

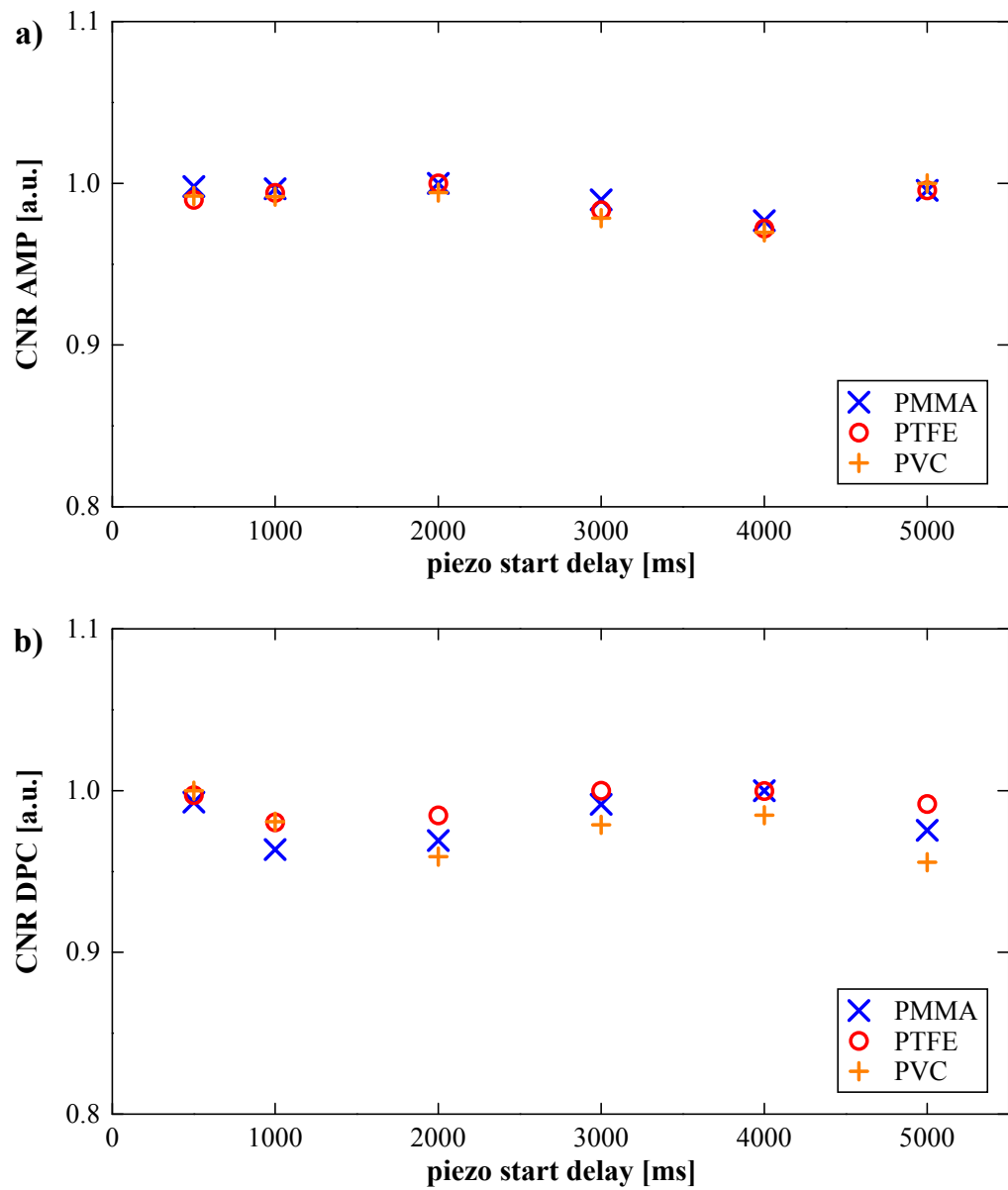


Figure 4.20: CNR vs. piezo start delay in projection mode.
a) AMP CNR. **b)** DPC CNR. The projections were acquired at 42 kVp with an exposure time of 1 s for each of the 5 phase steps. The displayed results are normalized relative to the maximum value of the respective rod.

Gantry delay parameter

For CT imaging, an additional delay factor is implemented in the acquisition software. The gantry delay parameter is applied after each movement of the gantry and prior to the acquisition routine for each projection to compensate for mechanical instabilities caused by the rotation process, such as vibrations of the gratings. To assess the impact of this parameter on the image quality of reconstructed slices, CT data sets with different gantry delay times were acquired at 45 kVp and 2 s exposure for each of the 6 phase steps. The results of the calculated CNR for the different gantry delay times are shown in Table 4.4. As mentioned

Contrast modality	Material	Gantry delay	Gantry delay	Gantry delay
		100 ms	500 ms	1000 ms
Attenuation CT	PMMA	11.32	11.21	11.20
	PTFE	22.10	21.78	22.00
	PVC	37.16	36.42	37.38
Phase CT	PMMA	18.81	18.71	19.62
	PTFE	26.04	25.58	26.66
	PVC	12.63	12.50	12.99

Table 4.4: Contrast-to-noise ratios for varying gantry delay times.

before, the error of the CT CNR results are marginal and can be neglected here. The results indicate that the image quality of the reconstructed slices in both contrast modalities is not affected by a reduction of the gantry delay time from 1000 ms to 100 ms. This was confirmed by a qualitative comparison of the images to ensure that the reduced gantry delay time does not cause any kind of artifacts that do not contribute to the CNR analysis, such as shading or blurring at the edges of the rods.

Discussion

The results presented in this section demonstrate that the piezo delay time can be reduced from the default value of 1000 ms to 200 ms without affecting the image quality. Consequently, the total acquisition time per phase step can be reduced by 800 ms regardless of the applied exposure time.

Furthermore, the piezo start delay time can be reduced from 5000 ms to 500 ms without compromising the image quality, which leads to a reduction of 9000 ms¹⁵ for each phase stepping routine regardless of the exposure time and number of steps.

In practice, this means a substantial gain in acquisition speed: For a typical projection acquisition (including the flat-field acquisition) with 5 phase steps and 2 s exposure per step, the total acquisition time of approximately 65 s can be reduced to roughly 40 s without any

¹⁵ This indicates that the piezo start delay parameter is implemented twice in one acquisition cycle. This could be a programming mistake.

SECTION 4.3: RESULTS AND DISCUSSION

loss in image quality ¹⁶.

Moreover, for CT imaging the acquisition time per projection can be shortened further by reducing the gantry delay parameter from the default value of 1000 ms to 100 ms.

Considering the presented results, it is highly recommended to reduce the delay parameters for future imaging purposes with the scanner, in particular for in-vivo measurements, for which the acquisition speed of the scanner plays a crucial role.

¹⁶ The total acquisition time was measured by hand starting from the moment when the acquisition is started in the software until the sample is restored to its starting position. Please note that *Version 3* of the acquisition software was used for the evaluation of the total acquisition time.

4.4 Summary

In this section, the results from the CNR analyses and the conclusions for practical imaging purposes are summarized.

First of all, it can be stated that the applied analysis of the projection images provided reliable results to compare the image quality of both contrast modalities for different acquisition settings.

The gain parameter has basically no influence on the resulting image quality in both contrast modalities and can thus be selected arbitrarily for each image acquisition. This is naturally only valid when the applied gain factor does not result in an over- or underexposure of the respective raw images. Please note that the typical values of the gain factor used in this work (20% - 100%) are based on the old acquisition software. In the new acquisition software the gain factor is defined in a different way and the feasible values are much lower (typically the applied factor should be below 8).

The procedure of maximizing the current of the X-ray tube for an applied peak voltage is generally recommended for all imaging purposes with the scanner, since it results in an improvement of image quality independent of the acquisition time.

The best image quality regardless of total acquisition time and dose is achieved at a peak voltage of approximately 45 kVp and naturally with the highest number of phase steps and exposure times per phase steps that are possible without overexposure of the raw images. For CT images, the number of projections should also be maximized.

For a given total acquisition time, but without considering the applied dose, the peak voltage should still be around 45 kVp. The total exposure time per projection should be distributed among 5 phase steps and the exposure time per phase step should be maximized. Moreover, for CT imaging, the total acquisition time per projection should be given priority over the number of projection angles, as long as the total number of projection angles is high enough that undersampling artifacts can be neglected for the applied reconstruction procedure.

For the case of in-vivo imaging, when the applied dose to the animal is of great importance, the applied peak voltage should be as low as possible without causing underexposure of the raw images, since this results in a superior image quality compared to acquisitions at higher peak voltages and a comparable dose per acquisition.

The contrast-to-noise ratios for both contrast modalities increase with increasing bin factor, whereas the resolution of the processed images is expected to decrease. Therefore, the application of the binning procedure depends on the particular requirements of the individual imaging acquisition. The influence of the binning on the resolution of the images is investigated further in Section 5.3.5.

The different delay parameters investigated in this work can all be reduced considerably, which leads to a substantial gain in acquisition speed of the scanner.

5 Characterization of the spatial system response

5.1 Direct modulation transfer function measurements

5.1.1 Data acquisition

The modulation transfer function (MTF) of a linear optical system can be obtained by measuring the contrast in an image of a periodic test object, ideally consisting of a sinusoidal pattern. To measure directly the full MTF of the imaging system the contrast must be determined for intensity distributions ranging from the lowest to the highest spatial frequency of the system. Traditionally, this luminance patterns are created by illuminating a target with absorbing bars of altering spatial frequency [7, 55].

Since the setup discussed here is not a typical laboratory setup with an optical table and a sample holder that is finely adjustable in all directions, but instead consists of a rotating gantry and a positioning stage that can only be moved parallel to the gantry axis, it is very difficult and cumbersome to position an additional target or optical device precisely in the field of view of the scanner. For this reason, the test pattern in the presented experiment was realized by intrinsic features of the setup.

Moiré fringes that represent a nearly sinusoidal intensity distribution can be produced by the superposition of square-wave patterns of relatively high spatial frequencies; in this experiment, the Moiré fringes were created by the superposition of the periodic intensity distribution created by the G_1 grating and the pattern of the G_2 grating. More information about Moiré interferometry with a grating interferometer can be found in [21, 54].

Due to imperfections in the grating structures and slight deviations in the alignment of the gratings, the overall intensity distribution of the background in the FOV of the scanner is not perfectly constant but always shows some residual Moiré fringes. For normal imaging purposes, these fringes are causing problems in the image processing and are minimized by fine adjustment of the relative alignment of the gratings to each other.

In this experiment, the possibility to rotate, shift, and tilt the G_1 grating relative to the G_2 grating was used to produce strongly pronounced Moiré fringes and to position them in such a way that they represented a nearly sinusoidal intensity pattern. By changing the distance between G_1 and G_2 , the spatial frequency of the pattern was tuned. The lowest spatial frequency for which a feasible sinusoidal intensity distribution could be realized was 0.006 line pairs per pixel (lp/pixel). It was impossible to produce fringes with lower frequencies that still had a constant frequency and were aligned parallel to each other on the detector, regardless of the chosen region of interest.

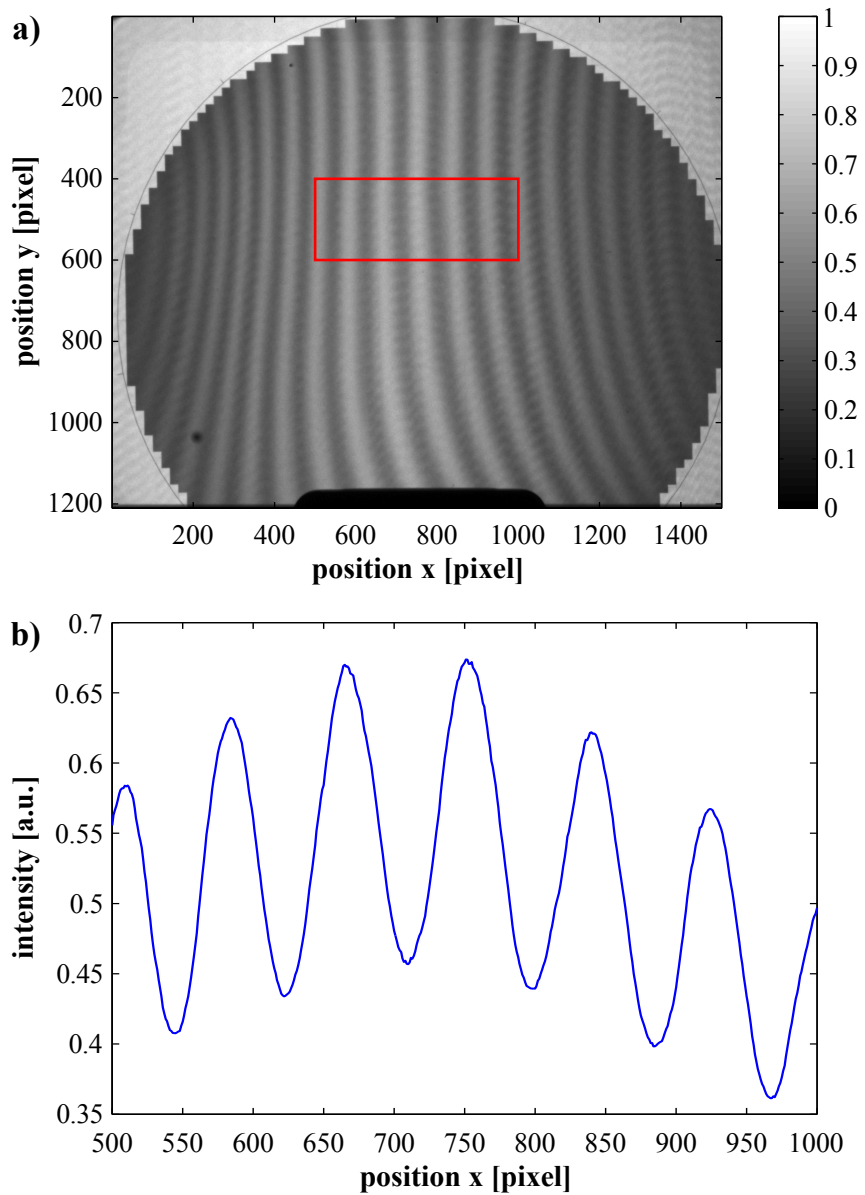


Figure 5.1: Moiré pattern and corresponding line profile. **a)** Raw image of Moiré pattern with spatial frequency of 0.012 lp/pixel . The selected region of interest is indicated by the red rectangle. **b)** One-dimensional periodic profile function, obtained by averaging the 200 rows along the vertical axis of the region of interest.

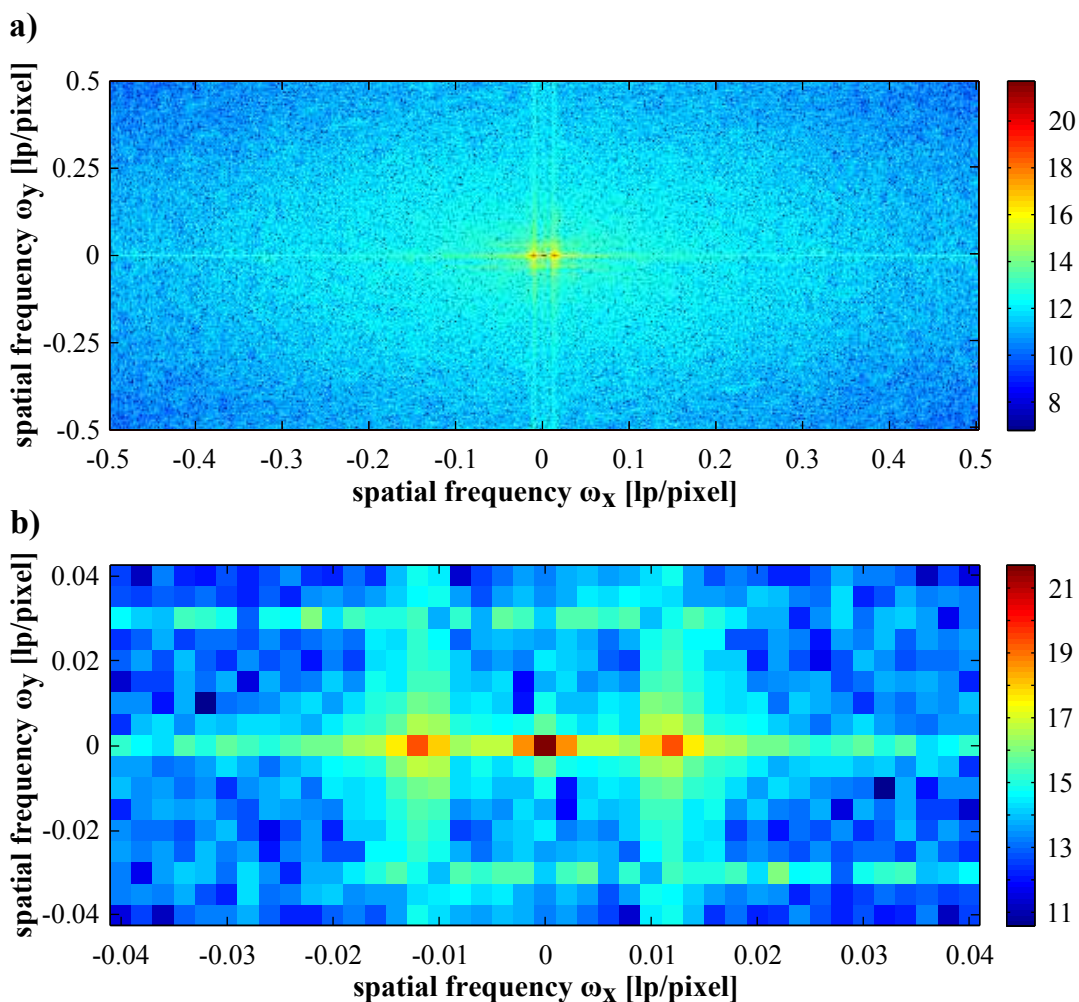


Figure 5.2: Fourier representation of Moiré pattern. **a)** Two-dimensional Fourier spectrum in logarithmic scale calculated from the region of interest, indicated by the red rectangle in Figure 5.1. **b)** Magnified central region of the logarithmically scaled Fourier spectrum including the center peak and the peaks of the frequency distribution at the positive and negative spatial frequencies of the regarding Moiré pattern.

Another contribution to this limitation was the fact that, ignoring the Moiré fringes, the distribution of background intensity in the FOV was still anisotropic. The shadowing effect, due to the cone beam and the height of the bars of the used analyzer grating G₂ (45 μm), caused the background intensity to be relatively higher in the central region of the field of view compared to the right and left margins, which influenced the measured contrast for low spatial frequencies. Hence, a region of interest with a size of 500×200 pixels in the central region of the raw image was selected (indicated by the red rectangle in Figure 5.1 a)) and by rotation of G₁ the fringes were aligned as parallel as possible to the vertical axes of the detector within this region. The highest spatial frequency that could be technically realized with our setup was 0.314 lp/pixel, as the G₁ grating could not be shifted further away from the G₂ grating.

Two series of about 30 images ranging from the lowest to the highest realizable spatial frequency were recorded at 45 kVp with 1 s exposure time per image and 35 kVp with 3 s exposure time per image. The spatial frequency steps between the different images were not exactly equidistant, since changing the distance between G₁ and G₂ in equidistant steps did not result in equidistant frequency steps. All images were acquired the new G₂ grating and *Version 3* of the acquisition software.

For each image, the spatial frequency spectrum was determined by calculating the absolute of the two-dimensional *Fast Fourier Transform (FFT)* of the region of interest, as depicted in Figure 5.2. The distance between the zeroth component of the frequency spectrum, which is referred to as the center peak, and the nth component where the spectrum had a local maximum (frequency peak), was used to calculate the spatial frequency of the respective pattern. This method of finding the spatial frequency of the pattern takes into account that the spatial frequency pattern might consist of a linear combination of frequency components in x- and y-direction, due to the imperfections in the alignment of the fringes. Practically, the y-component of the frequency was negligibly small for all images, but the exact position of the peak was still important for the calculation of the contrast with the Fourier methods, explained in the following.

The contrast of a sinusoidal pattern can be generally described by the intensity maximum I_{max} and the intensity minimum I_{min} of the sinusoidal distribution:

$$contrast = \frac{I_{max} - I_{min}}{I_{max} + I_{min}}. \quad (5.1)$$

The extreme values of the measured Moiré pattern were assessed with three different methods, which are explained in the following paragraphs.

Standard method

The first method, which is referred to as the Standard method in this thesis, is based on the one-dimensional periodic profile of the region of interest, obtained by averaging over the 200 rows along the vertical axis of the region of interest, as shown in Figure 5.1. The maximum

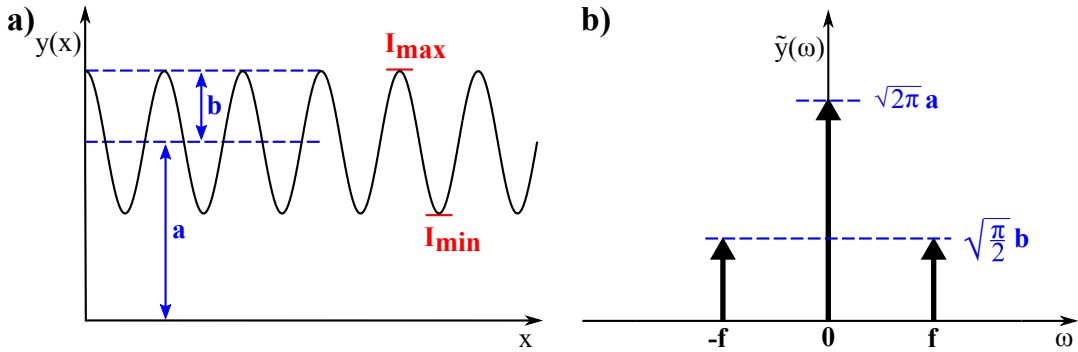


Figure 5.3: Sketch to illustrate the relationship of a sinusoidal pattern and the corresponding frequency spectrum. **a)** Sinusoidal pattern represented by a cosine function. The amplitude b and the offset a of the function $y(x)$ are indicated by the blue arrows, whereas the intensity maximum I_{\max} and minimum I_{\min} are marked by the red lines. **b)** Corresponding Fourier spectrum $\tilde{y}(\omega)$. The Dirac delta functions are indicated by bold black arrows, f is the spatial frequency of the cosine function.

and minimum of one period of the profile were determined for five fringes distributed over the entire width of the ROI to compensate for the uneven distribution of the background intensity in the scanner and thus have a statistically more reliable value for the contrast.

Since the fringes were not always parallel to each other neither to the vertical axis of the region of interest, the process of averaging might underestimate the calculated contrast. As the pattern for a single line was too strongly influenced by noise and the uneven background, a different way to assess the contrast by Fourier analysis was used.

Fourier method

To explain the relation between the contrast in real space and the components of the Fourier transform, a simple example is considered, as sketched in Figure 5.3. A sinusoidal pattern can be described in one dimension by

$$y(x) = a + b \cos fx, \quad (5.2)$$

where a is the average intensity or offset, b is the amplitude of the periodic function, and f the spatial frequency of the pattern. The Fourier transform of $y(x)$ is given by

$$\tilde{y}(\omega) = \sqrt{2\pi} a \delta(\omega) + \sqrt{\frac{\pi}{2}} b \delta(\omega - f) + \sqrt{\frac{\pi}{2}} b \delta(\omega + f). \quad (5.3)$$

Since $\tilde{y}(\omega)$ is a sum of three Dirac delta functions, the frequency spectrum has only three non-zero components:

$$\tilde{y}(\omega = 0) = \sqrt{2\pi} a, \quad (5.4)$$

$$\tilde{y}(\omega = \pm f) = \sqrt{\frac{\pi}{2}} b. \quad (5.5)$$

From Equations 5.4 and 5.5, it can be seen that the magnitude of the zeroth component of the Fourier spectrum is related to the offset of the periodic function, while the magnitude of the first component is related to the amplitude. Thus, the contrast definition can be reformulated to

$$\text{contrast} = \frac{I_{\max} - I_{\min}}{I_{\max} + I_{\min}} = \frac{2 b}{(a - b) + (a + b)} = \frac{2 \tilde{y}(f)}{\tilde{y}(0)}. \quad (5.6)$$

To transfer the results from the example to the recorded Moiré pattern, one has to consider that the analyzed region of interest is represented by a finite two-dimensional array of discrete values and that a *Fast Fourier Transform (FFT)* algorithm is used to calculate the *finite Fourier Transform*¹ of the ROI. For discrete calculations of the Fourier transform, the sampling frequency plays an important role, but since the sampling frequency for the analyzed pattern is always higher or equal to the Nyquist frequency, aliasing effects can be neglected here. Hence, the calculated Fourier spectrum consists of discrete values up to the Nyquist frequency of 0.5 lp/pixel with a spacing of 0.005 lp/pixel in the vertical and 0.002 lp/pixel in the horizontal direction and therefore the infinitively narrow peaks of the Dirac delta functions in the analytical example, are represented by two-dimensional peaks with a finite width in the discrete spectrum.

Consequently, the definition of contrast in Equation 5.6 is not exactly correct for the analysis of the presented intensity pattern, but the contrast is still related to the amplitude ratio of the frequency peak to the center peak. As in the example above, the spectrum can be assumed to be symmetric around the origin, hence it is sufficient to analyze the frequency peak at positive spatial frequencies of the two-dimensional Fourier spectrum and double the magnitude of the positive frequency peak for further calculations. Therefore, the straightforward method to assess the contrast of the Moiré fringes by Fourier analysis is to calculate the ratio of twice the maximum value of the frequency peak in the positive spectrum to the maximum value of the center peak. This method is named Fourier method in further discussions.

Fourier sum method

Considering the fact that frequency components of the spectrum that are very close to the maximum component also contribute to the contrast in the pattern, yet another analysis method was applied. This time, the values of the adjacent pixels to the respective peaks in the discrete Fourier spectrum were also taken into account. A threshold was set to 0.1% of the maximum value of the regarding peak and all values above the threshold were summed up. In this case, the contrast was subsequently calculated by substituting the single values in the Fourier method by the calculated sums. This method is referred to as Fourier sum method in the following.

¹ The denomination from the textbook by Kak and Slaney [46] is used here. Accordingly, the *finite Fourier Transform*, which is also sometimes abbreviated by *FFT*, calculates the discrete frequency domain representation of a discrete function in real space, whereas the *Discrete Fourier Transform (DFT)*, calculates the continuous frequency domain representation of a discrete function in real space.

5.1.2 Data processing

As mentioned before the "sampling process" used here to obtain the data was not equidistant. To overcome problems in the following calculation of the Fourier Transform, the measured data were fitted with a polynomial function of 8th degree and resampled in equidistant steps from 0 to the highest measured frequency with a sampling frequency above the Nyquist frequency. The particular form of the fit function was selected since it represented the data very well and particularly provided a relatively realistic result for very low frequencies ².

The correct form to calculate a line spread function (LSF) is to deduce it from a normalized symmetric MTF. Thus, the points from the fitted MTF are mirrored along the vertical axis and normalized to $\text{MTF}(0, 0) = 1$. The LSF is subsequently calculated from the normalized symmetric MTF using an *inverse Fast Fourier Transform (iFFT)* algorithm. The absolute of the result is calculated to convert all values to real numbers. In order to get an analytical function of the LSF, the resulting points were then fitted to a linear combination of two Gaussian functions, since the linear combination reflected better the relatively long tails of the LSF compared to a single Gaussian. Finally, the line spread functions were normalized to unity area. A sketch of the data processing is shown in Figure 5.4.

To explain the particular shape of the resulting LSF, one may possibly argue, that the narrow Gaussian originates from the broadening of the signal by the conversion mechanism from X-ray photons to visible light in the GOS scintillator, which is discussed more detailed in [25]. The broader Gaussian may be associated with multiple scattering processes of the visible light photons in the scintillator, due to the amorphous grain structure of the GOS crystal [19].

² A Gaussian function, typically used to describe modulation transfer functions, did not represent the data sufficiently, whereas polynomial functions of lower degree provided naturally a smoother curve than the polynomial function of 8th degree, but reflected less the typical saturation effect of the MTF for very low frequencies.

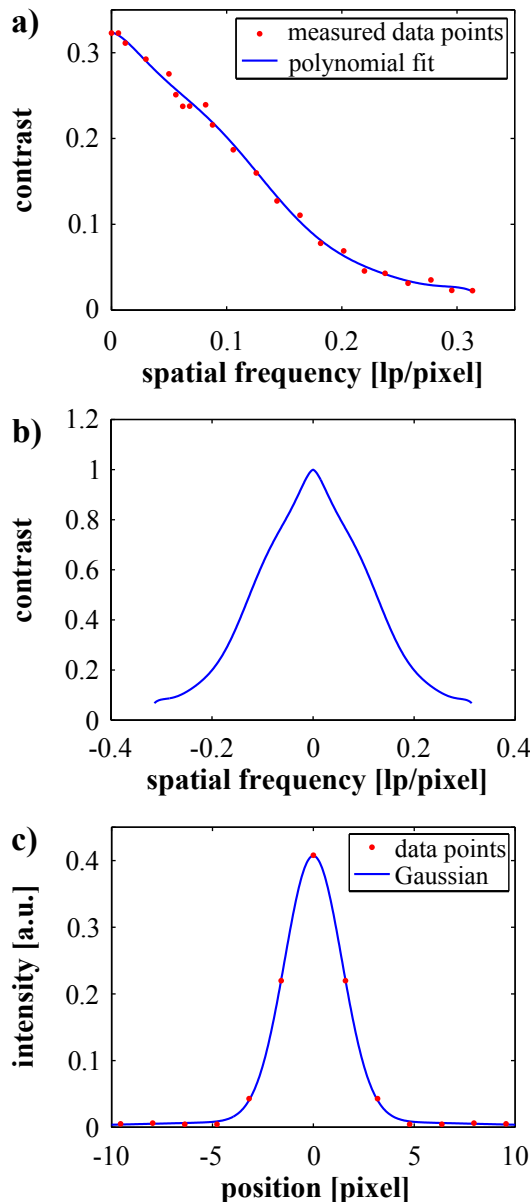


Figure 5.4: Scheme of data processing for the direct MTF measurements. **a)** Measured modulation transfer function and polynomial fit function. **b)** Normalized symmetric MTF obtained by mirroring and normalizing the resampled points from the polynomial fit function. **c)** Line spread function, found by calculating the absolute of the inverse Fast Fourier Transform of the normalized symmetric MTF. The red dots show the calculated data points; the fit function, indicated by the blue curve, has the shape of a linear combination of two Gaussian functions.

5.2 Edge profile measurements

5.2.1 Data acquisition

Besides direct methods to measure the modulation transfer function, it can also be evaluated by analyzing images of a single edge or slit. This kind of measurements are commonly referred to as indirect methods, since instead of the MTF, the line spread function or edge spread function (ESF) of the objects are measured, and the MTF is calculated from the measured data. The standard method to conduct an edge profile measurement is to bring a knife edge, also called a half plane (object with a sharp edge), in an exactly known position into the field of view of the imaging system; in simplest case, the edge is aligned parallel to the pixel rows of the detector. In this section, the edge profile measurements conducted with different objects in various planes relative to the detector are introduced. All presented experiments were carried out at a peak voltage of 45 kVp with 1 s exposure time per image. Furthermore, all images were acquired with the new G₂ grating and *Version 3* of the acquisition software.

Edge of G₂ grating in the detector plane

As mentioned above, precise positioning of an object in the scanner is very difficult and only possible in the object plane, thus alternative options were checked. Since the effective size of the G₂ grating is smaller than the active area of detector, the border of the grating structures with the surrounding wafer can be seen in raw images of the field of view (Fig 5.5 a)). Due to the design of the grating, consisting of many rectangular blocks assembled to a "circular" grating, the border between the grating and the surrounding region has the shape of a staircase. As the gratings are produced with very high precision, the edges of the borders may be assumed to be perfectly parallel or perpendicular to each other, within the limits of accuracy of the measurement. Due to the absorbing gold structures (gold height = 45 μm) in the grating region, these borders also provide enough bright-to-dark contrast to use them as a knife edge for edge profile measurements. Since the G₂ grating is positioned immediately in front of the detector, the magnification factor (1.7) from the cone beam geometry can be neglected and therefore the plane where the experiment took place is called the detector plane throughout this thesis.

The edge spread function is often determined by averaging the intensity along the edge axis over many detector rows to reduce the noise in the resulting profile. However, in the presented case, the grating was slightly rotated to the axis of the detector, which is indicated by the red line in the left image of Figure 5.5. Consequently, the ESF from the edges of the grating might be falsified by this procedure. To avoid this issue, individual lines were analyzed, for which the influence of the angular deviation was negligible. The measured values of the ESF were then normalized to 0 and 1. Subsequently, a linear combination of two error functions was fitted to the data points of each line, since the error function is an antiderivative of the Gaussian function. The assumption that the resulting LSF has the shape of two Gaussian functions has already been explained in Section 5.1.2.

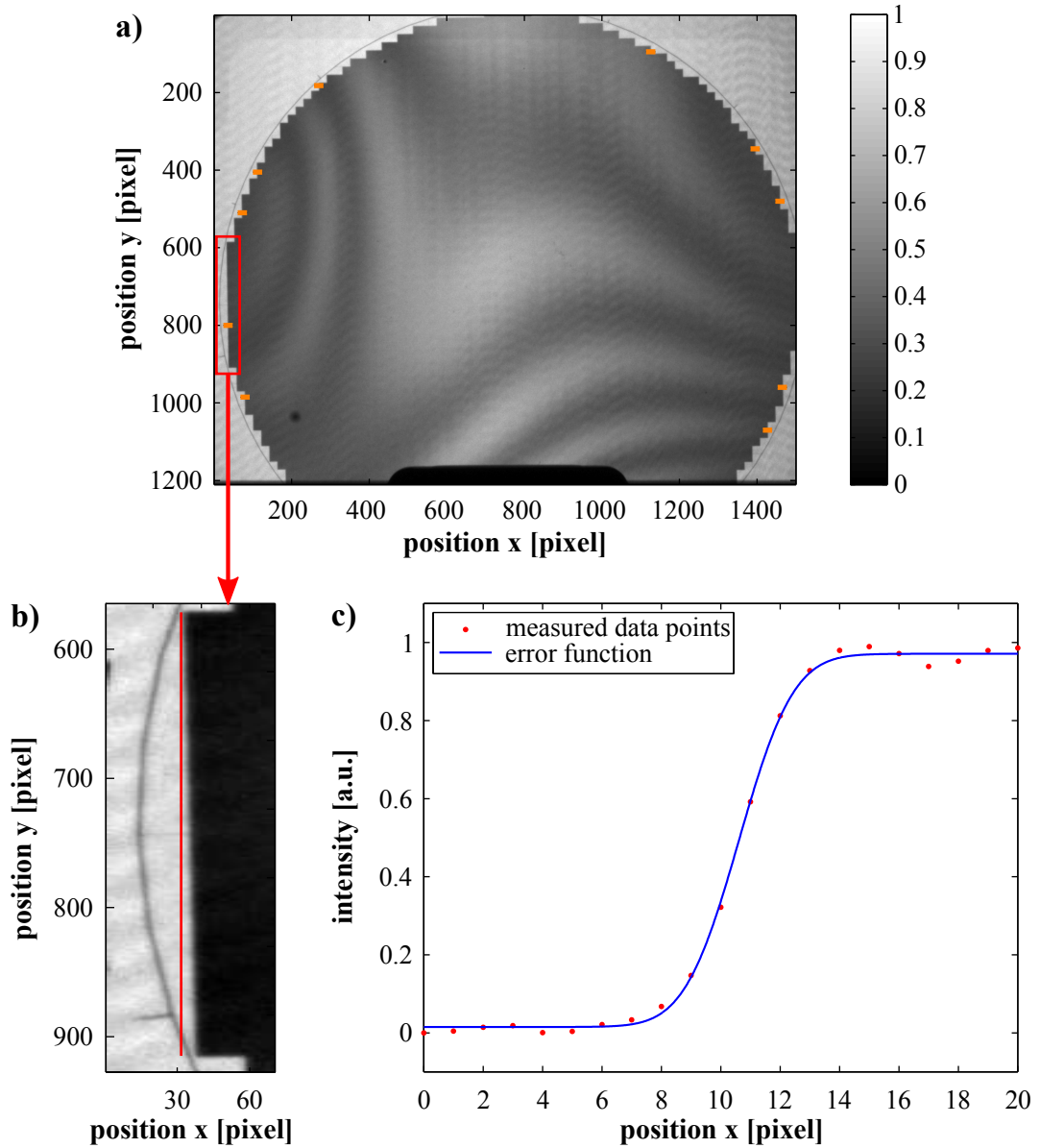


Figure 5.5: ESF measurements at the edges of the G_2 grating. **a)** Raw image of the detector showing the border between the effective grating and the surrounding waver. The edges used for the ESF measurements are indicated by orange lines. **b)** Magnified region from the left border of the raw image, to demonstrate the slight rotation of the grating relative to the detector axis. **c)** Edge spread function: The red dots show the data points obtained from one of the edges indicated in a). The blue curve represents the fit function in form of a linear combination of two error functions.

The described normalization and fitting procedure was executed for ten edges aligned parallel to the horizontal axis of the detector. The selected edges were distributed all around the grating, as indicated by the orange lines in Figure 5.5 a). A mean ESF was determined by calculating the sum of the individual edge spread functions and the averaged ESF was again normalized to 0 and 1. The entire procedure was repeated for ten edges along the vertical axis.

Wedge in the object plane

With the experimental setup presented above, the ESF in the plane of the G₂ grating immediately in front of the detector is determined, but the practically more valuable information is the ESF in the plane, where the sample is usually placed. For this reason, a small wedge of aluminum was built and fixated on the animal positioning stage as parallel as possible to the axis of the stage. To circumvent problems in the analysis of the image due to Moiré fringes, the G₂ grating was dismounted for this experiment as shown in Figure 5.6. The remaining intensity fluctuations, due to imperfections of the G₀ and G₁ gratings, were eliminated by recording a reference image of the background without a sample (Fig. 5.6 b)) and subtracting it from the image of the sample (Fig 5.7 a)). The resulting normalized image (Fig 5.7 b)) was used for further analysis. Due to the fact that the tip of the wedge was too thin to provide enough bright-to-dark contrast, the thick end of the wedge was used to record the edge profiles. A region of interest of 200 pixel lines, as indicated by the red rectangle in Figure 5.7 b), was chosen and ten single lines distributed over the entire region of interest were analyzed in the same way as the edges of the grating in the previous section.

In this arrangement, where the measured edge has a not negligible thickness, the angle between the axis of the beam direction and the axis along the depth of the wedge plays a crucial role. If the axes are not aligned parallel, the resulting edge profile on the detector is broadened, as illustrated in Figure 5.8. Since this angle was not controllable in a feasible way by positioning the wedge relative to a given gantry position, a series of images with varying gantry rotation angles and a fixed wedge position were recorded and analyzed. Subsequently, the optimal gantry angle relative to the position of the wedge was determined by finding the image with the narrowest edge profile. For the found angle, additional images in 2×2 binning and 4×4 binning mode were recorded by using the binning mode implemented in the Skyscan control software. In this mode, the values of the neighboring 2×2 or 4×4 pixels are summed up after the detector readout, which results in an increased effective pixel size of the acquired images. Analysis and processing of the binned data was the same as for the unbinned data.

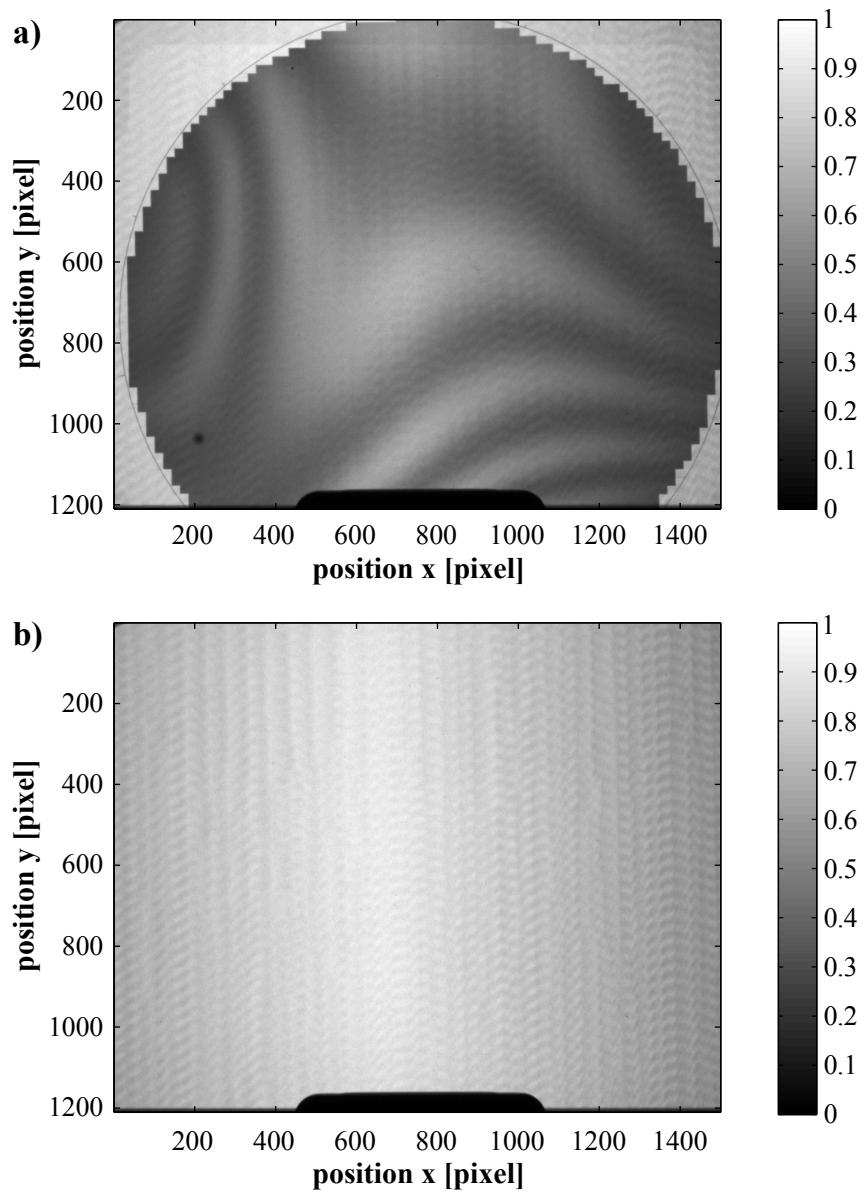


Figure 5.6: Normalization of the image of the wedge in the object plane: Part I.
a) Raw image of the field of view with mounted G_2 grating. **b)** Raw image of the field of view with dismounted G_2 grating used as reference image for the normalization of the wedge image.

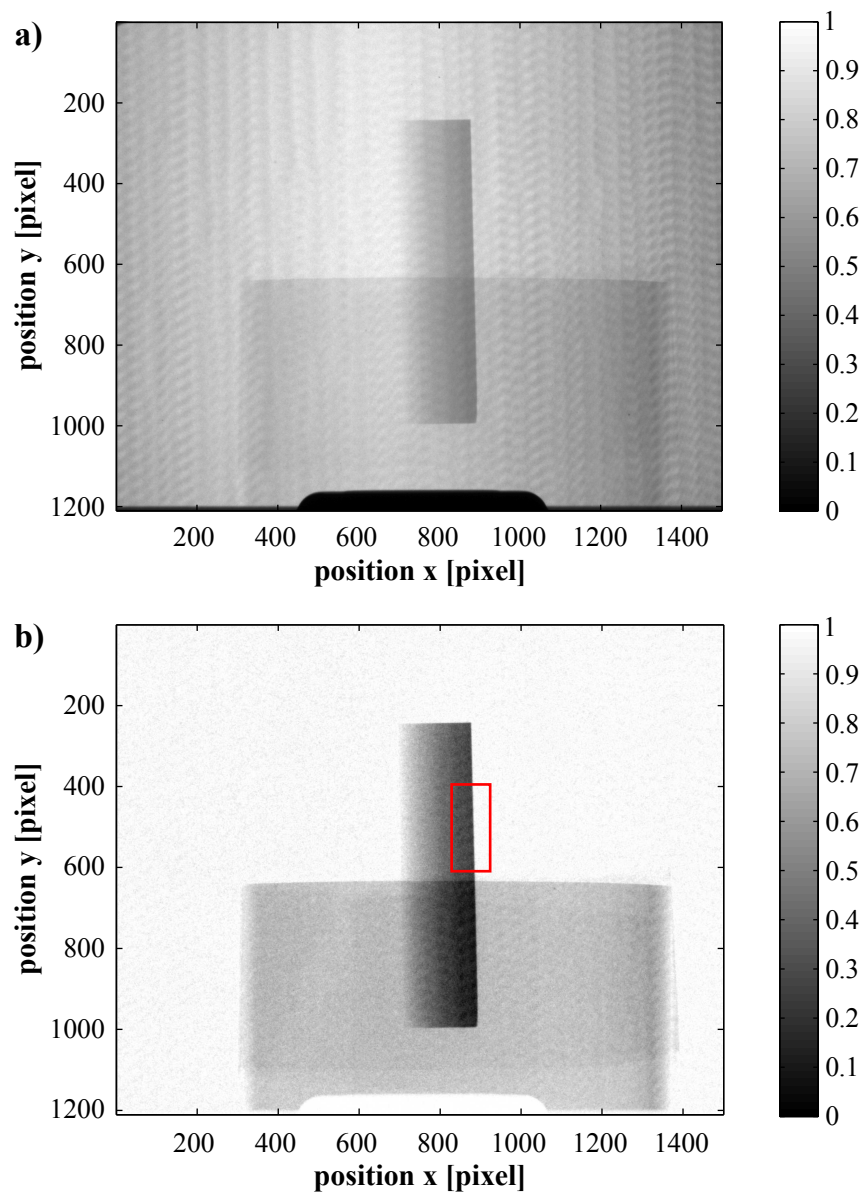


Figure 5.7: Normalization of the image of the wedge in the object plane: Part II.
a) Raw image of the aluminum wedge attached to the animal bed with dismounted G₂ grating.
b) Normalized image of the wedge. The region of interest for the edge profile measurements is illustrated by the red rectangle.

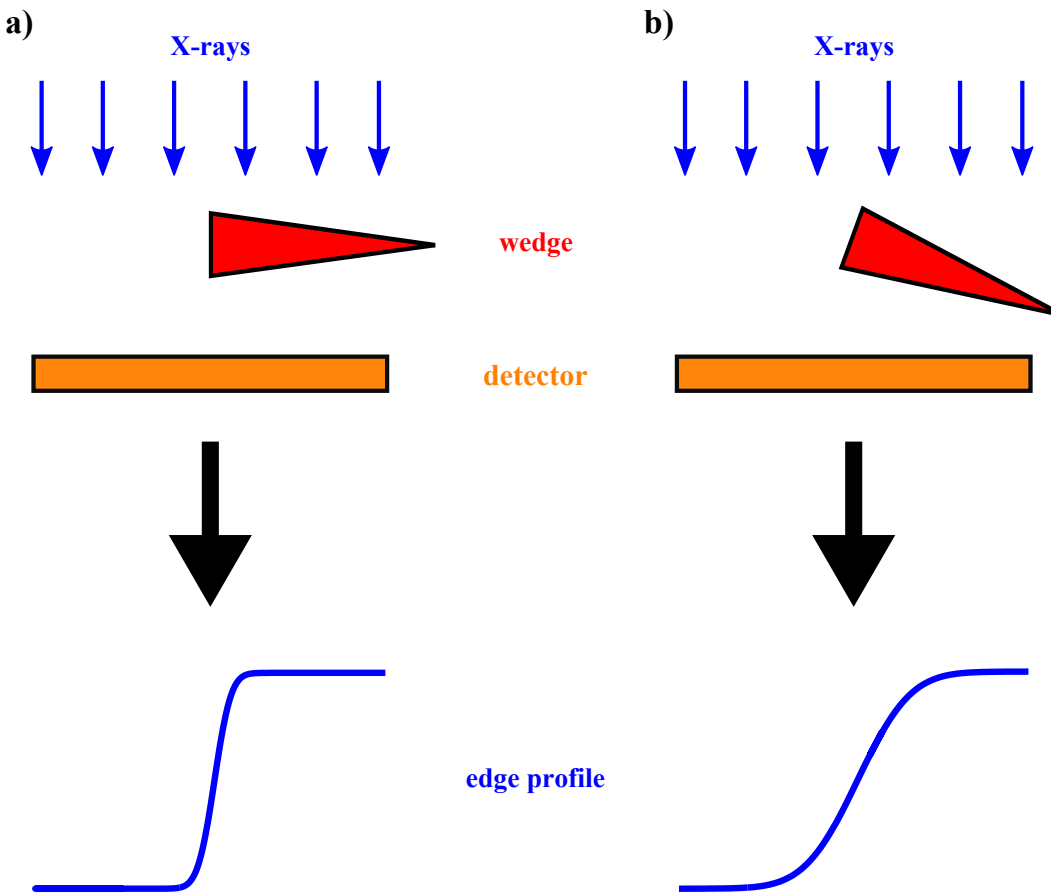


Figure 5.8: Influence of beam direction relative to the alignment of the wedge on resulting edge profile. For simplification, the wedge is represented by its two-dimensional base and parallel beam geometry is assumed. **a)** The short side of the equilateral triangle is aligned parallel to the direction of the incoming X-ray beam. The resulting edge profile is indicated below. **b)** The short side of the equilateral triangle is inclined by some angle to the beam direction. Thus, the edge spread function is broadened compared to the edge profile in a).

Rod in the object plane

The presented procedure of adjusting the gantry rotation angle relative to the wedge position was only realizable when the wedge was aligned parallel to the vertical axis of the detector, since this axis is also parallel to the rotation axis of the gantry. Consequently, only the edge spread function in the horizontal direction could be assessed by this procedure. In order to still get some information about the edge spread function in the vertical direction, the wedge was replaced by a thin metal rod with a cylindrical shape. This rod did not provide such a sharp edge as the wedge, but the resulting edge profiles were independent of the incoming beam angle, due to the circular base of the rod. Images were recorded with the rod aligned sufficiently parallel or perpendicular to the rotation axis of the gantry, so that angular

corrections could be disregarded. The edge profiles were ascertained in exactly the same way as for the wedge.

Wedge and rod in the source plane

To estimate the influence of the source profile on the spatial response of the system, the edge profile measurement is ideally performed close enough to the focal spot of the source, so that the MTF of the detector can be ignored. For the sake of convenience, the plane sufficiently close to the source to meet this requirement is named source plane in this thesis.

Since it was not possible to conduct such an experiment within the scanner and the dismounting of the source would have been too complicated and time-consuming, the same X-ray tube model was characterized in another setup. This setup consisted of the mentioned X-ray tube, a conventional CT rotation stage, and a flat panel sensor with a pixel size of $48 \mu\text{m}$. The rotation stage was positioned as close as possible to the source. The distance between the exit window of the source and the center of the rotation stage was 6 cm, and the distance between the stage and the detector was 84 cm. The process of measurement was completely analog to the experiment in the object plane and the images were also recorded at 45 kVp with 1 s exposure time. The wedge was positioned at the center of the rotation stage with the axis along the height of the wedge parallel to the rotation axis of the stage. The thick end of the wedge was used to create the edge profile, the ideal alignment of the axis along the depth of the wedge and the beam direction was found by analyzing images at varying angles of the rotation stage.

In order to estimate the two-dimensional source profile, the rod was recorded in horizontal and vertical alignment.

The region of interest for the images of the wedge and the rod in the source plane was chosen in the same way as for images from the object plane. Instead of a combination of two error functions, a single error function was fitted to the data, since this fit function represented the profiles with the same accuracy.

5.2.2 Data processing

To get from the measured edge spread functions of the various edge profile measurements to the corresponding line spread functions and modulation transfer functions, the following operations were executed: As mentioned before, the averaged ESF was represented by a linear combination of two error functions normalized to 0 and 1. From the obtained analytical representation of the ESF, the line spread function was subsequently calculated by analytical differentiation. The procedure of calculating the LSF analytically from a fit function was chosen, since the peak of the LSF could not be determined unambiguously by discrete differentiation.

The resulting LSF had the shape of a linear combination of two Gaussian functions, because the error function is an antiderivative of the Gaussian function, as mentioned before. The resulting LSF required no further normalization, as it was already normalized to unity area by the process of normalizing the ESF to 0 and 1. The MTF was then obtained by calculating the analytical Fourier transform of the normalized LSF. The calculation of the absolute of the Fourier transform was unnecessary, as the Fourier transform of a combination of Gaussian functions, symmetric to the origin, is again a combination of Gaussian functions, symmetric to the origin of the frequency spectrum. The stepwise process to get from the ESF to the MTF is shown in Figure 5.9. Please note that for the measurements in the source plane, the resulting LSFs and consequently also the MTFs have the shape of a single Gaussian symmetric to the origin.

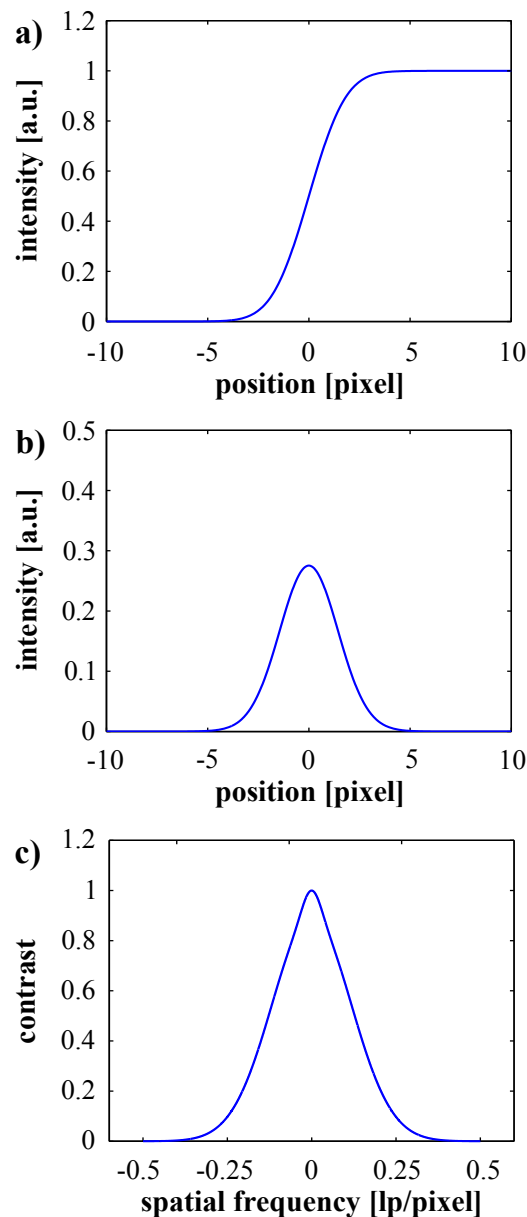


Figure 5.9: Scheme of data processing for the edge profile measurements. **a)** Averaged edge spread function. **b)** Symmetric line spread function calculated by analytical differentiation of the edge spread function. **c)** Symmetric modulation transfer function obtained by calculating the absolute of the analytical Fourier transform of the normalized LSF.

5.3 Results and discussion

In this section, the results of the various direct and indirect modulation transfer measurements, delineated in the prior sections, are presented and the consequences of the individual results for practical imaging purposes are discussed. For the sake of clarity, no error bars are displayed for the modulation transfer functions and line spread functions in this section. The resolution measures presented for each result were introduced to estimate the maximal resolution of the system by a single parameter. The exact definitions of these parameters can be found in Section 2.5.4. For the resolution measures, an error estimation is given based on the standard deviations of the fit functions and the standard deviations of the averaged results. The errors were deduced independently for each resolution measure in pixel units and subsequently converted to millimeter by using the respective pixel conversion factors.

All shown modulation transfer functions were normalized to unity at the origin to make them more easily comparable. The displayed line spread functions scaled in pixels are all normalized to unity area. For the case of different pixel conversion factors, such as in Section 5.3.3 and 5.3.5, the corresponding LSFs in millimeter are adapted to comprise the same area.

5.3.1 Direct modulation transfer function measurements

Results

Figure 5.10 shows the obtained MTFs and LSFs from the Moiré measurement analyzed with the different methods explained in section 5.1.1. The corresponding resolution measures are given in Table 5.1. The measurements were conducted at 35 and 45 kVp, but since the results were identical within the limits of accuracy of the measurements, only the results for 45 kVp are displayed. The arrangement of the fringes was parallel to the horizontal axis of the detector, as shown in Figure 5.1. Consequently, the presented results describe the spatial system response along the horizontal axis of the imaging system.

The Moiré fringes were effectively created in the plane of the G₂ grating, which is positioned in contact with the detector. Considering that there was no actual magnification due to the cone beam setup, the effective pixel size for the Moiré measurement was the pixel size of the flat-panel detector, which is 50 μm. Thus, the applied conversion factors from pixel to millimeter, which is a common unit for displaying MTFs and LSFs, are given by

$$1 \text{ pixel} = 0.05 \text{ mm}, \quad (5.7)$$

$$1 \text{ lp/pixel} = 20 \text{ lp/mm}. \quad (5.8)$$

The measured MTFs end at 6.28 lp/mm, which equals 0.314 lp/pixel. As mentioned before, this represents the maximum spatial frequency of Moiré pattern that was technically achievable with the setup and does not mean that this was the highest frequency, a non-zero contrast could be measured for.

The progression of the MTF curves differs strongly. The curve of the Standard method

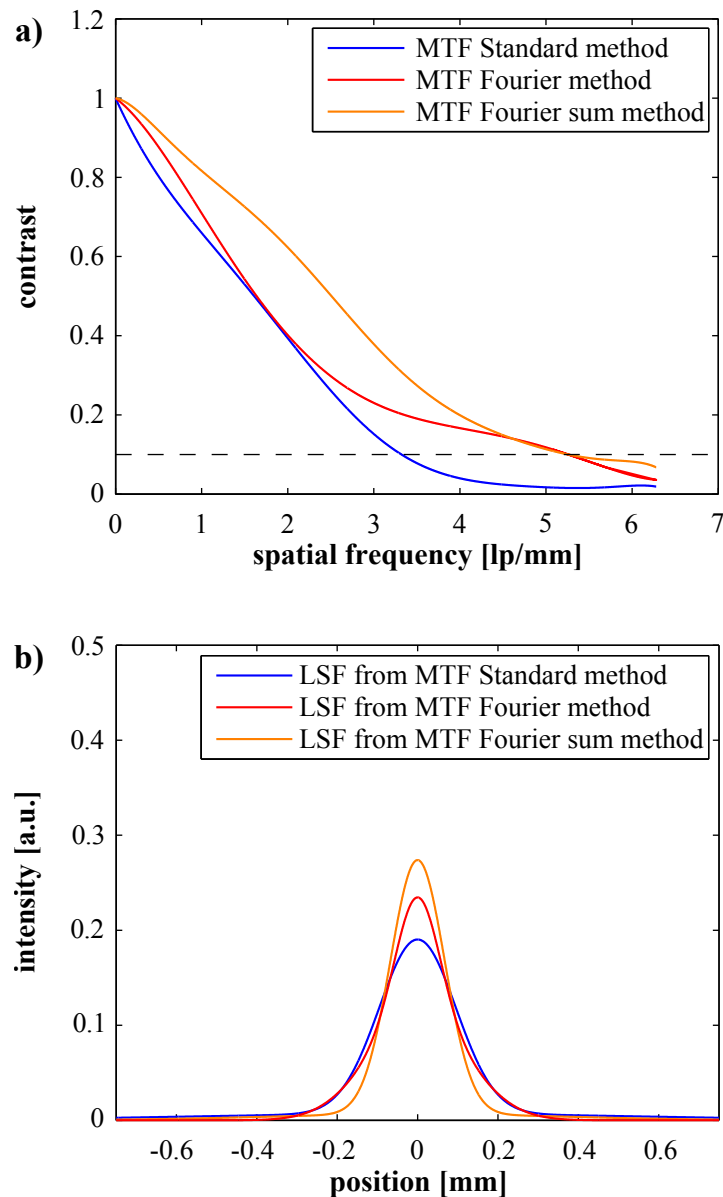


Figure 5.10: Results of the Moiré measurement at 45 kVp.
a) Modulation transfer functions obtained from Moiré patterns created with the scanner. The fringes were aligned parallel to the horizontal axis of the detector. The three different methods to deduce the MTF are described in the Section 5.1.1. The dashed line represents 10% of the MTF. **b)** Normalized line spread functions calculated from the MTFs above by the routine explained in the Section 5.1.2.

Resolution measure	Standard method	Fourier method	Fourier sum method
10% MTF [μm]	151 ± 10	95 ± 10	95 ± 10
FWHM of LSF [μm]	232 ± 10	175 ± 10	161 ± 10
FW of 10% LSF [μm]	442 ± 20	425 ± 20	303 ± 20

Table 5.1: Resolution measures obtained by different analysis methods from the data of the Moiré pattern measurements.

decreases rapidly with an almost constant slope over a large section of the frequency range. When it reaches its minimum around 5 lp/mm, it remains stable up to the cut-off frequency. The curve of the Fourier method shows similar behavior for low spatial frequencies up to approximately 2 lp/mm, while for higher frequencies the Fourier method curve drops more slowly and has its minimum at the cut-off frequency. The curve of the Fourier sum method declines significantly more slowly than the other two curves at low spatial frequencies. In an interval between approximately 4.5 and 5.5 lp/mm the functions of the Fourier sum method and the Fourier method display very similar values. Since the curves cross the 10% MTF level within this interval, the 10% MTF resolution measure is approximately equal. For higher frequencies, the values of the Fourier sum method are roughly constant, whereas the Fourier method curve decreases steadily.

The shown line spread functions were found by fitting a combination of two Gaussian functions to the calculated discrete data points. Consequently, the LSFs cannot be uniquely described by its full width at half maximum (FWHM) and an additional resolution parameter describing the full width at 10% of the LSF is introduced, as already stated in Section 2.5.4. The fact that the LSF of the Standard method is broader than the others seems obvious, since the corresponding MTF shows a lower contrast over the entire range of spatial frequencies than the MTFs of the Fourier methods. In contrast, the significant discrepancy in the width of the curves from the Fourier methods is an illustrative example to demonstrate that a single resolution measure gives only very limited information about the spatial system response of an imaging system. As mentioned before, the 10% MTF resolution measure is alike for both MTF curves, while the behavior at lower spatial frequencies of the MTFs disagrees strongly and hence the full width at 10% of the resulting LSFs differs significantly.

Discussion

As explained before, the Standard method and the Fourier method produce very similar results for an ideal sinusoidal distribution, perfectly aligned and with no background intensity fluctuations or noise. However, particularly for high frequencies, the MTF of the Fourier method shows significantly higher contrast transfer than the MTF of the Standard method.

A substantial reason for this is the process of averaging along the vertical axis of the region of interest, as applied in the Standard method. This step was necessary to get rid of the high-frequency noise, since the separate analysis of single lines was not feasible. The averaging process is very easily affected by the relative alignment of the entire Moiré pattern to the direction of averaging. For high frequencies, very small angles of rotation of the pattern

relative to the axis of averaging result in a drastic underestimation of the contrast³. On the contrary, the evaluation of contrast with the Fourier method is not affected by misalignment of the entire pattern, since a relative rotation of the pattern to the vertical axis does not influence the magnitudes of the center peak and the frequency peak, but moves the position of the frequency peak in the two-dimensional Fourier spectrum on a circle, centered in the origin, with a radius corresponding to the spatial frequency of the pattern. Additionally, the anisotropic distribution of the background intensity, due to the shadowing from the gratings, might still influence the outcome of the contrast analysis with the Standard method, despite the fact, that the maxima and minima of the fringes were determined independently for five fringes distributed over the entire region of interest. The results of the Fourier method are not affected by this effect, since the long-range intensity distribution of the background are reflected in the frequency spectrum by low-frequency components close to region around the center, but do not influence the magnitude of the center peak.

A further issue was the fact that within an entire Moiré pattern, fringes were not always aligned perfectly parallel to each other and sometimes varied in thickness and spacing over the chosen region of interest. This leads again to underestimation of the contrast with the Standard method, but also affects the Fourier method. The variation in thickness and spacing of the fringes is represented by slightly different spatial frequencies in the Fourier spectrum. Considering that the Fourier method accounts only for the peak value of the frequency distribution, other frequencies, which also contribute to the total contrast of the pattern, are not included in the analysis.

This might also explain why the MTF of the Fourier sum method exhibits higher contrast transfer values than the Fourier method over a long range of the spatial frequency spectrum. For the contrast estimation of the Fourier sum method, the directly neighboring values to the center peak and frequency peak in the discrete Fourier spectrum are also taken into account, given they exceed a certain threshold and consequently contribute significantly to the amplitude or the offset of the sinusoidal pattern. In the presented data, the adjacent values to the center peak only exceed the threshold in the horizontal direction, which can be interpreted as the low-frequency background intensity distribution from the shadowing towards the lateral edges of the field of view. In contrast, for most of the analyzed patterns all eight adjacent values around the frequency peak exceed the threshold value by far and thus contribute to the estimation of the amplitude of the fringes. Since the frequency peaks in the analyzed data become sharper for higher frequencies, the relative impact of adjacent values to the amplitude gets smaller for higher frequencies. As a consequence of this, the estimated contrast transfer values by the Fourier sum method are considerably higher for relatively low spatial frequencies compared to the Fourier method, while they are comparable for higher frequencies.

Assuming that the Fourier sum method provides the most realistic results, leads to the conclusion that the Fourier method may describe the real spatial system response to some extent correctly for high spatial frequencies and the Standard method basically underestimates the system response over the entire frequency range. This assumption is discussed more detailed in the following sections.

³ Assuming a perfect pattern with a spatial frequency of 0.1 lp/pixel and a rotation angle of 3 degree between the pattern and the axis of averaging, the resulting contrast averaged over 200 pixels would be zero already.

5.3.2 Source characterization

Results

The results presented in this section were obtained from a different experimental setup, as mentioned in Section 5.2.1. Considering the magnification factor of 15, calculated by the ratio of the source-to-detector distance to the source-to-sample distance, and the pixel size of $48 \mu\text{m}$, the pixel conversion factors for the experiment in the source plane are given by

$$1 \text{ pixel} = 0.0032 \text{ mm}, \quad (5.9)$$

$$1 \text{ lp/pixel} = 312.5 \text{ lp/mm}. \quad (5.10)$$

Since the data were acquired with a different setup, the application of the results to the scanner is very limited. For this reason, the results are only given in terms of resolution measures.

It is worth mentioning that the resolution measures presented in Table 5.2 are obtained from line spread functions with a shape of a single Gaussian function and consequently do not have long tails like the LSFs from the other results⁴. This is reasonable, since the intensity profile of the focal spot can be expected to have a relatively flat center region and to decrease very steeply at the margins, without exhibiting strongly pronounced tails.

Resolution measure	Wedge horizontal	Rod horizontal	Rod vertical
10% MTF [μm]	18 ± 2	24 ± 3	23 ± 3
FWHM of LSF [μm]	30 ± 3	39 ± 4	37 ± 4
FW of 10% LSF [μm]	62 ± 6	80 ± 8	77 ± 8

Table 5.2: Resolution measures obtained from the edge profile measurements conducted in the source plane.

Discussion

For the discussion of the edge profile experiments in the source plane, it is essential to consider that a modulation transfer function describing a linear, shift-invariant imaging system, is a product of the individual MTFs of the components of the system, as already stated in Section 2.5. The MTF of the setup used to characterize the X-ray tube consists of the detector and the source MTF, their relative distributions to the total MTF depend on the position of the sample. Assuming that f is the spatial frequency of the recorded object and M is the magnification factor for the plane where the object was placed, the total MTF of the system

⁴ The presented LSFs are uniquely described by their FWHM. The FW 10% resolution measure is only given to make the results of this section more easily comparable to the other results.

can be described by the following equation:

$$MTF_{system}(f) = MTF_{source}\left(\frac{M-1}{M}f\right) \times MTF_{detector}\left(\frac{f}{M}\right). \quad (5.11)$$

Considering a magnification factor of 15 for the used setup, the detector MTF can be neglected and the found results in this section basically describe the influence of the source profile on the spatial system response. Therefore, the calculated resolution measures in Table 5.2 can be used to estimate the focal spot size of the source.

The exact shape and symmetry properties of the two-dimensional source profile of the X-ray tube are difficult to predict since it depends on various factors, such as the exact anode angle and the focal spot of the electron beam. However, the results obtained from the rod measurement in the source plane indicate that the spatial system response of the source is the same in the horizontal and the vertical direction. This agrees with a square focal spot size of $50 \mu\text{m} \times 50 \mu\text{m}$, given in the data sheet of the X-ray tube [44].

It is hard to tell, how far the obtained results can be applied to the spatial system response of the source in the scanner, since they were not acquired with the very same source, but with the same X-ray tube model. Moreover, the G_0 grating immediately in front of the X-ray tube in the scanner might also influence the effective source profile and was not present in the setup used to characterize the source. Nevertheless, the calculated resolution measures are feasible to give a rough approximation of the focal spot size of the source and are used in following to estimate the influence of the source profile on the system MTF in a particular imaging plane.

5.3.3 Edge profile measurements

Results

In this section, the results of the edge profile measurements at the edges of the G_2 grating are compared to those performed with the wedge in the object plane. Both experiments were carried out at 45 kVp and the line profiles were measured in both cases in the horizontal direction of the X-ray camera as depicted in Figure 5.5 and Figure 5.7.

In Figure 5.11, the results are plotted in pixel units, whereas the same results are shown in millimeter in Figure 5.12. This is due to the different pixel conversion factors used for the conversion of the results from pixel to millimeter. The first experiment, which is referred to as the G_2 edge measurement, took place in the detector plane and therefore the same conversion factors were applied as presented in Equations 5.7 and 5.8. The second experiment, which is referred to as the wedge edge measurement, was executed in the plane where the sample usually is positioned. Due to the magnification caused by the cone beam geometry, the effective pixel size in this plane was $29 \mu\text{m}$. Consequently, the resulting pixel conversion factors are given by

$$1 \text{ pixel} = 0.029 \text{ mm}, \quad (5.12)$$

$$1 \text{ lp/pixel} = 34.48 \text{ lp/mm}. \quad (5.13)$$

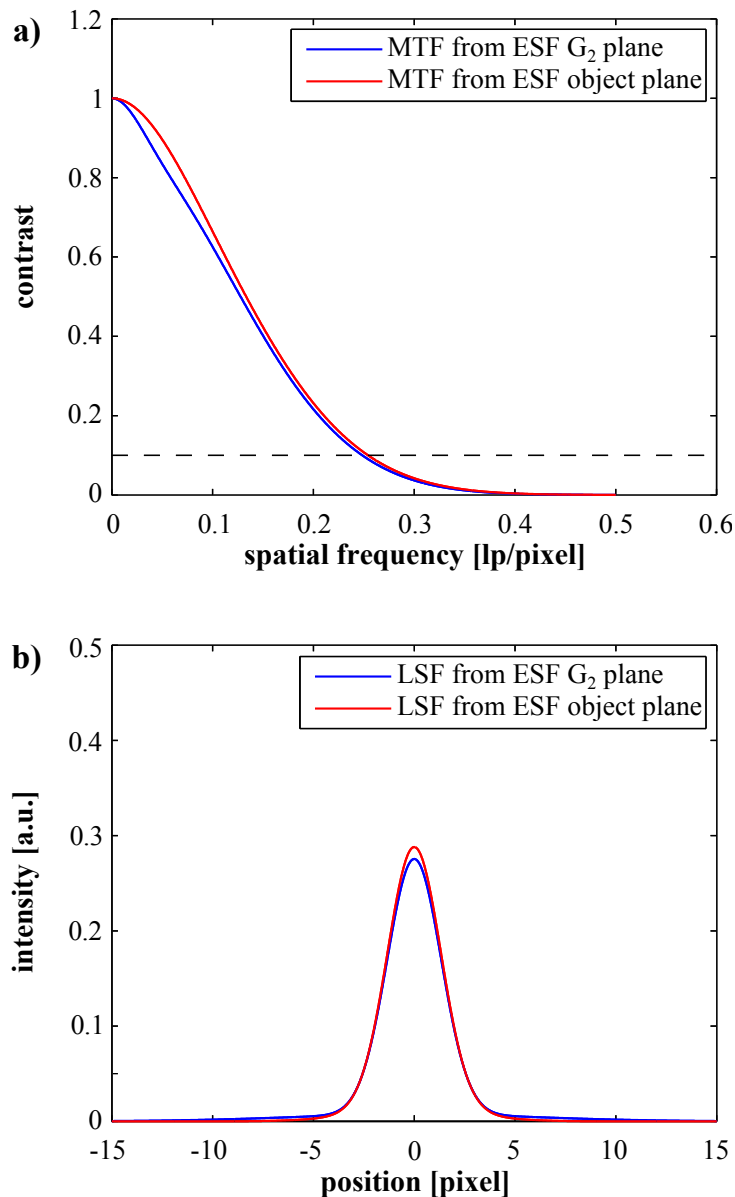


Figure 5.11: Results of the edge profile measurements in pixel.

a) Modulation transfer functions calculated from the line spread functions below. The dashed line represents 10% of the MTF. b) Normalized line spread functions obtained from the edge profile measurements at the edges of the G₂ grating and at the edge of the wedge positioned in the object plane. In both measurements, the edge profiles were measured in parallel direction to the horizontal axis of the detector.

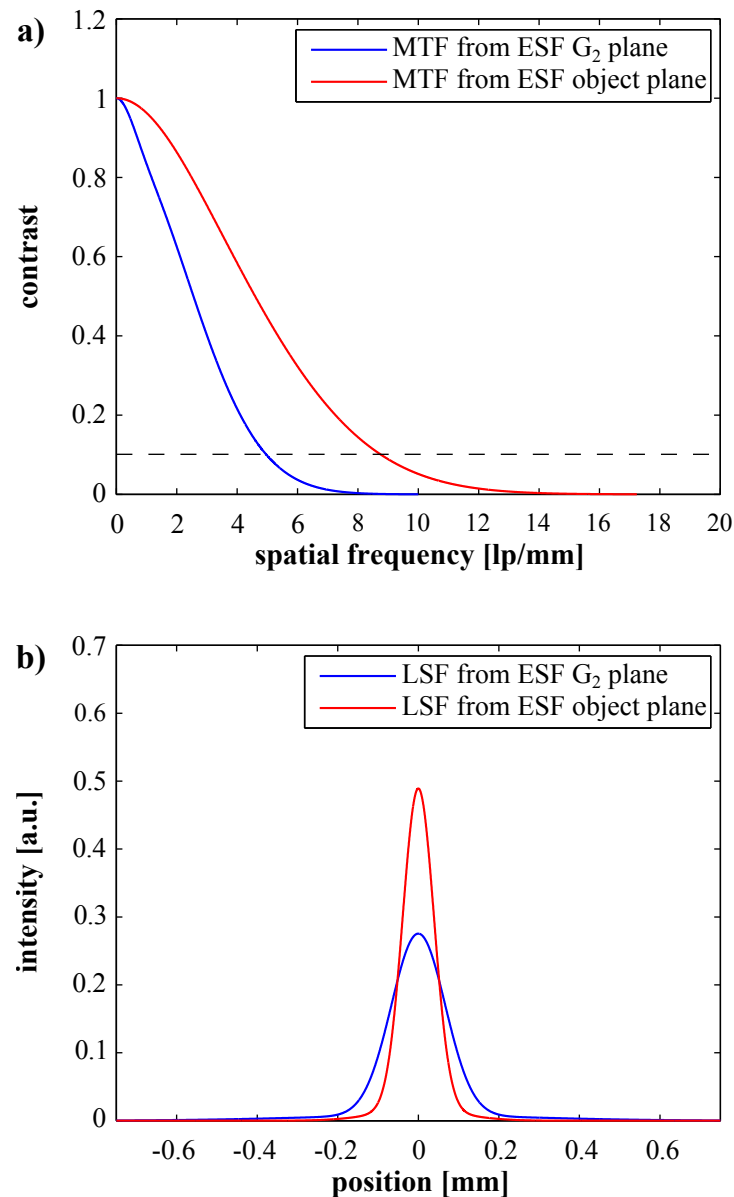


Figure 5.12: Results of the edge profile measurements in mm.

a) Modulation transfer functions calculated from the line spread functions below. The dashed line represents 10% of the MTF. **b)** Normalized line spread functions obtained from the edge profile measurements at the edges of the G₂ grating and at the edge of the wedge positioned in the object plane. In both measurements, the edge profiles were measured in parallel direction to the horizontal axis of the detector.

Resolution measure	G_2 edge measurement	Wedge edge measurement
10% MTF [pixel]	2.02 ± 0.15	1.98 ± 0.15
FWHM of LSF [pixel]	3.21 ± 0.20	3.19 ± 0.20
FW of 10% LSF [pixel]	6.04 ± 0.30	5.99 ± 0.40
10% MTF [μm]	101 ± 8	57 ± 4
FWHM of LSF [μm]	161 ± 10	93 ± 6
FW of 10% LSF [μm]	302 ± 15	174 ± 12

Table 5.3: Resolution measures obtained from the edge profile measurements at the edges of the G_2 grating and at the wedge in the object plane.

In Figure 5.11, the MTFs and LSFs were obtained by an analog procedure, which is explained in Section 5.2.2. The presented curves exhibit a very similar progression and the resolution measures in pixel, presented in Table 5.3, are equal within the present accuracy of measurement.

In contrast, the curves scaled to millimeter in Figure 5.12 are obviously very different. They represent the effective modulation transfer and line spread functions for the respective image planes where the experiments took place.

Discussion

For the discussion of the edge profile experiments in different planes relative to the X-ray camera, the MTF of the scanner is assumed to consist basically of the detector and the source MTF⁵ and can be described by the same formula as used for the source characterization (Equ. 5.11).

The measurement of the G_2 edges took place immediately in front of the detector, thus the magnification factor was practically unity and, according to Equation 5.11, the deduced MTF represents only the detector MTF. For the wedge experiment, the situation is different: Since the wedge was positioned in the typical object plane, the magnification factor is about 1.7, and therefore the source MTF contributes considerably to the total MTF of the imaging system. However, the resolution measures from the source measurement (Tab. 5.2) imply that the impact of the source is so small that it can still be ignored within the measurement accuracy. This can be demonstrated by assuming that the LSFs of detector, source, and the entire system are described by normal distributions with varying standard deviations. By inserting the Fourier transforms of the normal distributions into Equation 5.11, one can derive that the FWHM of the system LSF for a magnification factor of 1.7 is given by

$$FWHM_{system} = \sqrt{0.17 FWHM_{source}^2 + 0.35 FWHM_{detector}^2}. \quad (5.14)$$

⁵ The contribution of the gratings to the total MTF is not considered as an independent factor here. This is discussed further in Section 5.4.

To estimate the source influence, a FWHM of $50 \mu\text{m}$ for the source profile is assumed, which is significantly larger than the determined resolution measure. The particular value is chosen to compensate for a possible underestimation of the source profile due to the G_0 grating and differences between the characterized X-ray tube and the tube in the scanner. For the FWHM of the detector in this example, the calculated FWHM of the G_2 edge measurement ($161 \mu\text{m}$) is used. By applying both values to Equation 5.14, one finds that the FWHM of the system in the object plane is $97.45 \mu\text{m}$. In comparison, when the contribution of the source to the system MTF is completely ignored, the FWHM is $95.25 \mu\text{m}$. Consequently, the influence of the source is smaller than the error estimations given for the resolution measures and can be neglected. Therefore, the line spread functions and corresponding modulation transfer functions, scaled in pixel, are expected to be roughly the same for the object and the detector plane, given the wedge and the G_2 provided knife edges with the same sharpness. This agrees well with the results in Figure 5.11 and Table 5.3.

The fact that the LSF of the wedge in the object plane is even slightly narrower than the LSF of the G_2 edges, may be explained by the processing of the images. The analysis procedure of the data was exactly analog for both measurements, but the analyzed image was not equivalent. For the image of the G_2 grating, no reference image for normalization was available, thus the unprocessed raw image was used for the analysis. In contrast, the image of the wedge was recorded in the absence of the G_2 grating and was normalized with a reference image. Therefore, the profiles from the G_2 grating might have been affected by residual Moiré fringes, noise of the background intensity, and potential vibrations of the entire G_2 grating, whereas these effects did not play a role for the normalized image of the wedge. However, the analysis of the unprocessed raw images of the wedge provided only marginally worse results than the analysis of the normalized image and the deviation of the results is negligible within the measurement accuracy. Another explanation could be that the wedge provided a slightly sharper knife edge than the edges of the G_2 grating.

The basic idea of comparing the results from the object and the detector plane in pixel scaling, is to point out the individual contributions of the source and the detector to the modulation transfer function of the entire system. However, the results in millimeter, for which the magnification factor of the cone beam is taken into account, provide more valuable information about the effective spatial system response of the imaging system. The wedge was positioned in the object plane, where the sample is usually placed. As mentioned before, the fact that the G_2 grating was dismounted can be neglected within the accuracy of measurement. Hence, the obtained results from the wedge measurements describe the spatial system response of the scanner for the usual imaging purposes⁶ and are therefore the most valuable results of all MTF measurements for practical considerations.

⁶ This is only valid for images obtained in the conventional attenuation contrast mode without phase stepping. The effective spatial system response of the AMP, DPC and DCI signals depends additionally on the phase stepping and the applied processing or reconstruction routines, which is further discussed in the Section 5.4.

5.3.4 Comparison of direct and indirect modulation transfer function measurements

Results

In this section, the results of the Moiré experiments and the edge profile measurements at the G₂ edges are compared. Since both measurements were performed in the detector plane, the same pixel conversion factors (Equ. 5.7, 5.8) were applied. The assessed direction of the spatial system response for both experiments was the direction along the horizontal axis of the X-ray camera and all the relevant parameters of the acquisition were identical for both measurements. Consequently, the results can be directly compared. For reasons of clear arrangement, only the results of the Moiré measurement, obtained by the Fourier sum method, are displayed in Figure 5.13, as they exhibit the highest agreement with the results of the edge experiment at the G₂ grating.

The MTF of the edge profile measurement is represented by two combined Gaussian

Resolution measure	G ₂ edge measurement	Fourier sum method
10% MTF [μm]	101 ± 8	95 ± 10
FWHM of LSF [μm]	161 ± 10	161 ± 10
FW of 10% LSF [μm]	302 ± 15	303 ± 20

Table 5.4: Resolution measures obtained from the edge profile measurements at the edges of the G₂ grating and the analysis of the Moiré pattern with the Fourier sum method.

functions, whereas the measured MTF is a polynomial function of 8th degree and hence has a less smooth shape than the Gaussians. Ranging up to a spatial frequency of approximately 4.5 lp/mm, the contrast values for both MTFs are very similar. For higher frequencies, the deviations become more significant.

An outstanding difference is the cut-off frequency of the depicted modulation transfer functions. The calculated MTF ends at 10 lp/mm, which is equivalent to 0.5 lp/pixel and thus the maximum frequency, which may theoretically be measured, while the measured MTF ends at 6.28 lp/mm due to technical reasons, as mentioned before. However, since the contrast values at the cut-off frequency are well below 10% contrast level, the missing part of the MTF does not influence significantly the calculation of the line spread function. This was also confirmed by the fact that for a completed MTF up to 0.5 lp/pixel, accomplished by interpolating or adding values in the order of the value at the cut-off frequency, the shape and consequently the FWHM and the FW at 10% of the resulting LSF remained practically the same. The corresponding resolution measures for the compared functions are listed in Table 5.4.

Discussion

The obtained resolution measures clearly demonstrate that both experiments can lead to equivalent results. The fact that the MTF from the Fourier sum method does not range up to the maximum spatial frequency of 10 lp/mm has no practical influence on the characterization

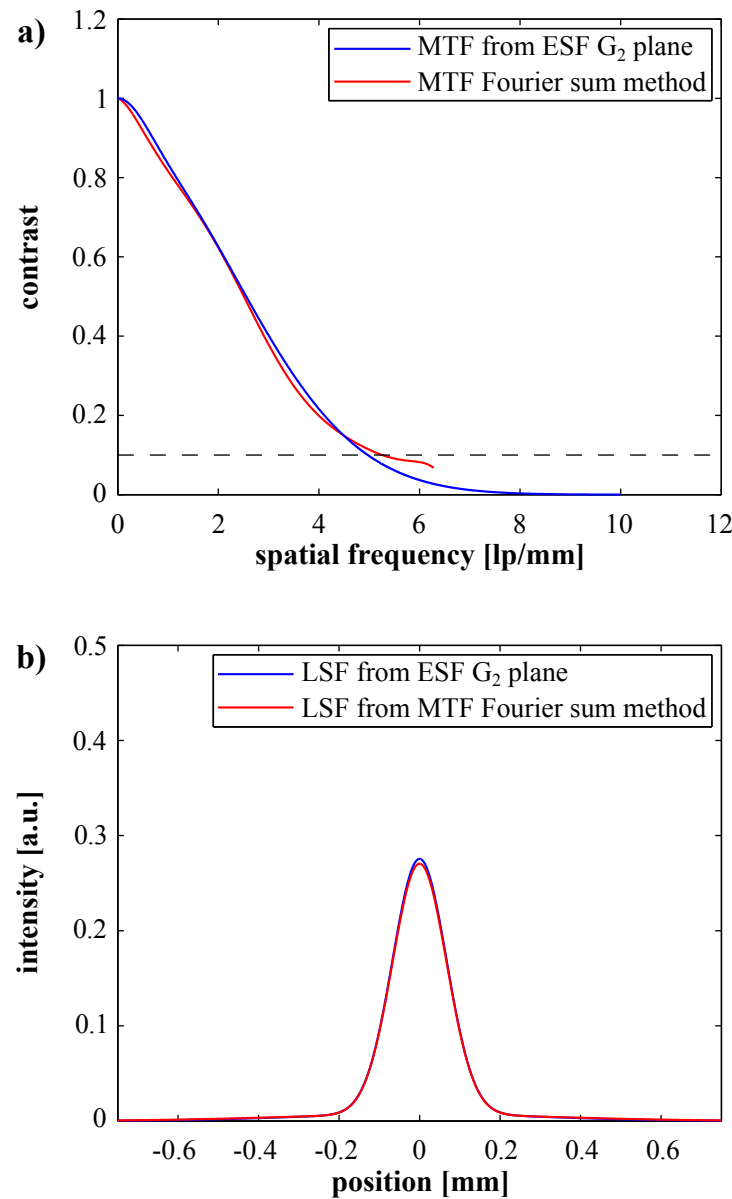


Figure 5.13: Comparison of the results for the edge profile measurements at the G₂ edges and the Moiré measurements. **a)** Modulation transfer functions. The dashed line represents 10% of the MTF. **b)** Normalized line spread functions. The results were obtained from edge profiles and Moiré fringes, both aligned parallel to the horizontal axis of the detector.

of the spatial system response. Given that the findings of the G₂ edge experiment describe the spatial system response appropriately, the results of this section confirm the assumption that the Fourier sum method provides the most realistic results of the three presented methods to analyze the Moiré pattern.

Considering the findings of this comparison, it can be stated that the basic idea of using Moiré fringes, produced by the gratings in the scanner, to create periodic intensity patterns for the direct MTF evaluation in the detector plane is generally feasible. However, the correctness of the results depends strongly on the analysis method of the fringes, as explained in Section 5.3.1.

In summary it can be stated, that both experiments can provide appropriate results, while the edge profile measurement has the advantage to be more reliable and to be easier to perform and to analyze.

5.3.5 Comparison of binned data from the edge profile measurements

Results

In this section, the results of the knife edge experiment in the object plane are shown for several binning configurations. The unbinned reference result is the same as already presented in Section 5.3.3. The binned images were obtained by software binning as reported in Section 5.2.1. The mode, referred to as 2×2 binning uses an effective pixel size of 100 μm, which is twice the physical size of a normal detector pixel; accordingly the 4×4 binning mode uses an effective pixel size of 200 μm. Considering the magnification factor of the cone beam setup, as explained before, and the effective pixel size in the detector plane, the resulting pixel conversion factors for the 2×2 binning mode are given by

$$1 \text{ pixel} = 2 \times 0.029 \text{ mm} = 0.058 \text{ mm}, \quad (5.15)$$

$$1 \text{ lp/pixel} = 1/2 \times 34.48 \text{ lp/mm} = 17.24 \text{ lp/mm}. \quad (5.16)$$

The conversion factors for the 4×4 binning mode are determined correspondingly by replacing the factors of 2 and 1/2 in the equations above by 4 and 1/4.

The modulation transfer functions, plotted in Figure 5.14 have very different cut-off frequencies. This is due to the fact that each modulation transfer function ends at the maximum frequency of 0.5 lp/pixel, since at least two pixels are necessary to resolve a line pair, irrespective of the size of the pixels. By applying the pixel conversion factors above, the corresponding cut-off frequencies in millimeter are 17.24 lp/mm for the unbinned case, 8.62 lp/mm for the 2×2 binning mode and 4.31 lp/mm for the 4×4 binning mode. From the progressions of the curves, it can be seen that the spatial system response for the 2×2 binning case, is very similar to the unbinned case. In contrast, the curve from the 4×4 binning mode shows a significantly different behavior and decreases more rapidly.

The corresponding line spread functions were normalized to comprise the same area in millimeter scaling to make them more easily comparable. The LSFs obtained from the data with no binning and 2×2 binning are approximately equal, whereas the LSF, from images recorded with 4×4 binning, was considerably broader. In Table 5.5, the resolution measures

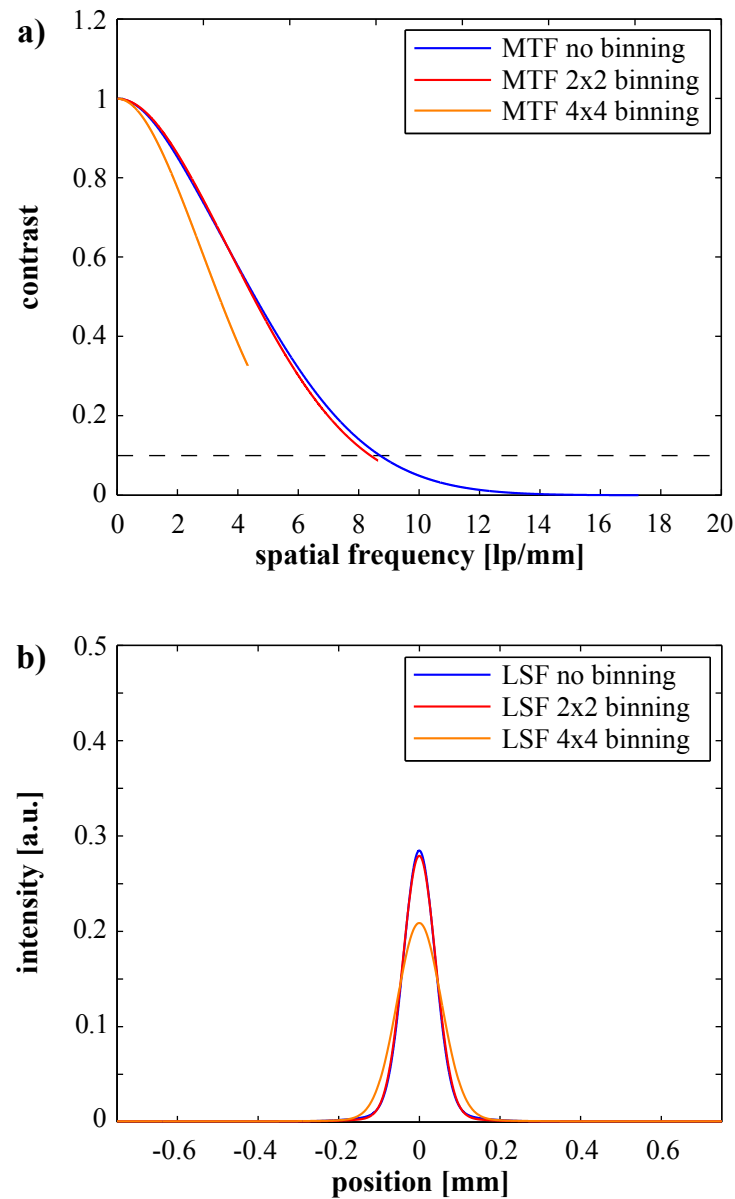


Figure 5.14: Comparison of the results from the wedge experiment in the object plane with different binning settings. **a)** Modulation transfer functions. The dashed line represents 10% of the MTF. **b)** Normalized line spread functions. The compared results were obtained with the same wedge alignment and describe the horizontal spatial system response.

Resolution measure	Wedge no binning	Wedge 2×2 binning	Wedge 4×4 binning
10% MTF [pixel]	1.98 ± 0.15	1.03 ± 0.10	–
FWHM of LSF [pixel]	3.19 ± 0.20	1.66 ± 0.20	1.11 ± 0.20
FW of 10% LSF [pixel]	5.99 ± 0.40	3.06 ± 0.40	2.05 ± 0.40
10% MTF [μm]	57 ± 4	60 ± 6	–
FWHM of LSF [μm]	93 ± 6	96 ± 12	129 ± 24
FW of 10% LSF [μm]	174 ± 12	177 ± 23	238 ± 48

Table 5.5: Resolution measures obtained from the edge profile measurements of the wedge in the object plane recorded with different binning modes.

for the binned results are compared to the unbinned case. Please note that the relative errors in pixel units for the resolution measures increase with the applied bin factor. This is due to the declined precision of the fit functions, since the binning reduces the number of data points available for the fits.

Discussion

The presented discussion is limited to the line spread functions, since the MTFs are directly calculated from the LSFs and thus do not provide new information.

In general, the width in millimeter of LSFs from binned data is expected to become broader compared to LSFs from unbinned data. The broadening of the fitted LSF depends on the bin factor applied to the raw data. Moreover, the absolute width of the unbinned LSF and thereby the number of points available for the fitting has to be considered to estimate the influence of a particular bin factor. Within the measurement accuracy, the resolution measures of the binned data are in good agreement with the expected results from theoretical considerations⁷. However, the reliability of the results for 4×4 binning is questionable, since the number of data points available to fit the error functions might have been too small to represent the edge profile appropriately. This is also expressed by the very large relative errors of the respective resolution measures compared to the other results.

In biomedical imaging, a basic consideration is to find the ideal ratio of noise minimization to the maximal spatial resolution for a particular experiment. Consequently, the obtained resolution measures from the binned images are of high practical relevance, since they estimate the maximal resolution obtained in the respective binning mode and hence provide valuable information to decide whether or not the respective binning mode is appropriate for a particular measurement. The resolution measures were determined for the raw images from the detector; hence, additional influences on the final resolution of the projection and CT data in

⁷ To simulate the behavior of the fit function for different binning settings, a Gaussian function with a FWHM of 3.2 pixel was sampled with the same number of points as available for the fit of the unbinned LSF. Different bin factors were applied to the data points and a Gaussian was fitted to the binned data. By this calculations one finds that the expected FWHM for the 2×2 binning is 1.72 pixel and the FWHM for the 4×4 binning is expected to be 1.05 pixel.

the different contrast modalities, such as the phase stepping procedure, the processing routine, and the applied reconstruction algorithm for CT data, have not been taken into account. Therefore, no conclusions about the maximal resolution in the respective imaging modality can be drawn from the presented results. Nevertheless, the fact that the resolution measures of the raw images are practically the same for the image acquisition in 2×2 binning mode and without binning suggests that the resolution of the processed images in the different contrast modalities might also be very similar for 2×2 binning and no binning. Considering the fact that the contrast-to-noise ratio improves with increasing bin factor, as demonstrated in Section 4.3.4, the results in Table 5.5 indicate that the 2×2 binning mode is generally preferable over the unbinned mode, since it provides better noise properties with a comparable resolution.

Furthermore, the results discussed in this section are important to determine the correct PSFs for the deconvolution procedure of the binned raw data which is further explained in Section 5.5.

5.3.6 Comparison of horizontal and vertical edge profile measurements

In this section, the spatial system response along the horizontal and vertical axis of the detector are compared. As mentioned before, reasonable results in the vertical direction could only be obtained from the edge profile measurements at the edges of the G₂ grating and from the experiments with the rod positioned in the object plane. Within the accuracy of the measurement, both experiments provided identical results for the horizontal and vertical direction and no significant difference in the shape of the compared functions could be seen, therefore the results are only given in terms of resolution measures.

Resolution measure	G ₂ edge measurement horizontal	G ₂ edge measurement vertical
10% MTF [pixel]	2.02 ± 0.15	1.97 ± 0.15
FWHM of LSF [pixel]	3.21 ± 0.20	3.17 ± 0.20
FW of 10% LSF [pixel]	6.04 ± 0.30	5.96 ± 0.30
10% MTF [μm]	101 ± 8	99 ± 8
FWHM of LSF [μm]	161 ± 10	159 ± 10
FW of 10% LSF [μm]	302 ± 15	298 ± 15

Table 5.6: Resolution measures from the edge profile measurements at the horizontal and vertical edges of the G₂ grating.

Edge profile measurements at the edges of the G₂ grating

The results for the vertical edge profile measurements at the edges of the G₂ grating were attained in the same way as for the horizontal direction. Since the horizontal and vertical edges of the border between the grating and the surrounding wafer were perpendicular to each other, the correction factor for the slight rotation of the grating relative to the detector was exactly the same for both directions and could be neglected in the applied line-by-line

analysis. The pixel conversion factors for the detector plane can be found in Equations 5.7 and 5.8. Consequently, the resolution measures, presented in Table 5.6, describe the horizontal and vertical spatial resolution in the detector plane.

Edge profile measurements with the rod in the object plane

The rod experiment was conducted in the object plane. Therefore, the same pixel conversion factors as for the knife edge experiment were applied (see Eq. 5.12, 5.13). The angular deviations in the alignment of the rod were small enough to be neglected in both cases. The data of both measurements were analyzed and processed in a completely analog way. Due to the circular shape of the rod, the resulting edge profiles were much broader than the profiles of the G₂ edges or the wedge; consequently, the absolute values of the resolution measures have little significance. Nevertheless, the results of the rod measurements, displayed in Table 5.7, can be used to compare the spatial system response in the object plane along several directions.

Resolution measure	Rod edge measurement horizontal	Rod edge measurement vertical
10% MTF [pixel]	2.36 ± 0.20	2.35 ± 0.20
FWHM of LSF [pixel]	3.77 ± 0.20	3.72 ± 0.20
FW of 10% LSF [pixel]	7.18 ± 0.40	7.18 ± 0.40
10% MTF [μm]	68 ± 6	68 ± 6
FWHM of LSF [μm]	109 ± 6	108 ± 6
FW of 10% LSF [μm]	208 ± 12	208 ± 12

Table 5.7: Resolution measures obtained from the edge profile measurements with the rod aligned in different directions in the object plane.

Discussion

The point spread function of the detector is expected to be approximately radially symmetric, since the matrix of the GOS scintillator can be assumed to be isotropic and the pixels of the detector have a quadratic shape and are sufficiently small. The results obtained from the edge profile measurements of the G₂ grating edges in horizontal and vertical direction (Tab. 5.6) confirm this assumption. Considering that the impact of the source focal spot can be ignored in the object plane, the point spread function at the typical sample position is also expected to be radially symmetric, which is confirmed by the results of the rod measurement in the object plane (Tab. 5.7). This is a very important result for the calculation of the point spread function that is used as input for the deconvolution algorithm explained in Section 5.5.

5.4 Summary

In this section, the results of the various direct and indirect modulation transfer function measurements and their implications on the spatial system response of the imaging system are summarized.

First of all, it can be stated that the direct and indirect measurements methods can both provide valuable results for the estimation of the spatial response of the scanner. However, the feasibility of the Moiré method depends strongly on the applied analysis and is restricted to the plane where the fringes are effectively created. In contrast, the analysis of the edge profiles is less complicated, more reliable, and the edge profile measurements can be reproduced in different imaging planes. Hence, the indirect method is generally beneficial over the direct method and is recommended for future investigations with the presented setup.

The MTF of the entire imaging system can be described by a product of source MTF and detector MTF (Equ. 5.11). The absorption and scattering of the X-ray beam due to the gratings of the interferometer also contributes to the obtained system MTF, but is not considered here as an independent factor. This is due to the fact that the impact of the gratings could not be separated from the other factors, since it was impossible to dismount the entire interferometer and perform MTF measurements with no gratings in the beam. Therefore, all presented results include the contributions of the interferometer and consequently describe the typical setup for imaging applications with the scanner⁸.

The edge profile measurements in the different planes relative to the detector demonstrated that the spatial system response for practical applications is effectively characterized by the detector response only, since the impact of the source profile is negligible in the object plane.

The edge profile measurements of the wedge took place in the object plane, consequently the corresponding results characterize the spatial system response of the scanner in the plane used for normal imaging purposes. The maximal resolution that can be obtained with the scanner in the different binning modes can be estimated by the resolution measures in Table 5.8. An essential finding is that the resolution measures for the acquisition in the 2×2 binning mode are practically the same as for the acquisition without binning.

Resolution measure	Object plane no binning	Object plane 2×2 binning	Object plane 4×4 binning
10% MTF [μm]	57 ± 4	60 ± 6	–
FWHM of LSF [μm]	93 ± 6	96 ± 12	129 ± 24
FW of 10% LSF [μm]	174 ± 12	177 ± 23	238 ± 48

Table 5.8: Resolution measures for different binning modes, describing the spatial system response in the plane used for normal imaging purposes.

The resolution measures are valid regardless of the direction in the object plane, since it was demonstrated that the spatial system response of the scanner is radially symmetric.

⁸ The fact that the G₂ was dismounted for the wedge measurement is not mentioned here, since the impact of the grating on the results was negligible within the measurement accuracy, as discussed in Section 5.3.3.

As explained in Section 2.5, the response of the discussed imaging system to an input signal can be described to be linear and shift invariant. Nevertheless, the system response of the scanner might not be completely independent of the position in the object plane. The shadowing effect at the left and right margins of the field of view might influence the spatial system response in the outer regions of the FOV. Moreover, the impact of the cone beam geometry on the imaging system increases with the displacement from the center of the field of view and thus might also change the spatial system response with respect to its position. But since the impact of these effects can be considered to insignificant, the estimated maximal resolution is practically valid regardless of the exact position within the object plane.

The dependence of the spatial system response on the applied peak voltage, and thereby on the polychromatic spectrum of the X-ray beam described by an effective energy, was not explored in detail. However, general theoretical considerations and the fact that the Moiré experiment provided the same results for 35 and 45 kVp, imply that the system response can be assumed to be independent of the X-ray spectrum within the typical energy window used for imaging with the scanner.

Another important factor that might affect the resolution is the characteristics of the recorded object. The samples used here were thin, highly absorbing objects that did not cause significant scattering. If, for instance, a relatively thick sample of highly scattering material is imaged, a considerably lower maximal resolution is expected.

Please note that the given resolution measures in the results were deduced from single raw images without the phase stepping routine and thus characterize the resolution for conventional attenuation contrast images in projection mode. The impact of the phase stepping and the applied processing routine to extract the imaging signals on the final resolution of the projection images in attenuation, differential phase and dark-field contrast has not been investigated yet. Moreover, the characterization of the system response of the scanner for CT imaging requires additional factors taken into account that also contribute to the total system MTF, such as the interpolation method and the window function used during the CT reconstruction [26]. Consequently, the obtained results from the presented measurements do not describe the spatial system response expected for the typical imaging modes used with the scanner, but rather represent a solid starting point for further investigations.

In conclusion, it is important to mention that the obtained results are not only valuable to estimate the maximal resolution of the scanner; furthermore, the line spread functions from the object plane can be used to reduce the blurring in the recorded images, as explained in the following section.

5.5 Application: Deconvolution with Richardson-Lucy algorithm

In this section, a brief example for the practical applications of the obtained results from the modulation transfer function measurements is presented.

It is generally known that for a linear, shift invariant system the output signal is given by the convolution of the input signal and the impulse response (see Sec. 2.5.1). For the presented imaging system, this means that the recorded image is given by the convolution of the function describing the object and the point spread function of the system. Consequently, the object function of the sample can theoretically be recovered by deconvolution of the recorded image with the corresponding PSF. In practice, the exact determination of the object function is not feasible. Nevertheless, the deconvolution procedure can be used to improve image quality.

The practical application of the deconvolution procedure is realized by several algorithms, such as the commonly used *Wiener deconvolution* algorithm. In this example, the iterative *Richardson-Lucy* algorithm was used to pre-process raw images obtained with the scanner, prior to applying the usual processing routine to get from the raw images to the different imaging signals. The *Richardson-Lucy* algorithm is not explained here in detail, since this would go beyond the framework of this thesis. Further information about the algorithm can be found in [28, 42, 61]. The input for the algorithm is the array containing the pixel values of the recorded image and the corresponding point spread function in form of a two-dimensional array. The algorithm basically calculates iteratively the most probable pixel values for the deconvolved image by applying the maximum likelihood principle. The point spread functions used for the deconvolution of the raw images in the three binning modes were obtained by rotation of the line spread functions from the wedge experiments (Tab.5.5). This process was possible, since the spatial system response of the scanner is radially symmetric. The sizes of the resulting arrays were reduced by cutting of all pixels with negligible values to shorten the computation time of the algorithm. The size of the respective filter kernel was 9×9 pixels for the unbinned case, 3×3 pixels for the 2×2 binning, and 2×2 pixel for the 4×4 binning. Please note that the used implementation of the Richardson-Lucy algorithm is a test version and has not been optimized so far. Nevertheless, the presented results can still be used to demonstrate the basic effect of the deconvolution procedure on the processed images.

The used raw data were acquired by recording images of an ex-vivo mouse⁹ in the standard phase stepping mode of the scanner. In Figure 5.15, unbinned projection images of the torso of the mouse are shown for the three contrast modalities. In the column on the left side the attenuation contrast images are displayed, in the central column the differential phase contrast images, and in the column to the right side the dark-field images. The images in the first row were obtained from the unprocessed raw images, while the images in the following rows were obtained from raw images filtered by the deconvolution algorithm with varying numbers of iteration steps, as indicated in the figure.

⁹ The mouse was fixated in phosphor buffered saline (PBS) solution containing 3.7% formaldehyde. The thorax and the abdominal wall of the mouse were punctured to enhance the fixation process and to get rid of residual gas bubbles that produce artifacts in imaging. The mouse was left in the solution for approximately ten days, then it was washed and placed into a 50 ml Falcon tube filled with ethanol to prevent further degradation processes.

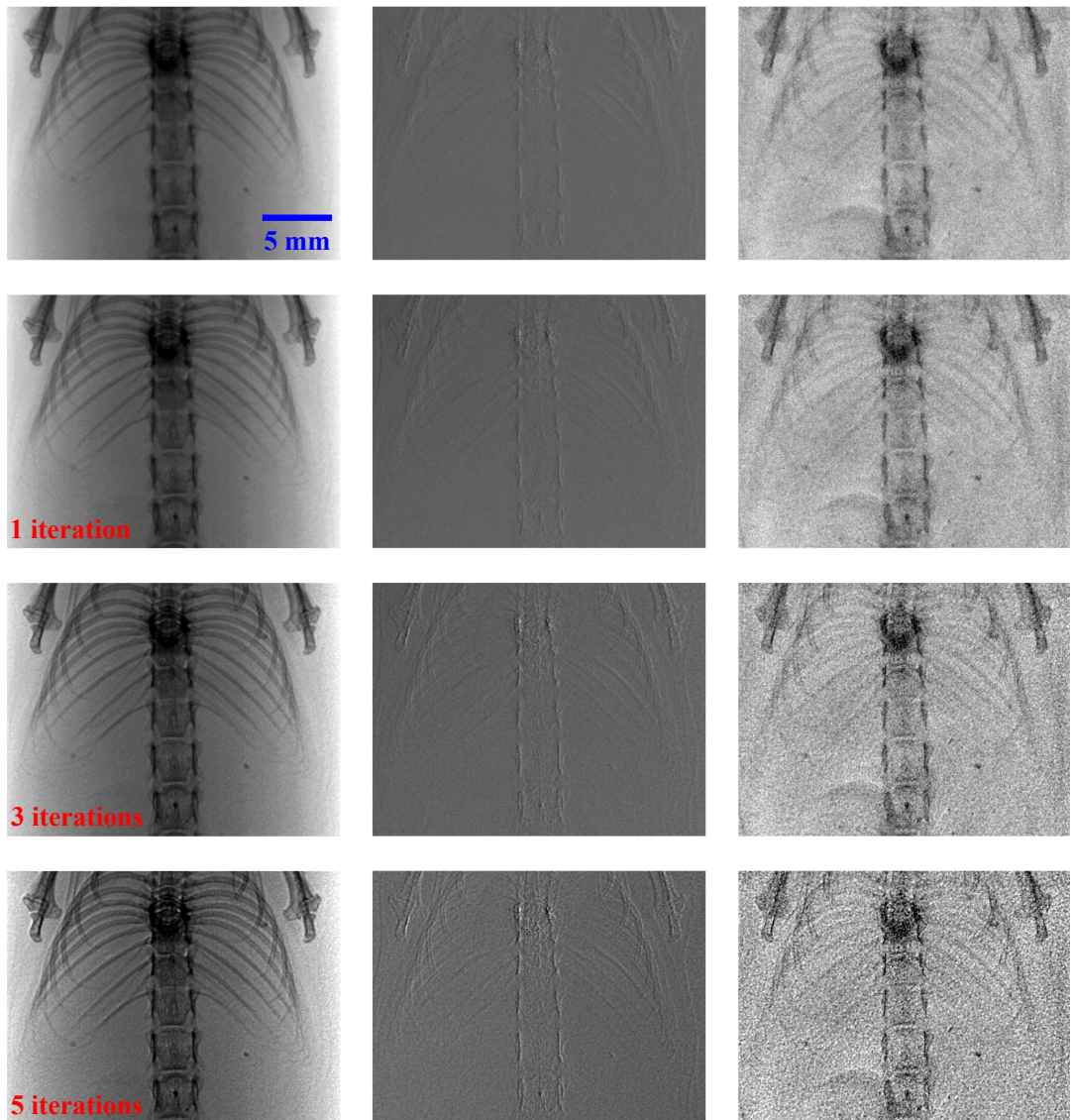


Figure 5.15: Images of the torso of a mouse in attenuation (left column), differential phase (central column), and dark-field contrast (right column) with different processing of the raw images: The first row displays images obtained from unfiltered raw data, the images displayed in the other rows, were obtained from raw images deconvolved with respectively one, three, and five iteration steps of the applied Richardson-Lucy algorithm.

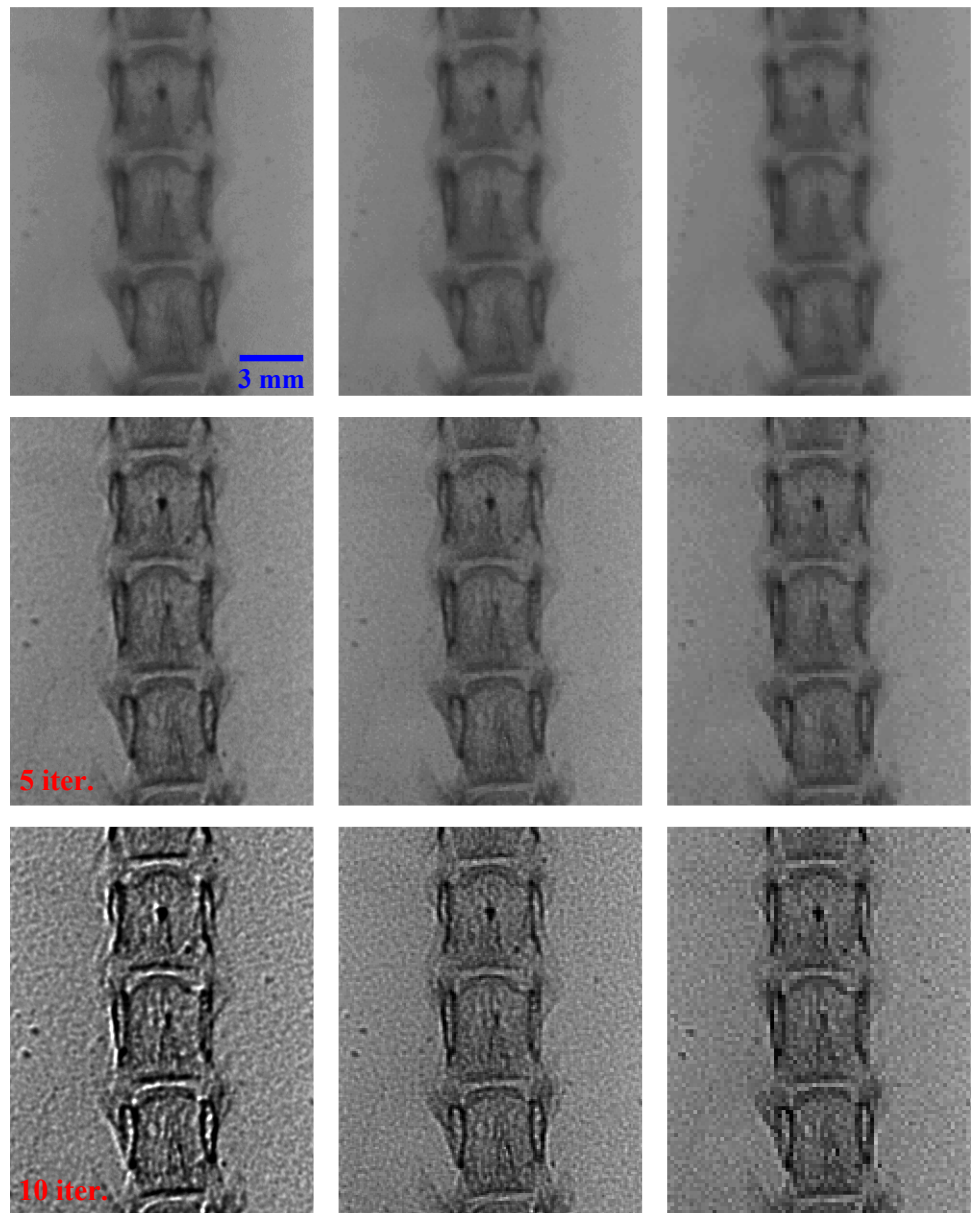


Figure 5.16: Attenuation contrast images displaying a magnified section of the spline of a mouse: The images on the left were retrieved from unbinned raw data, the central images from 2×2 binned raw data, and the images on the right from 4×4 binned raw data. The images in the first row were not processed with the deconvolution algorithm, the images in the second and third row with respectively five and ten iteration steps of the applied Richardson-Lucy algorithm.

A gradual improvement of the sharpness of the images can be observed for all contrast modalities. The images with five iterations display the structures of the sample with a perceptibly higher edge-contrast than the images from the unfiltered raw data. This can be easily seen by observing the spline of the mouse and particularly the structures of the vertebrae, which become more pronounced for a higher number of iterations. The images of Figure 5.15 also indicate that the three contrast modalities benefit to a different degree from the filtering with the deconvolution algorithm.

To demonstrate the effect of the deconvolution algorithm for the processing of binned data, the same data set was binned 2×2 and 4×4 prior to applying the deconvolution algorithm and the corresponding point spread functions for the respective binning mode were used as deconvolution kernel. In Figure 5.16, a magnified section of the spine of the mouse, based on the attenuation signal, is displayed. The images on the left were obtained without binning, the images in the center by 2×2 binning of the raw data, and the images on the right by 4×4 binning. The images in the first row were not filtered with the deconvolution algorithm, the images in the second row with five iteration steps, and the images in the third row with ten iteration steps. The image from the unbinned data filtered with ten iterations, already seems to be overregulated by the algorithm and thus is corrupted by saturation artifacts, whereas the results for the 2×2 binning and 4×4 binning raw images, filtered with ten iterations, do not show any artifacts from overregulation, which indicates that the ideal number of iteration steps depends on the binning factor.

It has to be emphasized here again that these results are premature. The quantitative effect of the applied deconvolution procedure on the images has not been analyzed yet. Moreover, the deconvolution procedure does not only improve the sharpness of the structures in an image but also amplifies the noise. Consequently, the application of this algorithm has to be considered individually for a particular set of raw images. In the case of very noisy raw images, the application of the deconvolution algorithm might even decrease the image quality. Furthermore, the results presented here indicate that the ideal number of iteration steps is different for each binning mode and contrast modality and has to be optimized separately. But since these premature results already show some improvement in the sharpness of the images, an optimized implementation of the deconvolution procedure is expected to provide a considerable benefit in achieved image quality.

6 Summary, conclusions, and outlook

In this chapter, the most important results of this thesis and the consequential conclusions for practical imaging purposes with the scanner are briefly summarized. Finally, a short outlook is presented.

The contrast-to-noise ratio analysis of attenuation and phase contrast projections and CT data from the phantom acquired with the scanner yielded the following results:

- The gain parameter of the detector had no influence on the resulting image quality in both contrast modalities.
- The image quality of the phase contrast projections was always improving when the total exposure was increased, regardless of the distribution of the total exposure among the different exposure parameters. The attenuation signal reached a certain exposure level per step where it did not benefit from higher exposure.
- For a given total exposure of a single projection and typical numbers of phase steps, the acquisition settings with less steps and higher exposure per step provided superior image quality in both contrast modalities in comparison to corresponding acquisition settings with a higher number of steps.
- For a given total exposure of an entire CT data set, the image quality of a single projection had a stronger impact on the quality of the resulting CT slices than the total number of projection angles, as long as undersampling artifacts could be ignored.
- For a given total acquisition time per projection, the phase and attenuation CNR in relation to the applied peak voltage were significantly increasing up to approximately 35 kVp. For a peak voltage range from 35 to 45 kVp, the resulting image quality in both contrast modalities was relatively similar. The best image quality in both contrasts could be achieved at approximately 45 kVp. Above 45 kVp the phase and attenuation CNRs were decreasing again.
- The best image quality for a given total exposure per CT acquisition in relation to the applied peak voltage was provided at the lowest applicable peak energy. By comparison with dose measurements of a mouse phantom, it was found that the acquisition at the lowest applicable peak energy also resulted in the lowest applied dose for an in-vivo sample.
- The contrast-to-noise ratios for both contrast modalities were increasing, the higher the applied bin factor. Consequently, the best contrast-to-noise ratios were achieved in the 4×4 binning mode.

- The piezo delay, piezo start delay, and gantry delay times implemented in the acquisition software could be reduced significantly without any loss in image quality.

The characterization of the spatial system response provided the following essential findings:

- The spatial system response of the scanner in the plane of the sample is effectively characterized by the detector response only, since the impact of the source profile can be neglected.
- The spatial resolution in the object plane is practically the same for image acquisition in 2×2 binning mode and without binning, while the maximal resolution for image acquisition in the 4×4 binning mode is considerably worse.
- The two-dimensional spatial system response is approximately radially symmetric and independent of the position in the object plane.
- The spatial system response is independent of the X-ray spectrum within the typical energy window used for imaging with the scanner.
- The filtering of the raw images of the phase stepping routine with an iterative deconvolution algorithm based on the obtained point spread functions, resulted in improved sharpness of the final images in all contrast modalities.

By considering the results of both studies, the following conclusions for practical imaging purposes with the scanner can be drawn:

- It is generally recommended to use the 2×2 binning mode for all standard imaging purposes, since it provides the best compromise between contrast-to-noise ratio and maximal resolution of the resulting images. For acquisitions with priority on the contrast-to-noise behavior of the resulting images, the 4×4 binning mode is recommended.
- For a given total acquisition time per projection image, the best image quality is achieved at approximately 45 kVp and the correspondingly maximized current of the X-ray tube. Moreover, the total exposure time per projection should be distributed among 5 phase steps and the exposure time per phase step should be maximized. The gain parameter should be chosen in such a way that over- or underexposure of the raw images is circumvented.
- In case of a given total acquisition time for a tomographic data set, the number of projection angles should be chosen to be as small as possible without causing undersampling artifacts in the reconstructed data and the exposure time per projection should be maximized. Since the acquisition time for in-vivo CT imaging with the scanner is so far limited to approximately 100 projection angles with typical exposure times per projection, the data should generally be reconstructed iteratively in order to obtain the best image quality.

-
- If image acquisition in projection or CT mode is limited by a given dose, the applied peak voltage should be as low as possible without causing underexposure of the raw images of the phase stepping. Therefore, the exposure time and the gain parameter for each of the 5 phase steps should be maximized.
 - To obtain the best image quality, regardless of exposure time and dose, the image acquisition should be performed at approximately 45 kVp and the correspondingly maximized current of the X-ray tube. The exposure time per step and the maximal number of phase steps, naturally, should be as high as possible and therefore the gain parameter should be adjusted to circumvent overexposure of the raw images.
 - The delay times should be reduced in order to enhance the acquisition speed of the scanner. This is particularly important for in-vivo CT imaging, since the animal can only be anesthetized for a certain period of time.
 - If the sharpness of the resulting images is of high importance for a particular imaging purpose, it is recommended to filter the raw images with the presented *Richardson-Lucy* algorithm prior to the standard Fourier processing routine.

It has to be mentioned here that the found conclusions are generally only valid for the phase and the attenuation signal. The behavior of the dark-field signal needs to be analyzed in further investigations. Nevertheless, basic technical findings, such as the influence of the gain and the delay parameters on the resulting image quality can be directly translated to the expected behavior for the dark-field signal.

A detailed discussion about further development and technical issues of the scanner can be found in [50]. The most important findings from the investigations of [50] are recapitulated here, complemented with additional conclusions that can be drawn from the results of this thesis.

A further improvement of the performance without modifying the hardware of the scanner may be achieved by the following approaches:

- The normalization procedure of the sample images with the reference flat-field images should be optimized for the experimental setup of the scanner in order to reduce artifacts, such as residual fringes, in the processed images and to reduce the scan time for CT acquisitions.
- Currently, the CT mode of the scanner is operated in step-and-shoot mode, meaning that the phase stepping routine and gantry rotation are performed one after the other. In the most recent software update of the acquisition software, a novel acquisition mode is implemented that combines sample rotation and phase stepping [59]. In theory, this technique reduces the applied dose and acquisition time considerably, while maintaining image quality. However, the feasibility of this method for typical imaging purposes with the scanner has not been investigated yet.

- The required number of projection angles in CT mode may be further reduced by developing advanced iterative reconstruction algorithms optimized for CT data from the scanner.
- Moreover, applying of a beam hardening correction routine to the acquired data from the scanner might also improve the resulting image quality considerably.
- Finally, the presented deconvolution procedure needs optimization to enhance the sharpness of the images more effectively.

From a technical point of view the performance of the scanner can be improved by the following optimizations:

- The scanner was designed to produce the best results at an effective energy of the X-ray spectrum of 23 keV. However, in practice, the imaging of a typical sample with the scanner requires a higher effective X-ray energy due to the limited photon flux of the tube and the efficiency of the detector. Therefore, gratings optimized for a higher design energy will increase the visibility of the scanner and thereby the contrast-to-noise ratios of the resulting images. Moreover, a reduction of the silicon wafer thickness of the gratings may reduce the acquisition time considerably and a better grating quality in terms of fewer imperfections of the grating structures will cause fewer artifacts in the processed images.
- An improvement in performance with less fundamental changes of the hardware may be achieved by the development of a faster, artifact-free acquisition mode of the incorporated detector.
- Furthermore, the optimization of the animal bed in terms of attenuation, refraction and scatter properties of the used material for the bed fabrication, might also increase the image quality.

With respect to future successor models of the phase contrast CT scanner that are based on the same physical principles, the following considerations might be valuable:

- As mentioned before, the design energy of a future scanner should be chosen to be more suitable for the required effective energies for typical imaging purposes.
- Furthermore, the spatial resolution of the current scanner is basically limited by the incorporated X-ray camera. Therefore, the spatial resolution of a future scanner may be considerably improved by using a detector that provides a higher resolution, such as a flat panel sensor with a structured CsI(Tl) scintillator.
- For CT in-vivo imaging, the acquisition speed and applied dose are the crucial factors that are limiting the image quality in terms of contrast-to-noise behavior. From this point of view, a future scanner should be equipped with a detector that is more efficient and has a lower readout noise. Moreover, a larger size of the detector pixels would

additionally increase the photon statistics and consequently the acquisition speed could be improved and the applied dose could be reduced.

- At high photon statistic, the noise in the attenuation and phase signals of the scanner is limited by the jitter of the piezo stage used for the phase stepping. Consequently, the stability of the piezo stage might also be an important factor for a future scanner that provides better photon statistics.

Concluding, it can be said that the presented phase contrast CT scanner represents an important step towards clinical implementation of grating-based X-ray phase contrast imaging. In this thesis, crucial properties of the scanner have been investigated and valuable conclusions for future applications have been drawn.

A CNR analysis

A.1 Projection data

A.1.1 MATLAB processing script

All projection images for the CNR analysis were processed with the same processing script and the same settings. The AMP and DPC signals were extracted by Fourier analysis from the intensity curves obtained from the phase stepping procedure, as explained in Section 2.2.3. The AMP and DPC signal were extracted from images of the sample and from the reference images. The resulting relative signals are given by:

$$a_0 = \frac{a_0^s}{a_0^r}, \quad (\text{A.1})$$

$$\phi_1 = \phi_1^s - \phi_1^r. \quad (\text{A.2})$$

An adaptive differential phase recovery method (ADPR) was implemented in the processing script to correct for phase artifacts that are caused by minute changes of the grating alignments during the acquisitions. More detailed information about the phase recovery method can be found in [52]. The gray value range of the resulting 16-bit *TIFF* images was set to the maximal signal range for both contrast modalities:

$$\text{AMP}_{\min} = 0; \quad \text{AMP}_{\max} = 1.1; \quad (\text{A.3})$$

$$\text{DPC}_{\min} = -\pi; \quad \text{DPC}_{\max} = \pi. \quad (\text{A.4})$$

A.1.2 CNR versus gain: Acquisition parameters

In this section, the acquisition parameters for the projection images used to calculate the averaged gain results (Fig. 4.10) are displayed. Please note that the Skyscan acquisition software *Version 2* and the old G₂ grating were used for all listed acquisitions.

Peak Voltage [kVp]	Current [μ A]	Steps	Exposure time [s]	Gain [%]
33	472	10	10	20
33	472	10	10	40
33	472	10	10	60
33	472	10	10	80
33	472	10	10	100
36	540	10	5	20
36	540	10	5	40
36	540	10	5	60
36	540	10	5	80
36	540	10	5	100
39	592	10	3.3	20
39	592	10	3.3	40
39	592	10	3.3	60
39	592	10	3.3	80
39	592	10	3.3	100
42	644	10	2	20
42	644	10	2	40
42	644	10	2	60
42	644	10	2	80
42	644	10	2	100
48	756	10	1	20
48	756	10	1	40
48	756	10	1	60

Table A.1: List of acquisition parameters for the CNR comparison with varying gain factors.

A.1.3 CNR versus exposure time per step: Acquisition parameters

In this section, the acquisition parameters for the projection images used to obtain the results in Figure 4.11 and Figure 4.12. Please note that the Skyscan acquisition software *Version 2* and the old G₂ grating were used for all listed acquisitions.

Peak Voltage [kVp]	Current [μ A]	Steps	Exposure time [s]	Gain [%]
36	540	10	2	40
36	540	10	3.3	40
36	540	10	5	20
36	540	10	10	20
45	712	10	0.3	100
45	712	10	0.5	60
45	712	10	1	100
45	712	10	2	80
45	712	10	3.3	20
45	712	10	2	20

Table A.2: List of acquisition parameters for the CNR comparison with varying exposure times per step.

A.1.4 Exposure time per phase step versus number of phase steps: Acquisition parameters

In this section, the acquisition parameters for the comparison of projection images with same total exposure, but varying number of steps are listed (Tab. 4.1). The compared settings are indicated by the values in brackets for the processing with 5 steps. Please note that the Skyscan acquisition software *Version 2* and the old G₂ grating were used for all listed acquisitions.

Peak Voltage [kVp]	Current [μ A]	Steps	Exposure time [s]	Gain [%]
39	540	10 (5)	1 (2)	60
42	644	10 (5)	1 (2)	60
45	712	10 (5)	1 (2)	60
36	540	10 (5)	5 (10)	20
39	592	10 (5)	5 (10)	20
42	644	10 (5)	5 (10)	20
33	472	10 (5)	5 (10)	40
33	472	10 (5)	5 (10)	60
33	472	10 (5)	5 (10)	80
33	472	10 (5)	5 (10)	100
48	756	10 (5)	0.5 (1)	60
48	756	10 (5)	0.5 (1)	80
48	756	10 (5)	0.5 (1)	100
45	712	10 (5)	0.5 (1)	80
45	712	10 (5)	1 (2)	80

Table A.3: List of acquisition parameters for the CNR comparison with same total exposure and different numbers of steps.

A.1.5 Maximal CNR versus peak voltage: Acquisition parameters

In Table A.4, the acquisition parameters are given for the acquisitions used to present the maximal contrast parameter (Fig. 4.15) and maximal CNR (Fig. 4.16) for a given peak voltage. Please note that the Skyscan acquisition software *Version 2* and the old G₂ grating were used for all listed acquisitions.

Peak Voltage [kVp]	Current [μ A]	Steps	Exposure time [s]	Gain [%]
27	336	10	10	80
30	404	10	10	80
33	468	10	10	100
36	540	10	10	100
39	604	10	10	20
42	656	10	10	20
45	720	10	5	20
48	764	10	5	20

Table A.4: List of acquisition parameters for the comparison of the contrast parameter and the maximal CNR with varying peak voltages.

A.1.6 CNR versus peak voltage with the new G₂ grating: Acquisition parameters and supplementary results

In Table A.5, the acquisition parameters are listed for the acquisitions with the new G₂ grating, which has a gold height of 45 μm . Please note that the Skyscan acquisition software *Version 1* was used for all listed acquisitions.

Parts of this results are displayed in Figure 4.17 in the results section. The remaining results from the acquisitions with the new G₂ grating are depicted in Figure A.3 and Figure A.2. Both figures show normalized CNR in relation to the applied number of phase steps. Please note that the exposure time per step was 2 s in Figure A.3 and 10 s in Figure A.2.

Peak Voltage [kVp]	Current [μA]	Steps	Exposure time [s]	Gain [%]
33	476	10	3.3	100
36	532	10	3.3	100
39	604	10	3.3	60
42	648	10	3.3	40
45	720	10	3.3	20
48	764	10	3.3	20
42	652	4	2	60
42	652	6	2	60
42	652	8	2	60
42	652	10	2	60
42	652	4	10	20
42	652	6	10	20
42	652	8	10	20
42	652	10	10	20

Table A.5: List of acquisition parameters for the acquisitions with the new G₂ grating.

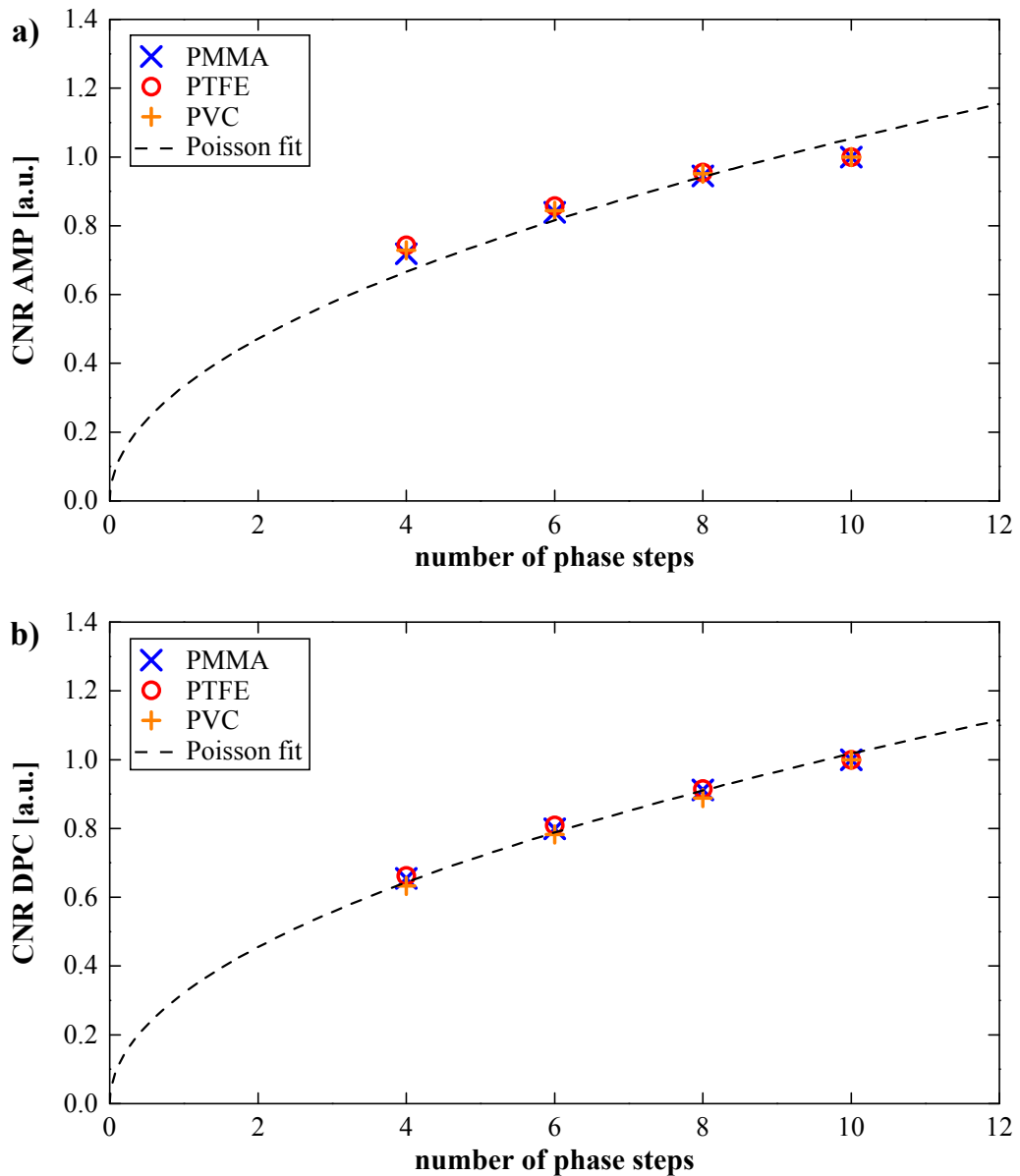


Figure A.1: CNR vs. number of phase steps in projection mode with 2 s exposure time per step. **a)** AMP CNR. **b)** DPC CNR. The projections were acquired at 42 kVp. The dashed lines represent a square root function fitted to all data points of the respective plot. The displayed results are normalized relative to the maximum value of the respective rod.

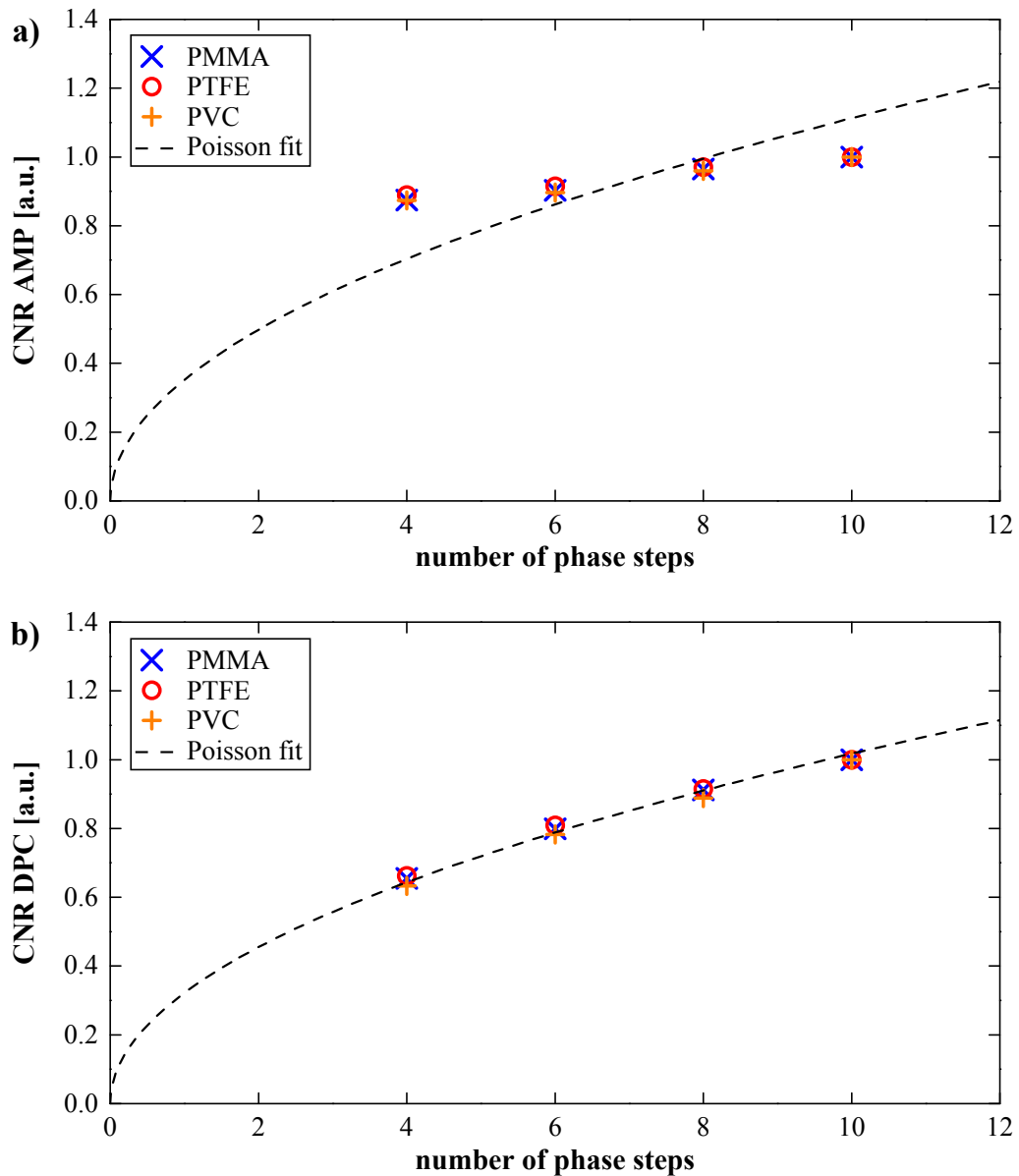


Figure A.2: CNR vs. number of phase steps in projection mode with 10 s exposure time per step. **a)** AMP CNR. **b)** DPC CNR. The projections were acquired at 42 kVp. The dashed lines represent a square root function fitted to all data points of the respective plot. The displayed results are normalized relative to the maximum value of the respective rod.

A.1.7 CNR versus binning: Acquisition parameters

In this section the acquisition parameters for the projection images used to calculate the ratios (Tab. 4.3) of the results with different binning modes are listed. Please note that the Skyscan acquisition software *Version 2* and the old G₂ were used for all listed acquisitions.

Peak Voltage [kVp]	Current [μ A]	Steps	Exposure time [s]	Gain [%]
36	532	10	2	80
39	540	10	2	60
42	644	10	2	60
45	712	10	2	60
33	476	10	10	20
36	540	10	10	20
39	592	10	10	20
42	644	10	10	20
48	756	10	1	20
48	756	10	1	40
48	756	10	1	60
48	756	10	1	80
48	756	10	1	100
45	712	10	0.3	100
45	712	10	0.5	80
45	712	10	1	80

Table A.6: List of acquisition parameters for the comparison of the CNRs in different binning modes.

A.1.8 CNR versus delay parameters: Acquisition parameters

In Table A.7 the acquisition parameters are listed for the acquisitions with the different piezo delay and piezo start delay times. Please note that the Skyscan acquisition software *Version 3* and the new G₂ grating were used for all listed acquisitions.

Peak Voltage [kVp]	Current [μA]	Steps	Exposure time [s]	Gain [%]	Piezo delay [ms]	Piezo start delay [ms]
42	700	5	1	8	1000	5000
42	700	5	1	8	800	5000
42	700	5	1	8	600	5000
42	700	5	1	8	400	5000
42	700	5	1	8	300	5000
42	700	5	1	8	200	5000
42	700	5	1	8	100	5000
42	700	5	1	8	1000	5000
42	700	5	1	8	1000	4000
42	700	5	1	8	1000	3000
42	700	5	1	8	1000	2000
42	700	5	1	8	1000	1000
42	700	5	1	8	1000	500

Table A.7: List of acquisition parameters for the comparison of the CNRs with varying delay parameters.

A.2 CT data

A.2.1 Processing and reconstruction

The projection images of the CT data sets were processed with the same script and settings as the single projections, except for the fact that no separate flat-field image was acquired for each projection angle. Instead, for each interval of typically 20 projections, a block of 10 flat-field images with static gantry were acquired and each projection in the interval was normalized with a randomly chosen flat-field from this block.

The CT slices were reconstructed with a Skyscan reconstruction software optimized for the cone beam setup of the scanner. For the reconstruction of the attenuation signal a *Hamming* filter was used during the *Filtered Backprojection*. For the phase signal a *Hilbert* filter was used during the FBP in order to reconstruct the phase contrast, instead of the differential phase contrast. The gray value range was the same for all reconstructions and was found by determining the maximal and minimal values of the acquisition at the lowest energy:

$$\text{attenuation}_{\min} = -0.02; \quad \text{attenuation}_{\max} = 0.07; \quad (\text{A.5})$$

$$\text{phase shift}_{\min} = -0.01; \quad \text{phase shift}_{\max} = 0.05. \quad (\text{A.6})$$

No beam hardening or ring artifact correction was applied during the reconstruction.

A.2.2 List of acquisition parameters for all CT data sets

In Table A.8 the relevant acquisition parameters of all acquired CT data sets for the CNR analysis are presented. All CT data were acquired with the Skyscan software *Version 1* and the old G₂ (25 μ m). For all delay times the default values were used if not mentioned explicitly (gantry delay: 1000 ms, piezo delay: 1000ms, piezo start delay: 5000 ms) .

Acquisition	Peak Voltage [kVp]	Current [μ A]	Steps	Exposure time [s]	Gain [%]	FF/proj	Proj
32 kVp	32	516	6	10	50	10/20	1001
35 kVp	35	532	6	10	50	10/20	1001
39 kVp	39	604	6	3.3	50	10/20	1001
45 kVp	45	712	6	2	50	10/20	1001
5 steps	45	712	5	2	50	10/20	1001
4 steps	45	712	4	2	50	10/20	1001
3 steps	45	712	3	2	50	10/20	1001
Gantry delay 500 ms	45	712	6	2	50	10/20	1001
Gantry delay 100 ms	45	712	6	2	50	10/20	1001
Low dose	45	712	6	0.5	50	10/20	1001
Fixation	44	704	6	2	50	10/20	1001

Table A.8: List of acquisition parameters for all CT data sets.

A.2.3 Supplementary results: Low dose and alternative fixation

In Table A.9, two additional acquisitions are compared to the reference measurement at 45 kVp. The exact acquisition parameters can be found in Table A.8. For the low dose measurement the lowest exposure time per step was applied that still did not lead to underexposure of the detector. However, from a retrospective view the acquisition parameters for a low dose measurement should be chosen differently (see Section 4.3.3) and therefore this result does not have any practical significance.

For the acquisition named "Fixation" the Falcon tube was fixated in a different way as for the other acquisitions: Usually the plastic container was fixated with a cable strap to the animal bed in such a way that the cable strap did not interfere with the movement of the positioning stage when the sample is moved from the zero position (for flat-field acquisition) to the actual position in the FOV. For the Fixation measurement, the cable strap was attached in such a way that it wobbled over the roles of the position stage for each movement of the stage and therefore the exact sample position might be changed slightly after each flat-field acquisition. The results show the impact of the alternative fixation method compared to the standard fixation.

Contrast modality	Material	Low dose	Fixation	Reference measurement at 45 kVp
Attenuation CT	PMMA	4.68	11.11	11.20
	PTFE	9.05	21.53	22.00
	PVC	15.27	35.77	37.38
Phase CT	PMMA	7.16	17.98	19.62
	PTFE	10.31	24.89	26.66
	PVC	3.97	12.34	12.99

Table A.9: CNR results for supplementary CT measurements.

A.3 Literature data of the phantom materials

In this section, the literature values of the linear attenuation coefficient μ and the decrement of the real part of the complex refractive index δ for the different rod materials are given. The literature data were taken from the *XOP data base* provided by the European Synchrotron Radiation Facility (ESRF), Grenoble, France.

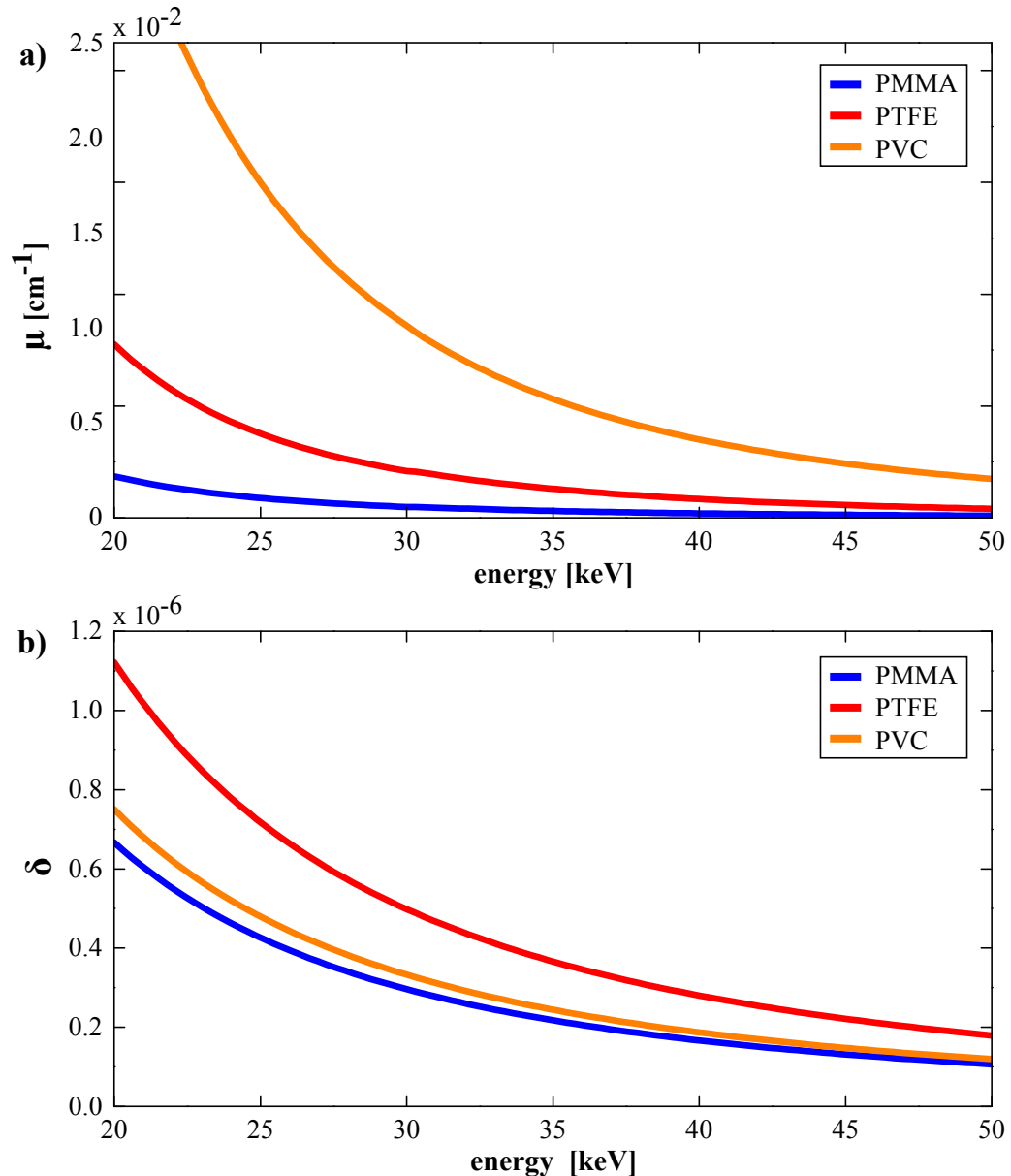


Figure A.3: Literature data of the phantom materials. a) Linear attenuation coefficient μ . b) Decrement of the real part of the complex refractive index δ .

Acknowledgments

While there is always only a single author on the front cover of a Diploma thesis, this work would not have been possible without the contribution, advice and guidance of many people.

First of all, I would like to express my gratitude to Franz Pfeiffer for his intriguing lecture on biomedical physics, which draw my attention to this interesting field of research, and for giving me the opportunity to be a part of his group. Furthermore, I want to thank him for the guidance and very helpful advices he provided during the last year.

My sincere gratitude also belongs to the other members of the "*Skyscan-team*":

To Martin Bech, for his patience and helpfulness during numerous discussions over the last year and for all the invaluable advices he gave me. Moreover, for his comments on the structure of this work and for proofreading my thesis.

To Andre Yaroshenko, for his continuous support in daily work with the scanner and his helpful feedback on many aspects of this work. Furthermore, for providing me with a very interesting insight into the field of in-vivo X-ray imaging with small animals and for proofreading this thesis.

To Astrid Velroyen, for helping me with all kinds of problems whenever I needed support. I also want to thank her for proofreading this thesis and for all the discussions and advices related to programming and data processing issues, in particular for the help with the implementation of the deconvolution algorithm.

To Arne Tapfer, for introducing me to the phase contrast scanner in the first place, for sharing his invaluable knowledge about the scanner with me, and for giving me helpful comments on several aspects of this work.

Furthermore, I would like to thank Bart Pauwels and Faisal Nadeem from our industrial collaboration partner *Bruker microCT* for their friendly support and for patiently answering all my questions related to the hardware and the acquisition software of the scanner.

I would like to express my sincere thanks to Andreas Malecki and Martin Dierolf for their permanent support with all kinds of IT related issues.

Equally, I would like to thank Michael Chabior for his critical comments and suggestions with respect to crucial aspects of this thesis.

Moreover, I would like to thank Hans Märucz for building the X-ray phantom that has been used during this work.

A special thank you goes the IMETUM crew of the E17 group for providing such a pleasant and friendly working atmosphere and for any kind of help during the last year.

I also want to thank the whole E17 group for creating such an enjoyable and comfortable atmosphere as well as for the incredible amount of cakes.

Finally, I want to express my sincere gratitude to my family and friends. To my mum and dad, for supporting me during my whole life with both financial and moral assistance and for always trusting in me, especially throughout difficult times. To my brothers and friends, for always being there for me.

Bibliography

- [1] ALS-NIELSEN, J., AND McMORROW, D. *Elements of Modern X-ray Physics*. Wiley and Sons, 2011.
- [2] BECH, M. *X-ray imaging with a grating interferometer*. PhD thesis, 2009.
- [3] BECH, M., JENSEN, T. H., FEIDENHANS'L, R., BUNK, O., DAVID, C., AND PFEIFFER, F. Soft-tissue phase-contrast tomography with an x-ray tube source. *Physics in Medicine and Biology* 54, 9 (2009), 2747.
- [4] BECH, M., TAPFER, A., VELROYEN, A., YAROSHENKO, A., PAUWELS, B., HOSTENS, J., BRUYNDONCKX, P., SASOV, A., AND PFEIFFER, F. Phase-contrast x-ray imaging translates to in-vivo mouse models. 2013 (submitted).
- [5] BLUSHBERG, J. T. *The Essential Physics of Medical Imaging*. Lippincott Williams and Wilkins, 2002.
- [6] BONSE, U., AND HART, M. An x-ray interferometer. *Applied Physics Letters* 6, 8 (1965), 155–156.
- [7] BOREMAN, G. D. *Modulation Transfer Function in Optical and Electro-optical Systems*. SPIE Press, 2001.
- [8] CHABIOR, M. *Contributions to the characterization of grating-based x-ray phase-contrast imaging*. PhD thesis, 2011.
- [9] CHABIOR, M., DONATH, T., DAVID, C., SCHUSTER, M., SCHROER, C., AND PFEIFFER, F. Signal-to-noise ratio in x-ray dark-field imaging using a grating interferometer. *Journal of Applied Physics* 110, 5 (2011).
- [10] CHEN, G.-H., ZAMBELLI, J., LI, K., BEVINS, N., AND QI, Z. Scaling law for noise variance and spatial resolution in differential phase contrast computed tomography. *Medical Physics* 38, 2 (2011), 584–588.
- [11] CLOETENS, P., PATEYRON-SALOME, M., BUFFIERE, J. Y., PEIX, G., BARUCHEL, J., PEYRIN, F., AND SCHLENKER, M. Observation of microstructure and damage in materials by phase sensitive radiography and tomography. *Journal of Applied Physics* 81, 9 (1997), 5878–5886.
- [12] DAVID, C., NOHAMMER, B., SOLAK, H. H., AND ZIEGLER, E. Differential x-ray phase contrast imaging using a shearing interferometer. *Applied Physics Letters* 81, 17 (2002), 3287–3289.

- [13] DAVIS, T., GAO, D., GUREYEV, T., STEVENSON, A., AND WILKINS, S. W. Phase-contrast imaging of weakly absorbing materials using hard x-rays. *Nature* 373, 6515 (1995), 595–598.
- [14] DONATH, T. *Quantitative X-ray Microtomography with Synchrotron Radiation*. PhD thesis, 2007.
- [15] ENGELHARDT, M., BAUMANN, J., SCHUSTER, M., KOTTLER, C., PFEIFFER, F., BUNK, O., AND DAVID, C. High-resolution differential phase contrast imaging using a magnifying projection geometry with a microfocus x-ray source. *Applied Physics Letters* 90, 22 (2007), 224101.
- [16] GASKILL, J. *Linear Systems, Fourier Transforms, and Optics*. Wiley and Sons, 1978.
- [17] GRANDL, S., WILLNER, M., HERZEN, J., MAYR, D., AUWETER, S. D., HIPP, A., PFEIFFER, F., REISER, M., AND HELLERHOFF, K. Evaluation of phase-contrast ct of breast tissue at conventional x-ray sources - presentation of selected findings. *Zeitschrift für Medizinische Physik* 23, 3 (2013), 212 – 221.
- [18] HAMAMATSU. *Data sheet: Flat panel sensor C9312SK-06*.
- [19] HAMAMATSU. *Opto-semiconductor handbook, Chapter 8: X-ray detectors*.
- [20] HERMAN., G. T. *Fundamentals of Computerized Tomography: Image Reconstruction from Projections*. Springer, 2009.
- [21] HERMWILLE, M. Moiré interferometry at compact x-ray synchrotron sources. Master's thesis, 2013.
- [22] HUFNAGEL, R. E. Significance of the phase of optical transfer functions. *Jorunal of the Optical Society of America* 58, 11 (1968), 1505–1506.
- [23] INGAL, V., AND BELIAESKAYA, E. X-ray plane-wave topography observation of the phase-contrast from a noncrystalline object. *Journal of Phyisc D: Applied Physics* 28, 11 (1995), 2314–2317.
- [24] KENNTNER, J., ALTAPOVA, V., GRUND, T., PANTENBURG, F. J., MEISER, J., BAUMBACH, T., AND MOHR, J. Fabrication and characterization of analyzer gratings with high aspect ratios for phase contrast imaging using a talbot interferometer. *AIP Conference Proceedings* 1437, 1 (2012), 89–93.
- [25] LEMPICKI, A., WOJTOWICZ, A., AND BERMAN, E. Fundamental limits of scintillator performance. *Nuclear Instruments and Methods in Physics Research Section A: Accelerators, Spectrometers, Detectors and Associated Equipment* 333, 2-3 (1993), 304 – 311.
- [26] LI, K., ZAMBELLI, J., BEVINS, N., GE, Y., AND CHEN, G.-H. Spatial resolution characterization of differential phase contrast ct systems via modulation transfer function (mtf) measurements. *Physics in Medicine and Biology* 58, 12 (2013), 4119.

- [27] LOHMANN, A. W., AND THOMAS, J. A. Making an array illuminator based on the talbot effect. *Applied Optics* 29, 29 (1990), 4337–4340.
- [28] LUCY, L. Iterative technique for rectification of observed distributions. *Astronomical journal* 79, 6 (1974), 745–754.
- [29] MARSCHNER, M. Data processing in grating-based x-ray phase-contrast computed tomography: workflow automation and noise studies. Master's thesis, 2013.
- [30] MEINEL, F. G., YAROSHENKO, A., HELLBACH, K., BECH, M., MÜLLER, M., VELROYEN, A., BAMBERG, F., EICKELBERG, O., NIKOLAOU, K., REISER, M. F., PFEIFFER, F., AND YILDIRIM, A. O. In vivo visualization of pulmonary emphysema using dark-field radiography. 2013 (in progress).
- [31] MOMOSE, A. Demonstration of phase-contrast x-ray computed tomography using an x-ray interferometer. *Nuclear Instruments and Methods in Physics Research Section A: Accelerators, Spectrometers, Detectors and Associated Equipment* 352, 3 (1995), 622 – 628.
- [32] PFEIFFER, F., BECH, M., BUNK, O., KRAFT, P., EIKENBERRY, E. F., BRONNIMANN, C., GRÜNZWEIG, C., AND DAVID, C. Hard-x-ray dark-field imaging using a grating interferometer. *Nature Materials* 7, 2 (2008), 134–137.
- [33] PFEIFFER, F., KOTTLER, C., BUNK, O., AND DAVID, C. Hard x-ray phase tomography with low-brilliance sources. *Phys. Rev. Lett.* 98 (2007), 108105.
- [34] PFEIFFER, F., WEITKAMP, T., BUNK, O., AND DAVID, C. Phase retrieval and differential phase-contrast imaging with low-brilliance x-ray sources. *Nature Physics* 2, 4 (2006), 258–261.
- [35] PI. Catalogue: *Piezo-driven nanopositioning and scanning systems*.
- [36] PI. Datasheet: *P-712 Low-Profile Piezo Scanner*.
- [37] PRESS, W. H., TEUKOLSKY, S. A., VETTERLING, W. T., AND FLANNERY, B. P. *Numerical Recipes: The Art of Scientific Computing*, 3rd ed. Cambridge University Press, 2007.
- [38] RADON, J. *Über die Bestimmung von Funktionen durch ihre Integralwerte längs gewisser Mannigfaltigkeiten*. Ber. Ver. Saechs. Akad. Wiss. Leipzig, Math-Phys. Kl Vol. 69, (1917).
- [39] RAUPACH, R., AND FLOHR, T. G. Analytical evaluation of the signal and noise propagation in x-ray differential phase-contrast computed tomography. *Physics in Medicine and Biology* 56, 7 (2011), 2219.
- [40] REVOL, V., KOTTLER, C., KAUFMANN, R., STRAUMANN, U., AND URBAN, C. Noise analysis of grating-based x-ray differential phase contrast imaging. *Review of Scientific Instruments* 81, 7 (2010), 073709.

- [41] REZNIKOVA, E., MOHR, J., BOERNER, M., NAZMOV, V., AND JAKOBS, P.-J. Soft x-ray lithography of high aspect ratio su8 submicron structures. *Microsystem Technologies* 14, 9-11 (2008), 1683–1688.
- [42] RICHARDSON, W. H. Bayesian-based iterative method of image restoration. *Jorunal of the Optical Society of America* 62, 1 (1972), 55–59.
- [43] ROENTGEN, W. C. On a new kind of rays. *Nature* 53, 1396 (1896), 274–276.
- [44] RTW. *Datasheet of metal-ceramic X-ray tube: RTW, MCBM 65B-50 W.*
- [45] SCHAFF, F. Numerical analysis of microct and x-ray vector radiography data from trabecular bones. Master's thesis, 2013.
- [46] SLANEY, M., AND KAK, A. *Principles of computerized tomographic imaging*. Society for Industrial and Applied Mathematics, 2001.
- [47] SNIGIREV, A., SNIGIREVA, I., KOHN, V., KUZNETSOV, S., AND SCHELOKOV, I. On the possibilities of x-ray phase contrast micro-imaging by coherent high-energy synchrotron radiation. *Review of Scientific Instruments* 66, 12 (1995), 5486–5492.
- [48] SULESKI, T. J. Generation of lohmann images from binary-phase talbot array illuminators. *Applied Optics* 36, 20 (1997), 4686–4691.
- [49] TALBOT, H. F. Lxxvi. facts relating to optical science. no. iv. *Philosophical Magazine Series 3* 9, 56 (1836), 401–407.
- [50] TAPFER, A. *Small Animal X-ray Phase-Contrast Imaging*. PhD thesis, 2013.
- [51] TAPFER, A., BECH, M., PAUWELS, B., LIU, X., BRUYNDONCKX, P., SASOV, A., KENNTNER, J., MOHR, J., WALTER, M., SCHULZ, J., AND PFEIFFER, F. Development of a prototype gantry system for preclinical x-ray phase-contrast computed tomography. *Medical Physics* 38, 11 (2011), 5910–5915.
- [52] TAPFER, A., BECH, M., VELROYEN, A., MEISER, J., MOHR, J., WALTER, M., SCHULZ, J., PAUWELS, B., BRUYNDONCKX, P., LIU, X., SASOV, A., AND PFEIFFER, F. Experimental results from a preclinical x-ray phase-contrast ct scanner. *Proceedings of the National Academy of Sciences* 109, 39 (2012), 15691–15696.
- [53] WEITKAMP, T., DIAZ, A., DAVID, C., PFEIFFER, F., STAMPANONI, M., CLOETENS, P., AND ZIEGLER, E. X-ray phase imaging with a grating interferometer. *Optics Express* 13, 16 (2005), 6296–6304.
- [54] WEITKAMP, T., DIAZ, A., NOHAMMER, B., PFEIFFER, F., STAMPANONI, M., ZIEGLER, E., AND DAVID, C. Moiré interferometry formulas for hard x-ray wave-front sensing. *Proceedings of SPIE* 5533 (2004), 140–144.
- [55] WILLIAMS, C. S., AND BECKLUND, O. A. *Introduction to Optical Transfer Function*. SPIE Press, 2002.

- [56] WILLMOTT, P. *An Introduction to Synchrotron Radiation*. Wiley and Sons, 2012.
- [57] WILLNER, M., BECH, M., HERZEN, J., ZANETTE, I., HAHN, D., KENNTNER, J., MOHR, J., RACK, A., WEITKAMP, T., AND PFEIFFER, F. Quantitative x-ray phase-contrast computed tomography at 82 kev. *Optics Express* 21, 4 (2013), 4155–4166.
- [58] YAROSHENKO, A., MEINEL, F. G., BECH, M., TAPFER, A., VELROYEN, A., SCHLEEDE, S., AUWETER, S., BOHLA, A., YILDIRIM, A. O., NIKOLAOU, K., BAMBERG, F., EICKELBERG, O., REISER, M. F., AND PFEIFFER, F. Pulmonary emphysema diagnosis with a preclinical small-animal x-ray dark-field scatter-contrast scanner. *Radiology* 122413 (2013).
- [59] ZANETTE, I., BECH, M., RACK, A., LE DUC, G., TAFFOREAU, P., DAVID, C., MOHR, J., PFEIFFER, F., AND WEITKAMP, T. Trimodal low-dose x-ray tomography. *Proceedings of the National Academy of Sciences* (2012).
- [60] ZANETTE, I., WEITKAMP, T., LANG, S., LANGER, M., MOHR, J., DAVID, C., AND BARUCHEL, J. Quantitative phase and absorption tomography with an x-ray grating interferometer and synchrotron radiation. *physica status solidi (a)* 208, 11 (2011), 2526–2532.
- [61] ZECH, G. Iterative unfolding with the richardson-lucy algorithm. *Nuclear Instruments and Methods in Physics Research Section A: Accelerators, Spectrometers, Detectors and Associated Equipment* 716, 0 (2013), 1 – 9.
- [62] ZERNIKE, F. Phase contrast, a new method for the microscopic observation of transparent objects. *Physica* 9, 7 (1942), 686 – 698.

List of Abbreviations

AMP	attenuation contrast
CNR	contrast-to-noise ratio
CT	Computed Tomography
DCI	dark-field contrast
DPC	differential phase contrast
ESF	edge spread function
FBP	Filtered Backprojection
FFT	Fast Fourier Transform
FOV	field of view
FW 10%	resolution measure based on full width at 10% of the respective LSF.
FWHM	full width at half maximum, in this thesis: Resolution measure based on FWHM of the respective LSF.
iFFT	inverse Fast Fourier Transform
kVp	peak voltage in kilovolt
lp	line pairs
LSF	line spread function
LSI	linear and shift invariant system
MTF	modulation transfer function
MTF 10%	resolution measure based on the spatial frequency, at which the MTF of the systems falls below 10%.
OTF	optical transfer function
PEA	piezoelectric actuator
PMMA	polymethylmethacrylate

PSF	point spread function
PTF	phase transfer function
PTFE	polytetrafluoroethylene
PVC	polyvinyl chloride
RMSE	root-mean-square error
ROI	region of interest
SE	standard error
SNR	signal-to-noise ratio

List of Figures

2.1	Attenuation and phase shift of an electromagnetic wave propagating in a medium	4
2.2	Schematic drawing of a Talbot-Lau interferometer	7
2.3	Phase stepping procedure and resulting contrast modalities	9
2.4	Radon Transform: Line integral	10
2.5	Visualization of the Radon Transform: Sinogram	11
2.6	Visualization of the Fourier Slice Theorem	12
2.7	Resolution measures	16
3.1	Photograph of small animal phase contrast CT scanner and control PC	17
3.2	Small animal phase contrast CT scanner: Technical drawings and photographs	19
3.3	Schematic drawing of the experimental setup including distances between the individual components	21
4.1	Photographs of the phantom	24
4.2	Attenuation signal from the phantom	26
4.3	Differential phase signal from the phantom	27
4.4	Schematic drawing of attenuation and differential phase contrast signal for a circular object with radius R and constant refractive index n	28
4.5	Fitting of the obtained analytical functions to the attenuation and differential phase signals from the Falcon tube	29
4.6	Comparison of the original signals and the isolated signals from the three rods	30
4.7	Fitting of the obtained analytical functions to the attenuation signal from the rods	32
4.8	Fitting of the obtained analytical functions to the differential phase signal from the rods	34
4.9	Reconstructed transverse CT slices with regions of interest used for the CNR analysis.	36
4.10	CNR vs. gain in projection mode	39
4.11	CNR vs. exposure time per phase step in projection mode at 36 kVp	42
4.12	CNR vs. exposure time per phase step in projection mode at 45 kVp	43
4.13	CNR vs. number of projection angles in CT mode	46
4.14	CNR vs. number of phase steps in CT mode	47
4.15	Contrast parameter from projection analysis vs. peak voltage	53
4.16	Maximal CNR vs. peak voltage in projection mode	54
4.17	CNR vs. peak voltage at constant exposure time in projection mode	55

4.18	CNR vs. peak voltage at constant total exposure in CT mode	57
4.19	CNR vs. piezo delay in projection mode	64
4.20	CNR vs. piezo start delay in projection mode	65
5.1	Moiré pattern and corresponding line profile	70
5.2	Fourier representation of Moiré pattern	71
5.3	Sketch to illustrate the relationship of a sinusoidal pattern and the corresponding frequency spectrum	73
5.4	Scheme of data processing for the direct MTF measurements	76
5.5	ESF measurements at the edges of the G ₂ grating	78
5.6	Normalization of the image of the wedge in the object plane: Part I	80
5.7	Normalization of the image of the wedge in the object plane: Part II	81
5.8	Influence of beam direction relative to the alignment of the wedge on resulting edge profile	82
5.9	Scheme of data processing for the edge profile measurements	85
5.10	Results of the Moiré measurement at 45 kVp	87
5.11	Results of the edge profile measurements in pixel	92
5.12	Results of the edge profile measurements in mm	93
5.13	Comparison of the results for the edge profile measurements at the G ₂ edges and the Moiré measurements	97
5.14	Comparison of the results from the wedge experiment in the object plane with different binning settings	99
5.15	Comparison of filtered and unfiltered images of the torso of a mouse in the three contrast modalities	106
5.16	Comparison of filtered and unfiltered AMP images of the spline of a mouse .	107
A.1	CNR vs. number of phase steps in projection mode with 2 s exposure time per step	121
A.2	CNR vs. number of phase steps in projection mode with 10 s exposure time per step	122
A.3	Literature data of the phantom materials	128

List of Tables

3.1	Mean visibilities in relation to the applied peak voltage for different G ₂ gratings	20
4.1	Comparison of CNR for the same total exposure but varying numbers of steps	41
4.2	Typical mouse dose rates and total doses per phase step for the image acquisition with the scanner at varying peak voltages	61
4.3	Comparison of CNR for different binning modes	62
4.4	Contrast-to-noise ratios for varying gantry delay times	66
5.1	Resolution measures obtained by different analysis methods from the data of the Moiré pattern measurements	88
5.2	Resolution measures obtained from the edge profile measurements conducted in the source plane	90
5.3	Resolution measures obtained from the edge profile measurements at the edges of the G ₂ grating and at the wedge in the object plane	94
5.4	Resolution measures obtained from the edge profile measurements at the edges of the G ₂ grating and the analysis of the Moiré pattern with the Fourier sum method	96
5.5	Resolution measures obtained from the edge profile measurements of the wedge in the object plane recorded with different binning modes	100
5.6	Resolution measures from the edge profile measurements at the horizontal and vertical edges of the G ₂ grating	101
5.7	Resolution measures obtained from the edge profile measurements with the rod aligned in different directions in the object plane	102
5.8	Resolution measures for different binning modes, describing the spatial system response in the plane used for normal imaging purposes	103
A.1	List of acquisition parameters for the comparison of CNRs with varying gain factors	116
A.2	List of acquisition parameters for the comparison of the CNRs with varying exposure times per step	117
A.3	List of acquisition parameters for the comparison of the CNRs with same total exposure and different numbers of steps	118
A.4	List of acquisition parameters for the comparison of the contrast parameter and the maximal CNR with varying peak voltages	119
A.5	List of acquisition parameters for the acquisitions with the new G ₂ grating. . .	120
A.6	List of acquisition parameters for the comparison of the CNRs in different binning modes	123

A.7	List of acquisition parameters for the comparison of the CNRs with varying delay parameters	124
A.8	List of acquisition parameters for all CT data sets	126
A.9	CNR results for supplementary CT measurements	127